

Review and Improvement of Methods for Estimating Rates of Photolysis in Photochemical Models

Volume I

**Final Report
Contract No. 96-335**

Prepared for:

**California Air Resources Board and
the California Environmental Protection Agency**

Prepared by:

**Laurent Vuilleumier and Nancy J. Brown
Ernest Orlando Lawrence Berkeley National Laboratory**

**Robert A. Harley
University of California at Berkeley**

and

**Steven D. Reynolds
Envair, 12 Palm Avenue, San Rafael, California, 94901-2222**

December 8, 2000

Disclaimer

The statements and conclusions in this Report are those of the contractors and not necessarily those of the California Air Resources Board. The mention of commercial products, their source, or their use in connection with material reported herein is not to be construed as actual or implied endorsement of such products.

Acknowledgments

The authors thank James Pederson of the California Air Resources Board and the staff of CARB, Sasha Madronich of the National Center for Atmospheric Research, Linsey Marr of the University of California at Berkeley and James Slusser and David Bigelow from the Natural Resource Ecology Laboratory for their valued advice.

This report was submitted in fulfillment of ARB contract 96-335, Review and Improvement of Methods for Estimating Rates of Photolysis in Photochemical Models, by Lawrence Berkeley National Laboratory and the University of California at Berkeley under sponsorship of the California Air Resources Board. Work was completed as of May 31, 2000.

Table of Contents

Disclaimer	ii
Acknowledgments.....	iii
Table of Contents	iv
List of Tables	vi
List of Figures	vii
Abstract	ix
Executive Summary	x
1 Introduction	1
1.1 Motivation.....	1
1.2 Objectives.....	3
1.3 Approach.....	3
1.4 Report overview	3
2 Radiative Transfer Theory and Models.....	5
2.1 Actinic flux and photolysis rate coefficients	5
2.2 Radiation transfer general equation	6
2.3 Two-stream methods.....	9
2.4 Other methods	12
2.5 Current radiation transfer models	13
2.6 Selection of TUV for modeling radiation transfer	14
2.7 Implementation Issues for Air Quality Models.....	15
2.7.1 Calculation of photolysis rates in UAM-IV.....	15
2.7.2 Calculation of photolysis rates in UAM-FCM.....	16
2.7.3 Calculation of photolysis rates in SAQM.....	17
2.7.4 Photolysis reactions in the SAPRC and CB-IV mechanism.....	17
2.7.5 Elevation grid treatment in Air Quality Models	19
3 Photolysis Sensitivity to Radiative Transfer Parameters	21
3.1 Sensitivity to the aerosol parameters	26
3.2 Sensitivity to the air temperature.....	27
3.3 Sensitivity to the ground albedo	28
3.4 Sensitivity to the total ozone column.....	28

4	Variability in Optical Depth during SCOS97.....	30
4.1	SCOS97 Data	31
4.1.1	Experimental Measurement.....	31
4.1.2	Cloud influence	36
4.1.3	Distributions of optical depths.....	38
4.2	Statistical Analysis.....	41
4.2.1	Methodology	41
4.2.2	Results.....	43
5	Radiative Transfer Model Input Parameters	51
5.1	Aerosol optical properties and ozone column	51
5.2	Review of Routine Radiation Data	52
5.3	Ground albedo	55
6	Radiative Transfer and Photolysis Module Implementation.....	57
7	Implementation of TUV AQM in Three Air Quality Models.....	59
7.1	AQM code and input modifications.....	59
7.2	Model results.....	60
8	Conclusions	73
8.1	Radiative Transfer Models.....	73
8.2	TUV Sensitivity to Input Data.....	73
8.3	Variability in Optical Depth.....	74
8.4	Implementation and Application of TUV.....	74
9	Recommendations.....	76
9.1	Radiometric data.....	76
9.2	Clouds	76
9.3	Air Quality Modeling.....	76
	Literature cited	77

List of Tables

Table 2.1: Photolysis reactions in SAPRC97 and CB-IV.....	18
Table 2.2: Discretization of the grid using σ -coordinates in SAQM.....	20
Table 3.1: Reactions considered in sensitivity analysis.....	22
Table 3.2: Nominal parameter values and ranges of variation used in sensitivity analysis	24
Table 3.3: Normalized sensitivity coefficients.....	26
Table 4.1: Correlations between optical depth measurements at various wavelengths....	46
Table 7.1: Influence of using TUVAQM for selected species in the SoCAB. Results for August 28, 1987, expressed as the range of the differences in concentrations (UAM621 with TUVAQM minus UAM621 and similarly for UAM-FCM).	63

List of Figures

Figure 3.1: Photolysis rate coefficients normalized sensitivity to radiative transfer model parameters.....	25
Figure 4.1: Logarithm of zero intercept ($\ln V_0$) time series and residual distribution for Mt Wilson at $\lambda = 333$ nm. V_0 is the value in mV that would be obtained by measuring the extraterrestrial irradiance with the radiometer used in this study.....	34
Figure 4.2: Optical depth time series for July 16 and 17, 1997 at Riverside at $\lambda = 300, 318$ and 368 nm.	37
Figure 4.3: Broadband visible total solar irradiance vs. cosine solar zenith angle.....	38
Figure 4.4: Optical depth distributions at $\lambda = 300, 306, 317$ and 368 nm.	39
Figure 4.5: Averages and standard deviations of the optical depth distributions vs. wavelength.....	40
Figure 4.6: Geometrical analogy for Principal Component Analysis.....	43
Figure 4.7: Optical depth correlations at Riverside (optical depths at $300, 306$ and 312 nm vs. optical depths at 318 and 326 nm).	44
Figure 4.8: Optical depth correlations at Mt Wilson (optical depths at $300, 306$ and 312 nm vs. optical depths at 318 and 326 nm).	45
Figure 4.9: Eigenvalues of the correlation matrices for Riverside and Mt Wilson.	47
Figure 4.10: Wavelength-dependent optical depth contributions to first and second principal components.	48
Figure 5.1: Cumulative frequency distributions of optical depths ($\tau - \tau_R$) at $\lambda=333$ nm for two southern California monitoring sites from summer 1997.....	52
Figure 5.2: Radiation monitoring sites in the San Joaquin Valley.	53
Figure 5.3: Correlation between total solar and UV irradiance at Three Rocks.	54
Figure 5.4: Correlation between total solar and UV irradiance at Riverside.	55
Figure 5.5: Los Angeles Area ground albedo distribution.	55

Figure 5.6:	Los Angeles Area ground albedo map (5×5 km grid). The size of the squares is inversely proportional to the albedo (smallest squares correspond to 0.22, and largest to 0.07) so that the lower albedo regions appear darker, and the higher albedo regions appear lighter.....	56
Figure 7.1.	Calculated hourly-averaged ground level ozone concentrations (ppb) at 1400 on August 28, 1987 using the original version of UAM621.	64
Figure 7.2.	Calculated hourly-averaged ground level ozone concentrations (ppb) at 1400 on August 28, 1987 using UAM621 with TUVAQM.....	65
Figure 7.3.	Difference in calculated hourly-averaged ground level ozone concentrations (ppb) at 1400 on August 28, 1987 – UAM621 with TUVAQM minus UAM621	66
Figure 7.4.	Calculated hourly-averaged ground level ozone concentrations (ppb) at 1400 on August 28, 1987 using the original version of UAM-FCM.....	67
Figure 7.5.	Calculated hourly-averaged ground level ozone concentrations (ppb) at 1400 on August 28, 1987 using UAM-FCM with TUVAQM	68
Figure 7.6.	Difference in calculated hourly-averaged ground level ozone concentrations (ppb) at 1400 on August 28, 1987 – UAM-FCM with TUVAQM minus UAM-FCM.....	69
Figure 7.7.	Calculated hourly-averaged ground level ozone concentrations (ppb) at 1500 on August 5, 1990 using the original version of SAQM.....	70
Figure 7.8.	Calculated hourly-averaged ground level ozone concentrations (ppb) at 1500 on August 5, 1990 using SAQM with TUVAQM	71
Figure 7.9.	Difference in calculated hourly-averaged ground level ozone concentrations (ppb) at 1500 on August 5, 1990 – SAQM with TUVAQM minus SAQM	72

Abstract

Photolysis of species such as NO_2 and formaldehyde influence significantly the formation of photochemical air pollution. Improved description of spatial and temporal variations in photolysis rates is needed, and improving the description of ultraviolet light intensity is key to improving urban and regional air quality models in this respect. Radiative transfer models were reviewed, and the Tropospheric Ultraviolet-Visible (TUV) model was implemented as a flexible photolysis module for online use within air quality models. Radiation measurements from the 1997 Southern California Ozone Study were used to assess the contributions of aerosols and ozone to variability in atmospheric optical depth. Aerosols were found to account for 90% or more of the observed **variability** in optical depth.

Sensitivity analysis was combined with an assessment of the likely range of variation for key TUV inputs parameters to estimate their influence on photolysis rate uncertainty. The amount of aerosol and its relative efficiency in scattering versus absorbing UV radiation each were found to lead to ~10% uncertainties in photolysis rate coefficients. The total ozone column (mostly stratospheric ozone) influences photolysis reactions that occur mainly at wavelengths below 300 nm (e.g., ozone and formaldehyde photolysis), but is of negligible influence for reactions that occur over a broad range of UV wavelengths (e.g., NO_2).

The photolysis module was used in two versions of the Urban Airshed Model (UAM), and in the SARMAP Air Quality Model (SAQM). For UAM applied to Los Angeles in August 1987, significant increases (up to ~100 ppb) in predicted ozone concentrations were found in localized areas of the eastern part of the South Coast Air Basin. The photolysis module includes both improved treatment of radiative transfer and upgraded absorption cross sections and quantum yields for photolyzing species. When SAQM was applied to central California for August 1990, smaller increases (up to ~40 ppb) in predicted ozone concentrations were seen, as expected given the more similar treatment of photolysis.

Executive Summary

Photolysis rates strongly influence the formation of photochemical air pollutants such as ozone. Photolysis rates of NO_2 and, depending on the VOC to NO_x ratio, formaldehyde are found to be among the most influential chemical reactions. The rates of photolysis depend on the integral of the product of absorption cross section, quantum yield and actinic flux over wavelength. While laboratory measurements have improved our understanding of cross sections and quantum yields for various photolyzing species, the representation of actinic flux in many air quality models is simplistic.

Radiative transfer models exist that are fundamentally based in theory. Models that compute the spherically integrated light intensity (actinic flux) are appropriate for use in calculating photodissociation rate coefficients. These models differ mainly in the degree of approximation of their description of the angular dependence of the light intensity. In this research, the Tropospheric Ultraviolet-Visible radiation transfer model (TUV) was implemented to run online within urban and regional-scale photochemical models.

Data on atmospheric optical properties are sparse at the wavelengths influencing photolysis of atmospheric pollutants (i.e., the near UV from 290 to 420 nm). Important factors affecting the actinic flux include solar zenith angle, clouds, aerosol amount and optical properties, total ozone column, terrain elevation and ground albedo. Although higher-order approximations are available, we used a two-stream model in the present implementation of TUV. This was done to minimize computational burden and because larger uncertainties are related to the lack of appropriate data for the TUV model inputs described above.

The sensitivity of photodissociation rate coefficients to selected TUV input parameters was examined, and the likely range of variation for these parameters was assessed. Two aerosol properties were found to be similarly influential. The aerosol optical depth (aerosol amount) has a potential wide range of variation, and normalized sensitivities between -5% and -10% depending on the reaction. These sensitivities are negative implying that an increase in aerosol total optical depth would lead to a decrease in photolysis rate coefficients (in the surface layer). The aerosol single scattering albedo is uncertain, especially at the ultraviolet wavelengths; likely values range from 0.75 to 0.95. The normalized sensitivity to this parameter is about +50% indicating that a 10% change in single scattering albedo would induce a 5% change in photolysis rate coefficients. We expect variation in photolysis rate coefficients due to these parameters to be on the order of 10%. During summer, ground albedo in the Los Angeles area ranges from about 0.05 to 0.20. Normalized sensitivity is on the order of 15%. The challenge here is to obtain high quality spatially-resolved values for ground albedo. The influence of total ozone column varies

greatly depending on the reaction of interest. Not surprisingly, ozone photolysis rates are the most strongly affected. Formaldehyde photolysis rates are also influenced significantly by ozone column, whereas NO₂ and nitrous acid are barely affected. Variation of 10% (i.e., 30 Dobson Units) in ozone column lead to changes of 15% in ozone photolysis (for the O(¹D) channel), and 4% in formaldehyde photolysis (for the channel that forms radicals).

Aerosols have the potential to affect photolysis reaction rates significantly (see above), and their optical properties have significant uncertainties. Therefore, we studied variability in total optical depths (including contributions due to Rayleigh scattering and absorption by ozone) in southern California to assess the importance of the aerosol contribution.

Measurements of direct (i.e., total minus diffuse) solar irradiance were made during the 1997 Southern California Ozone Study continuously at seven wavelengths at 300, 306, 312, 318, 326, 333 and 368 nm. At 300 nm, optical depths (mean \pm 1 S.D.) measured over the entire study period were 4.3 ± 0.3 at Riverside and 3.7 ± 0.2 at Mt Wilson. Optical depth decreased with increasing wavelength, falling at 368 nm to values of 0.8 ± 0.2 at Riverside and 0.5 ± 0.1 at Mt Wilson. At all wavelengths, both the mean and the relative standard deviation of optical depths were larger at Riverside than at Mt Wilson. At 300 nm, the difference between the smallest and largest observed optical depths corresponds to over a factor 2 increase in the direct beam irradiance for overhead sun, and over a factor 7 increase for a solar zenith angle of 60°.

Principal Component Analysis was used to reveal underlying factors contributing to variability in optical depths. PCA showed that a single factor (component) was responsible for the major part of the variability. At Riverside, the first component was responsible for 97% of the variability and the second component for 2%. At Mt Wilson, 89% of the variability could be attributed to the first component and 10% to the second. Dependence of the component contributions on wavelength allowed identification of probable physical causes: the first component is linked to light scattering and absorption by atmospheric aerosols, and the second component is linked to light absorption by ozone. These factors are expected to contribute to temporal and spatial variability in solar actinic flux and photodissociation rates of species including ozone, nitrogen dioxide, and formaldehyde.

The TUV model as been implemented as a flexible module that can be used within photochemical air quality models. A new interface was developed to allow flexible specification of TUV input parameters by the model user. (The version of the module modified for implementation in air quality models is designated as TUV AQM.) This will allow air quality models to take advantage of more and better input data as they become available. The

implementation of TUVAQM is highly modular, so that state-of-the-art treatment of radiative transfer can be maintained (e.g., switch to 4- or 8-stream models).

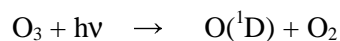
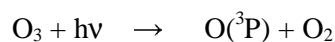
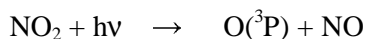
The photolysis module was implemented in three photochemical models: the Urban Airshed Model (UAM621), the Urban Airshed Model with Flexible Chemical Mechanism (UAM-FCM), and the SARMAP Air Quality Model (SAQM). The UAM621 and UAM-FCM models were used to simulate the August 26-28, 1987, SCAQS ozone episode in the South Coast Air Basin (SoCAB). Generally, higher calculated ozone concentrations resulted from employing TUVAQM, especially in the late morning and afternoon hours when relatively high ozone levels occur. For example, in the early afternoon of the simulation of 28 August, calculated hourly-averaged ozone concentrations were as much as 131 and 81 ppb higher using TUVAQM in UAM621 and UAM-FCM, respectively. Significant increases in calculated ozone concentrations occurred in the downwind areas of the San Gabriel Valley and the Riverside-San Bernardino areas. Much smaller increases in calculated ozone concentrations were noted in offshore, coastal, and central basin areas as well as in the easternmost and northernmost portions of the modeling domain. Differences in predicted ozone using TUVAQM may result not only from improved treatment of radiative transfer, but also because of more up to date information on absorption cross-section and quantum yields of photolyzing species such as formaldehyde.

SAQM was applied to the simulation of a large portion of central California for the August 3-6, 1990, ozone episode. Since the existing photolysis treatment in SAQM and TUVAQM share a somewhat similar origin, calculated ozone levels resulting from the implementation of TUVAQM were not as different as those noted for the implementation in UAM621 and UAM-FCM.

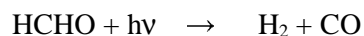
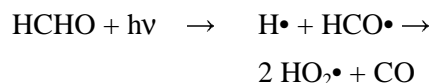
1 Introduction

1.1 Motivation

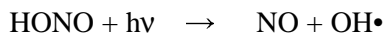
There are numerous photolysis reactions that occur in the troposphere in the presence of sunlight (see Finlayson-Pitts and Pitts, 1986). Although the exact wavelengths that cause photolysis vary by species, generally photolysis reactions occur in the troposphere when radiation in the near ultraviolet ($\lambda < \sim 400$ nm) is absorbed by photodissociating gas molecules. For example, the photolysis of nitrogen dioxide (NO_2) and ozone (O_3) yields free monatomic oxygen:



where $E = h\nu$ is the energy associated with a photon of frequency $\nu = c/\lambda$. The recombination of ground-state monatomic oxygen $\text{O}({}^3\text{P})$ with O_2 is the only reaction that forms ozone in both the troposphere and the stratosphere. Electronically excited oxygen $\text{O}({}^1\text{D})$ can react with water vapor to generate hydroxyl radicals which, in turn, initiate and drive the oxidation of volatile organic compounds (VOC) in the atmosphere. Other important reactions taking place in the troposphere include the photolysis of formaldehyde (HCHO):



and the photolysis of nitrous acid (HONO):



In the context of urban and regional ozone pollution problems, we have determined first- and second-order sensitivities for ozone concentration with respect to the reaction rate coefficients and initial conditions in a photochemically active system represented by a box model (Vuilleumier et al., 1997). We found the NO_2 , HONO , and HCHO photolysis reactions to be among the seven most important reactions affecting ozone formation in the LCC chemical mechanism (Lurmann et al., 1987). The LCC mechanism is of the same vintage and is comparable in level of detail to the Carbon Bond IV mechanism (CB-IV; Gery et al., 1992). Similar sensitivity analysis findings were reported for the CB-IV mechanism by Milford et al. (1992).

During the 1990 San Joaquin Valley Air Quality Study, layers of high ozone were observed aloft (*i.e.*, 500 m to several km above ground); to date it has not been possible to reproduce or explain these observations using air quality models. A possible explanation is that vertical variations in photolysis rates are not adequately represented in the models. Photolysis rates are known to affect ozone concentrations, as illustrated by the following examples. We found that when all photolysis rate coefficients were increased by 10% above baseline values in Urban Airshed Model simulations for Sacramento (July 11-13, 1990 episode), the predicted peak ozone concentration increased by 9% from 139 to 152 ppb. In modeling ozone formation in California's South Coast Air Basin, Harley et al. (1993) found that large differences existed in the NO₂ photolysis rate coefficient inferred from simultaneous measurements of broadband ultraviolet radiation intensity at 5 Los Angeles area sites, and that use of revised photolysis rates (lower than clear sky modeled values) led to a significant drop in predicted ozone levels. Air quality model performance may be improved by representing the spatial and temporal variations in photolysis rates more accurately.

In the context of air quality modeling, radiation transfer models are of interest for computing photolysis rate coefficients J . The rate of chemical species X photolysis via a given reaction is found by multiplying J_X with the concentration of species X undergoing the photolysis. The photolysis rate coefficient J_X is evaluated by integrating over wavelengths using the relationship

$$J_X = \int_0^{\infty} \sigma_X(\lambda) \phi_X(\lambda) F(\lambda) d\lambda \quad (1.1)$$

where $\sigma_X(\lambda)$ is the absorption cross-section (cm²), $\phi_X(\lambda)$ is the quantum yield, and $F(\lambda)$ is the actinic flux (photons cm⁻² s⁻¹ nm⁻¹). For a specific molecule reacting in the troposphere, the lower limit of integration is frequently set $\lambda = 290$ nm and the higher limit is the longest wavelength where the photochemical reaction occurs (the reaction threshold). Most photolysis reactions of interest for air quality occur in the wavelength region $\lambda = 290$ to 420 nm (*i.e.*, the near UV).

Even though the photolysis reactions identified above have been studied extensively, there is uncertainty associated with the rate coefficients when they are calculated according to Eq. (1.1) for use in models. Calculations for all species suffer from inaccurate representations of the actinic flux. Significant improvement in the description of photolysis could be achieved by improving the treatment of radiative transfer in the AQMS. The improved treatment of radiative transfer used to estimate the actinic flux as a function of wavelength should have the following characteristics:

- It must be based upon sound fundamental science.
- It must provide a reliable estimate of radiative transfer, that is, the errors associated with using them should be commensurate with errors in model input parameters.
- It must be computationally feasible.

1.2 Objectives

Motivated by the need to improve the description of radiative transfer to improve the evaluation of photolysis reactions in Air Quality Modeling Systems (AQMS), we pursued research whose **Objectives** were to:

- 1) review the state-of-the-science in radiative transfer modeling in support of photolysis calculations for atmospheric tropospheric chemistry models;
- 2) develop an improved photolysis module and appropriate procedures for developing location and day-specific inputs from routinely available monitoring data;
- 3) analyze measurements from the Riverside/Mt. Wilson solar radiation study that was part of the 1997 Southern California Ozone Study (SCOS97) to develop data for the photolysis module, and
- 4) incorporate the improved photolysis module into current regulatory ozone models.

1.3 Approach

During the course of this study, we improved the representation of the radiative transfer for AQMS, after reviewing the state-of-the-science. We developed a new module that can be used with AQMS without imposing an unreasonable computational burden, wrote a supporting manual to facilitate its implementation, analyzed radiometer data from the SCOS97 field study, and incorporated the new module into three current air quality models. The approach that was pursued to achieve our objective is described in detail in the various chapters of our report.

1.4 Report overview

Chapter 2 of our report presents a discussion of radiative transfer theory and the various models used to evaluate it. In this chapter we describe why the TUV model by Dr. Sasha Madronich of the National Center for Atmospheric Research (NCAR) was selected for implementation into AQMS. Implementation issues are also discussed in this chapter. The study that we conducted to determine the sensitivity of photolysis to radiative transfer parameters is discussed in Chapter 3. This sensitivity analysis identifies the most significant input parameters that affect radiative transfer.

A large-scale field study of ozone formation in Southern California (SCOS97-NARSTO) was conducted during summer 1997, to improve understanding of the emissions, atmospheric chemistry, and meteorological conditions leading to the notorious photochemical air pollution problems in the Los Angeles area. In Chapter 4, we discuss the analysis of solar UV irradiance measurements made at two Southern California sites experiencing different levels of air pollution. We describe our analysis of ground-based UV irradiance data from the SCOS97 field campaign at Riverside and Mt Wilson, California. Briefly, we computed total optical depths (*i.e.*, the solar direct beam differential extinction rate, see Section 2) and determined their distribution for the period extending from July to the end of October 1997. We also computed the correlation coefficients between pairs of optical depths measured at different wavelengths, and used principal component analysis (PCA) to identify the underlying factors responsible for the variability observed in the optical depths. Accounting for the variability in the calculation of the actinic flux reduces the uncertainty in photolysis rates in air quality models and improves our calculation of ozone formation. Also in this chapter, we describe how principal component analysis allows us to attribute the optical depth variability mainly to concentration changes in aerosols and marginally to changes in the ozone column.

Chapter 5 contains a discussion of radiative transfer model input parameters that are needed by the model to calculate photolysis rates. In addition to aerosols and other surface parameters discussed earlier in the report, routine radiation data collected in the state is reviewed. Chapter 6 in the report provides a discussion of radiative transfer and discusses photolysis module implementation issues. Chapter 7 describes application of the photolysis module in three regulatory AQMS: UAM-IV, UAM-FCM, and the SARMAP Air Quality Model (SAQM). In Chapter 8, we summarize our findings and offer suggestions for future research concerned with improving the description of photolysis in AQMS.

Volume II of this report is a standalone user's guide for the TUV AQM Radiative Transfer and Photolysis Module. It describes the underlying physics that supports the model, describes various options for model implementation, and provides directions for preparation of the model-input stream.

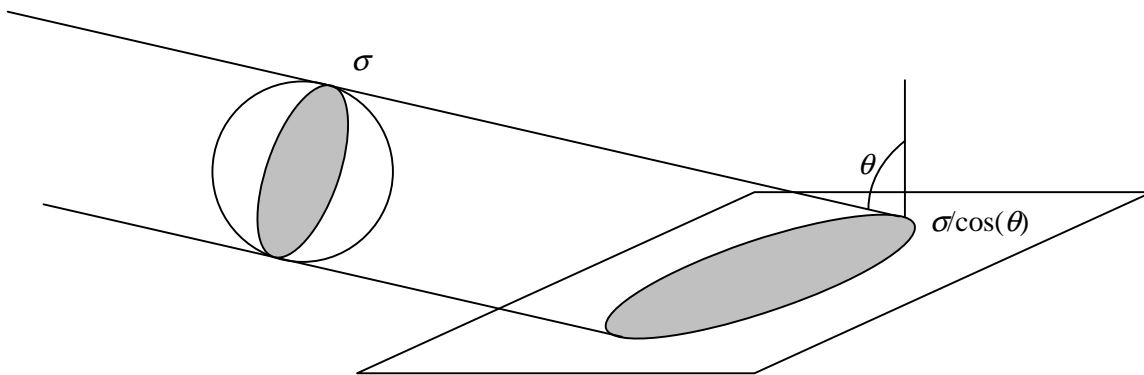
2 Radiative Transfer Theory and Models

2.1 Actinic flux and photolysis rate coefficients

Radiation transfer models are used to obtain theoretical estimations of quantities that depend on the radiation flux. Examples of such quantities include, but are not limited to, coefficients for determining the speed of chemical reactions induced by solar radiation in the atmosphere (photolysis), solar radiation flux, radiation effects on living species and heating of the earth by solar radiation. Two quantities of importance for this purpose are the actinic flux and the irradiance. Both measure the amount of light that crosses a unit surface area per unit of time, and per unit interval of wavelength. The actinic flux is the spherically-integrated light intensity that is appropriate for calculating photolysis reaction rate coefficients (see Madronich, 1987). The irradiance refers to a flux across a horizontal plane; sunlight intensity is commonly measured and reported in terms of irradiance. The actinic flux F and irradiance I as a function of frequency $\nu = hc/\lambda$ are defined by:

$$\begin{aligned} F(\nu) &\equiv \int d\phi \int d\theta u_\nu(\theta, \phi) \sin \theta \\ I(\nu) &\equiv \int d\phi \int d\theta u_\nu(\theta, \phi) \cos \theta \sin \theta \end{aligned} \quad (2.1)$$

where $u_\nu(\theta, \phi)$ is the spectral radiance (sometime also called radiation specific intensity or, simply, intensity) associated with a specific zenith angle θ and azimuth angle ϕ . To illustrate the difference between actinic flux and irradiance, let us consider a cylindrical parallel beam of light. The actinic flux is the flux of light received by a molecule of cross section σ . A molecule of cross section σ can be represented as a sphere that subtends an area σ to the light beam. In such a case, the direction of the light beam does not matter, and the area taken into account for computing the flux is always σ . When computing the irradiance (*i.e.*, the light flux across a horizontal plane) the surface intersected by the beam is augmented by a factor $1/\cos(\theta)$. Consequently, the irradiance is a factor $\cos(\theta)$ less than the actinic flux in this example.



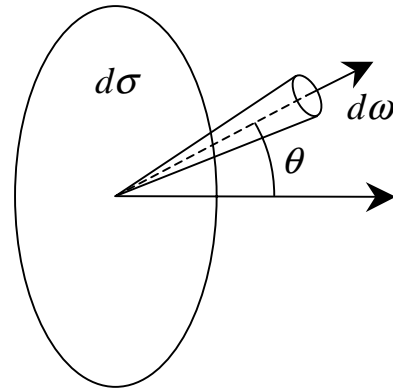
In the context of air quality modeling, radiation transfer models are of interest for computing photolysis rate coefficients J . The rate of chemical species photolysis via a given reaction X is found by multiplying J_X with the concentration of the species undergoing the photolysis. The photolysis rate coefficient J_X is evaluated by integrating over wavelengths using the relationship

$$J_X = \int_0^\infty \sigma_X(\lambda) \varphi_X(\lambda) F(\lambda) d\lambda \quad (2.2)$$

where $\sigma_X(\lambda)$ is the absorption cross-section (cm^2), $\varphi_X(\lambda)$ is the quantum yield, and $F(\lambda)$ is the actinic flux ($\text{photons cm}^{-2} \text{s}^{-1} \text{nm}^{-1}$). For a specific molecule reacting in the troposphere, the lower limit of integration is frequently set $\lambda = 290 \text{ nm}$ and the higher limit is the longest wavelength where the photochemical reaction occurs (the reaction threshold). Most photolysis reactions of interest for air quality occur in the wavelength region $\lambda = 290 \text{ to } 420 \text{ nm}$ (*i.e.*, the near UV).

2.2 Radiation transfer general equation

The objective of radiation transfer models is to determine how the radiance propagates through the atmosphere. Most radiation transfer models are based on theoretical developments attributed to Chandrasekhar (1960). Chandrasekhar defines the radiance u_ν at frequency ν by its relationship to the amount of radiant energy, dE_ν , in a frequency interval $(\nu, \nu + d\nu)$, which is transported across an element of area $d\sigma$ and in directions confined to an element of solid angle $d\omega$, during a time dt :



$$dE_\nu = u_\nu \cos \theta d\nu d\sigma d\omega dt \quad (2.3)$$

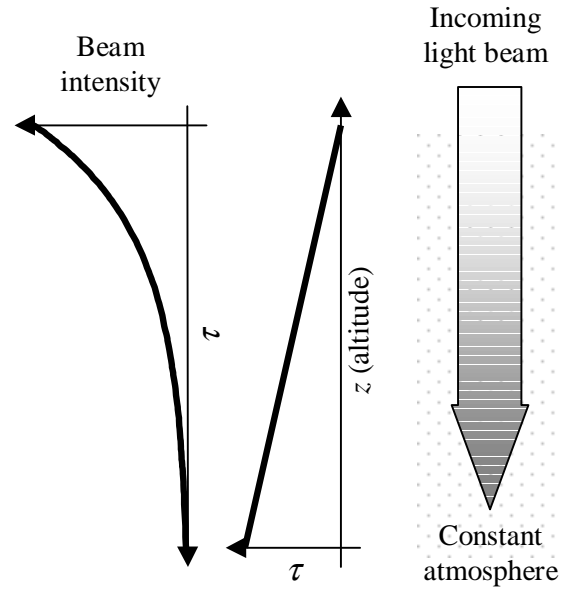
When the radiation transfer occurs in an atmosphere composed of parallel horizontal layers, the radiance transfer equation can be expressed as (see Liou, 1973 or Stamnes *et al.*, 1988):

$$\begin{aligned} \mu \frac{du_\nu(\tau_\nu, \mu, \phi)}{d\tau_\nu} = & u_\nu(\tau_\nu, \mu, \phi) \\ & - \frac{\omega_\nu(\tau_\nu)}{4\pi} \int_0^{2\pi} d\phi' \int_{-1}^{+1} d\mu' P_\nu(\tau_\nu, \mu, \phi, \mu', \phi') u_\nu(\tau_\nu, \mu', \phi') \\ & - Q_\nu(\tau_\nu, \mu, \phi) \end{aligned} \quad (2.4)$$

Eq. (2.4) describes the radiance transfer in the direction defined by μ the cosine of the zenith angle and ϕ the azimuth angle at the altitude z corresponding to the optical depth τ_ν defined by:

$$\tau_\nu = \int_z^\infty k_\nu \rho dz \quad (2.5)$$

where k_v is the extinction coefficient and ρ the density. The optical depth is a measure of the opacity of the atmosphere to light. When an incoming beam of light goes through the atmosphere, it has a probability of extinction through absorption or scattering that is proportional to the density ρ of the absorbing and scattering atmosphere and an extinction coefficient k_v depending on the properties of the atmosphere (pollutant and trace gas loading, etc.). In case the density and other properties of the atmosphere are **constant** along the light beam path, the optical depth increases linearly with distance, and the intensity of the incoming light beam decreases exponentially with distance with an exponent of $-\tau_v$. However, the amount of light available usually does not decrease as much, because part of the light lost from the incoming beam is scattered in another direction.



If an atmosphere layer has constant density and optical properties, optical depth increases linearly with decreasing altitude, while beam intensity decreases exponentially.

The first term of the right-hand side of Eq. (2.4) is a loss term proportional to the radiance that represents the absorption and scattering of light by the atmosphere. The extinction coefficient would be present in this loss term if the radiation transfer equation were expressed as a function of beam light path, but Eq. (2.4) is expressed as a function of the optical depth, which already includes the extinction coefficient. The remainder of Eq. (2.4) right-hand side is a source term split into a scattering source term and another term, Q_v , covering all other sources. The scattering source term expresses the amount of radiance that is scattered from the direction (μ', ϕ') into the direction (μ, ϕ) . Since this term is integrated over the whole solid angle, the scattering of light from all directions into the direction (μ, ϕ) is considered in this term. $P_v(\tau_v, \mu, \phi, \mu', \phi')$ is the phase function indicating the fraction of the light from direction (μ', ϕ') scattered into the direction (μ, ϕ) , while $\omega_v(\tau_v)$ is the single scattering albedo, and indicates what fraction of the extinguished light is scattered (the rest is absorbed). The phase function and the single scattering albedo depend on the absorbing and scattering material in the atmosphere. While a term for thermal emission in local thermodynamic equilibrium is sometimes included in Q_v , only the contribution of scattering from the direct solar beam will be considered here. In this case,

$$Q_\nu = \frac{\omega_\nu(\tau_\nu)}{4} F_{0\nu} P_\nu(\tau_\nu, \mu, \phi, -\mu_0, \phi_0) \exp\left(-\frac{\tau_\nu}{\mu_0}\right) \quad (2.6)$$

where πF_0 is the incident solar flux coming from the direction (μ_0, ϕ_0) and the exponential term represents the diminution of the direct beam by extinction before reaching the depth τ_ν .

When there is no explicit radiance transfer from one frequency to another (the thermal emission term can be viewed as an implicit transfer of radiance), the frequency index ν in Eq. (2.4) can be dropped without loss of generality.

Analytical solutions of Eq. (2.4) can only be found in simplified cases, and numerical methods are often used. The main difficulty comes from the integration over the whole solid angle in the scattering source term. Most methods for finding analytical or numerical solutions to Eq. (2.4) have common features that were devised by Chandrasekhar. The first step common to almost all methods is to simplify the integration over the azimuth angle in Eq. (2.4) by expanding the radiance in a Fourier cosine series:

$$u(\tau, \mu, \phi) = \sum_{m=0}^{2N-1} u^m(\tau, \mu) \cos m(\phi_0 - \phi). \quad (2.7)$$

Because ϕ is the azimuth angle, the radiance has a periodicity of 2π as a function of ϕ , and any azimuth dependence can be expressed as a Fourier cosine series as in Eq. (2.7). In order to simplify the angular integration in Eq. (2.4), the other term featuring an azimuth dependence, the phase function, needs to be expressed as a series where the azimuth and zenith dependence are separated. The phase function is expressed as a sum of Legendre polynomials that, by using the addition theorem for spherical harmonics, is transformed to:

$$P(\tau, \mu, \phi, \mu', \phi') = \sum_{m=0}^{2N-1} (2 - \delta_{0,m}) \cos m(\phi' - \phi) \sum_{l=m}^{2N-1} (2l+1) g_l^m(\tau) P_l^m(\mu) P_l^m(\mu') \quad (2.8)$$

where g_l^m are sets of constants that are determined using the orthogonal property of Legendre polynomials. Inserting Eqs. (2.7) and (2.8) in Eq. (2.4), a set of $2N$ **decoupled** equations (one for each Fourier component) is obtained:

$$\begin{aligned} \mu \frac{du^m(\tau, \mu)}{d\tau} &= u^m(\tau, \mu) \\ &- \frac{\omega(\tau)}{2} \sum_{l=m}^{2N-1} (2l+1) g_l^m(\tau) P_l^m(\mu) \int_{-1}^{+1} d\mu' P_l^m(\mu') u^m(\tau, \mu') \\ &- \frac{\omega(\tau)}{4} F_0 \exp\left(-\frac{\tau}{\mu_0}\right) (2 - \delta_{0,m}) \sum_{l=m}^{2N-1} (-1)^{l+m} (2l+1) g_l^m(\tau) P_l^m(\mu) P_l^m(\mu_0) \end{aligned} \quad (2.9)$$

In situations that have azimuthal symmetry, such as when atmospheric optical properties are isotropic, and the solar zenith angle is zero, only the term $m = 0$ is considered. When the solar zenith angle is different from zero, the situation is not symmetric and other terms must be considered. However, it is often assumed that the azimuth dependence is not complex, and that a few terms are enough to represent the radiance azimuth dependence. Furthermore, when one is not interested in quantities that depend on the azimuth and zenith angles such as the radiance, but in quantities that are integrated on the whole solid angle such as the actinic flux, the terms with m higher than zero are sometimes dropped. Such simplification assumes the zenith dependency of u^m for $m > 0$ to be sufficiently close to this of u^0 for the latter to be used as surrogate for the other u^m .

2.3 Two-stream methods

In two-stream methods (see Meador and Weaver, 1980), it is assumed that only two streams of radiation (*i.e.*, two directions) exist. Both streams are vertical, one going downward, and the other upward. In such a case, the solution is symmetric with respect to the azimuth angle, and only the equation for $m = 0$ in Eq. (2.9) is retained. Defining $p(\tau, \mu, \mu')$ as:

$$p(\tau, \mu, \mu') = \omega(\tau) \sum_{l=0}^{2N-1} (2l+1) g_l^0(\tau) P_l^0(\mu) P_l^0(\mu'), \quad (2.10)$$

the following transfer equation is obtained (the superscript index $m=0$ is dropped for simplicity):

$$\begin{aligned} \mu \frac{du(\tau, \mu)}{d\tau} &= u(\tau, \mu) \\ &\quad - \frac{1}{2} \int_{-1}^{+1} d\mu' p(\tau, \mu, \mu') u(\tau, \mu') \\ &\quad - \frac{1}{4} F_0 \exp\left(-\frac{\tau}{\mu_0}\right) p(\tau, \mu, -\mu_0) \end{aligned} \quad (2.11)$$

The intensity of the streams are defined as the following hemispheric integrals:

$$u^\pm(\tau) = \int_0^1 u^\pm(\tau, \pm\mu) \mu d\mu, \quad (2.12)$$

and the quantity β_0 , representing the fraction of the direct solar beam that is scattered in the upward direction, is defined as:

$$\beta_0(\tau) = \frac{1}{2\omega(\tau)} \int_0^1 p(\tau, \mu, -\mu_0) d\mu. \quad (2.13)$$

Because the phase function is normalized as $\int_{-1}^1 p(\tau, \mu, \mu') d\mu' = 2\omega(\tau)$, then

$$\beta_0(\tau) = 1 - \frac{1}{2\omega(\tau)} \int_0^1 p(\tau, -\mu, -\mu_0) d\mu. \quad (2.14)$$

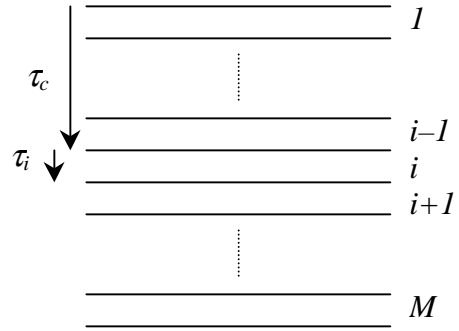
Thus, after integrating Eq. (2.11) from 0 to 1 along μ in one case and $-\mu$ in the other, the following pair of equations is obtained:

$$\begin{aligned} \frac{du^+(\tau)}{d\tau} &= \int_0^1 u(\tau, \mu) d\mu \\ &\quad - \frac{1}{2} \int_0^1 d\mu \int_{-1}^{+1} d\mu' p(\tau, \mu, \mu') u(\tau, \mu') - \frac{1}{2} F_0 \omega(\tau) \beta_0(\tau) \exp\left(-\frac{\tau}{\mu_0}\right) \\ \frac{du^-(\tau)}{d\tau} &= - \int_0^1 u(\tau, -\mu) d\mu \\ &\quad + \frac{1}{2} \int_0^1 d\mu \int_{-1}^{+1} d\mu' p(\tau, -\mu, \mu') u(\tau, \mu') + \frac{1}{2} F_0 \omega(\tau) (1 - \beta_0(\tau)) \exp\left(-\frac{\tau}{\mu_0}\right) \end{aligned} \quad (2.15)$$

The two-stream methods approximate $u(\tau, \mu)$ so that it is related to $u^\pm(\tau)$ to obtain the following general form for the transfer equation:

$$\begin{aligned} \frac{du^+(\tau)}{d\tau} &= \gamma_1 u^+(\tau) - \gamma_2 u^-(\tau) - F_0 \omega(\tau) \gamma_3 \exp\left(-\frac{\tau}{\mu_0}\right) \\ \frac{du^-(\tau)}{d\tau} &= \gamma_2 u^+(\tau) - \gamma_1 u^-(\tau) + F_0 \omega(\tau) \gamma_4 \exp\left(-\frac{\tau}{\mu_0}\right) \end{aligned} \quad (2.16)$$

The parameters γ_1 , γ_2 , γ_3 , and γ_4 , depend on the assumed functional form $p(\tau, \mu, \mu')$. For the most commonly chosen functional forms, γ_1 , γ_2 , γ_3 , and γ_4 are simple functions of the single scattering albedo $\omega(\tau)$, the asymmetry parameter¹ $g(\tau)$ and the cosine of the solar zenith angle μ_0 . Consequently, the γ parameters depend on τ . In order to solve the coupled Eqs. (2.16), the atmosphere is divided into thin horizontal layers where the parameters are assumed constant². Within a layer, Toon *et al.* (1989) have shown that the general solution to the coupled Eqs. (2.16) is:



¹ The asymmetry parameter indicates whether the light is scattered in the forward or backward direction. It is the intensity-weighted average of the cosine of the scattering angle: $g(\tau) = \frac{1}{2} \int_{-1}^1 \mu' p(\tau, 1, \mu') d\mu'$.

² When deriving the solution, the layers are assumed to be planar. Corrections are made afterward to take into account atmospheric sphericity. Such corrections are only important for large solar zenith angle.

$$\begin{aligned}
u_i^+(\tau) &= k_{1i} \exp(\lambda_i \tau) - \Gamma_i k_{2i} \exp(-\lambda_i \tau) + C_i^+(\tau) \\
u_i^-(\tau) &= \Gamma_i k_{1i} \exp(\lambda_i \tau) - k_{2i} \exp(-\lambda_i \tau) + C_i^-(\tau)
\end{aligned} \tag{2.17}$$

where the index i stands for the layer number, k_1 and k_2 depend on the boundary conditions, and by assuming a layer of optical depth τ_i and cumulative optical depth τ_c for the layers above,

$$\begin{aligned}
\lambda_i &= \sqrt{\gamma_{1i}^2 - \gamma_{2i}^2} \\
\Gamma_i &= \frac{\gamma_{2i}}{\gamma_{1i} + \lambda_i} \\
C_i^+(\tau) &= \frac{\omega_i \pi F_0 [(\gamma_{1i} - 1/\mu_0) \gamma_{3i} + \gamma_{4i} \gamma_{2i}] \exp[-(\tau_c + \tau)/\mu_0]}{\lambda_i^2 - 1/\mu_0} \\
C_i^-(\tau) &= \frac{\omega_i \pi F_0 [(\gamma_{1i} + 1/\mu_0) \gamma_{4i} + \gamma_{2i} \gamma_{3i}] \exp[-(\tau_c + \tau)/\mu_0]}{\lambda_i^2 - 1/\mu_0}
\end{aligned} \tag{2.18}$$

First, Toon *et al.* scaled the terms so that none of them includes a positive τ -dependent exponent (terms with such positive exponents can lead to numerical instabilities):

$$\begin{aligned}
u_i^+(\tau) &= Y_{1i} (\exp[-\lambda_i (\tau_i - \tau)] + \Gamma_i \exp[-\lambda_i \tau]) \\
&\quad + Y_{2i} (\exp[-\lambda_i (\tau_i - \tau)] - \Gamma_i \exp[-\lambda_i \tau]) + C_i^+(\tau) \\
u_i^-(\tau) &= Y_{1i} (\Gamma_i \exp[-\lambda_i (\tau_i - \tau)] + \exp[-\lambda_i \tau]) \\
&\quad + Y_{2i} (\Gamma_i \exp[-\lambda_i (\tau_i - \tau)] - \exp[-\lambda_i \tau]) + C_i^-(\tau)
\end{aligned} \tag{2.19}$$

where $\tau < \tau_i$, since τ_i is the total optical depth of the layer, and

$$\begin{aligned}
Y_{1i} &= \frac{1}{2} (k_{1i} \exp(\lambda_i \tau_i) + k_{2i}) \\
Y_{2i} &= \frac{1}{2} (k_{1i} \exp(\lambda_i \tau_i) - k_{2i})
\end{aligned} \tag{2.20}$$

Then, an iterative solution scheme is devised from one layer to the other by requiring:

$$\begin{aligned}
u_i^+(\tau = \tau_i) &= u_{i+1}^+(\tau = 0) \\
u_i^-(\tau = \tau_i) &= u_{i+1}^-(\tau = 0) \\
u_1^-(\tau = 0) &= u_{d0}^- \\
u_M^+(\tau = \tau_M) &= R_{\text{sfc}} (u_M^-(\tau = \tau_M) + \mu_0 \pi F_0 \exp[-(\tau_c + \tau_M)/\mu_0])
\end{aligned} \tag{2.21}$$

where u_{d0}^- is a diffuse downward flux at the top of the atmosphere (usually set to 0), M is the total number of layers, and R_{sfc} is the ground surface reflectivity (albedo).

After rearranging the terms, Toon *et al.* found a set of $2M$ equations that compose a tridiagonal matrix of the form:

$$\begin{aligned}
A_j Y_{j-1} + B_j Y_j + D_j Y_{j+1} &= E_j \\
Y_j &= Y_{1i} \quad j = 2n - 1 \quad (\text{odd}) \\
Y_j &= Y_{2i} \quad j = 2n \quad (\text{even})
\end{aligned} \tag{2.22}$$

that is solved using a standard tridiagonal solution method. Once a solution is found for the expressions Y_{1i} and Y_{2i} , the solution for the upward and downward flux can be derived via Eq. (2.19), and the actinic flux defined in Eq. (2.1) can be computed with (Toon *et al.* 1989):

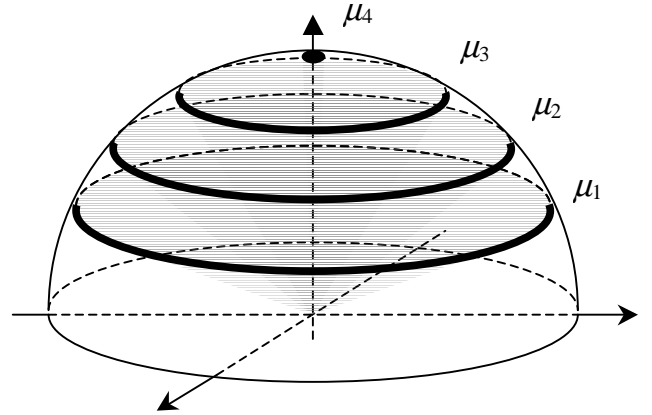
$$F_i = \frac{u_i^+ + u_i^-}{\mu_1}, \tag{2.23}$$

where μ_1 is a parameter that depends on the chosen two-stream approximation.

The type of two-stream approximation used defines the γ parameters. Meador and Weaver (1980) and Toon *et al.* (1989) give the value of these parameters for different types of two-stream methods.

2.4 Other methods

More complex methods than two-stream approximations allow a more precise description of the angular dependence of the radiance. They rely on applying a Gaussian quadrature rule to integrate over the zenith angle following Eq. (2.9). (For details, see Chandrasekhar, 1960, Liou, 1973 or Stamnes *et al.*, 1988.) The integral over μ' is replaced by a discrete sum over zenith angles using Gauss quadrature. The discrete zenith angle cosines (μ_i) and weights (a_i) are determined by Gauss quadrature rule, and a “light stream” is associated with each zenith angle. For each of the $2N$ equations for the Fourier components a set of $2n$ coupled equations should be solved (one for each quadrature zenith angle):



The integration over μ (the cosine of the zenith angle) is replaced with a sum of streams of light coming at different zenith angles where the μ_i and weights for the streams are defined by the Gaussian quadrature rule. The phase function indicates which fraction of light is transferred from one stream to another.

$$\begin{aligned}
\mu_i \frac{du^m(\tau, \mu_i)}{d\tau} = & u^m(\tau, \mu_i) \\
& - \frac{\omega(\tau)}{2} \sum_{l=m}^{2N-1} (2l+1) g_l^m(\tau) P_l^m(\mu_i) \sum_{\substack{j=-n \\ j \neq 0}}^n a_j P_l^m(\mu_j) u^m(\tau, \mu_j) \\
& - \frac{\omega(\tau)}{4\pi} I_0 \exp\left(-\frac{\tau}{\mu_0}\right) (2 - \delta_{0,m}) \times \\
& \sum_{l=m}^{2N-1} (-1)^{l+m} (2l+1) g_l^m(\tau) P_l^m(\mu_i) P_l^m(\mu_0) \quad i = \pm 1, \dots, \pm n
\end{aligned} \tag{2.24}$$

The discrete-ordinate method and the other related methods allow an arbitrarily precise description of the radiance angular dependence, according to the number of terms considered. At the lowest order ($m = 0$, and $n = 1$), they reduce to a two-stream method. When good precision in the angular description is desired, the dimensionality of the system of equations is large. There are $M \times 2n \times 2N$ equations, where M is the number of atmospheric horizontal layers, $2n$ is the number of Gaussian quadrature points (zenith angles), and $2N$ is the number of Fourier azimuth components³.

2.5 Current radiation transfer models

Excluding simple look-up tables, radiation transfer models implement either two-stream approximations or the type of higher-order methods that are briefly described in section 2.4.

Many different two-stream approximations exist that differ in the phase function used. Meador and Weaver (1980) have shown that a unified description can be constructed for representing the different two-stream approximations. Three parameters (γ_1 , γ_2 , and γ_3 in Section 2.3) depending on the single scattering albedo and the phase function are sufficient to express the differences between these approximations. Toon *et al.* (1989) expanded upon the work of Meador and Weaver to include a formulation valid for thermal emission in local thermodynamic equilibrium, and developed a matrix method for treating the problem of an atmosphere with multiple parallel layers. Popular two-stream approximations mentioned by Meador and Weaver and Toon *et al.* include the Eddington (see Shettle and Weinman, 1970) and the quadrature scheme. (The quadrature scheme is the discrete-ordinate method at the lowest-order, see Liou, 1973 and 1974.) These schemes can be applied with or without the delta scaling technique proposed by Joseph *et al.* (1976). Meador and Weaver also described the hemispheric constant scheme (see Coakley and Chýlek, 1975) and a delta function approximation that is identical in results to the scheme of Coakley and Chýlek.

³ The number of Fourier components is usually restricted by assumptions over the functional form of the phase function.

Higher order methods differ mainly in the manner in which the Gaussian quadrature scheme is applied for zenith angle integration, and the method for treating the vertical dependence (dependence on the optical depth τ). Liou (1973) expanded upon Chandrasekhar's discrete-ordinate method. The $2n$ coupled Eqs (2.24) are expressed as a matrix equation. Solving the homogeneous matrix equation becomes a standard eigenvalue-eigenvector problem. Liou pointed out that Chandrasekhar's method for solving the homogeneous equation has mathematical and numerical ambiguities. Liou's matrix method for solving the homogeneous equation suppresses the ambiguities, and is based on expanding the matrix in polynomial form. Stamnes and Swanson (1981) solved a similar matrix equation by using a matrix transformation in eigenspace followed by matrix decomposition. Nakajima and Tanaka (1986) showed that the matrix equation can be transformed so that symmetric matrices are obtained that can be solved by decomposition. The advantage is that eigenvalue-eigenvector decomposition of symmetric matrices implies only real non-negative eigenvalues, and is simpler than asymmetric matrix decomposition. Nakajima and Tanaka also showed that this technique applied to a multiple parallel layer representation of the atmosphere is similar to the matrix-operator technique (see Plass *et al.*, 1973). Stamnes *et al.* (1988) found that the technique introduced by Nakajima and Tanaka degrades the numerical accuracy of the Stamnes and Swanson (1981) method, but is faster. Stamnes *et al.* decided to apply the Stamnes and Swanson procedure while introducing simplification (questionable?) in the mathematics.

With the increasing available computational power and increasing refinement of matrix decomposition algorithms, the computational cost associated with using higher-order radiation transfer models is less significant. For example, PHOTOGT, a computer model implementing the finite difference method (Lenoble, 1985) was used with $n = 9$ in tests and comparisons by Blindauer *et al.* (1996). (The finite difference method is similar to the discrete ordinate method described above.) STAR, a computer model implementing the discrete order and adding method of Nakajima and Tanaka was used with $n = 4, 6$ and 10 in a study by Ruggaber *et al.* (1994).

2.6 Selection of TUV for modeling radiation transfer

The *Tropospheric Ultraviolet-Visible radiation transfer model* (TUV) by Dr. Sasha Madronich of the National Center for Atmospheric Research in Boulder, Colorado has been selected for our treatment of radiative transfer in Air Quality Models (AQM). The method used in TUV is the delta-scaled Eddington two-stream approximation, which uses the following approximation for the phase function (see Joseph *et al.*, 1976):

$$p(\cos \theta) \equiv 2f \delta(1 - \cos \theta) + (1 - f)(1 + 3g' \cos \theta), \quad (2.25)$$

The first part of the right-hand term is a delta function in the forward direction, and the second part of the right-hand side is the form of the phase function for the Eddington approximation. f is the fraction of the light scattered in a peak in the forward direction represented by the delta function, and g' is the asymmetry parameter of the Eddington approximation *alone*. The asymmetry factor of the delta-scaled Eddington approximation is different because of the scaling. Code for other approximations is also available but was not used in the present study. Use of the delta-scaled Eddington two-stream approximation has the following advantages (see Lenoble, 1985):

- 1) Solutions of the transfer equation may be derived explicitly.
- 2) Analytic two-stream (and four-stream) solutions can be derived in closed forms.
- 3) The computer time required to achieve intensity and flux computations is small relative to other higher-order methods.

The low-order approximation used by TUV can introduce errors on the order of 3 to 10% according to Lenoble (1985). Given the limited knowledge of many input parameters and the sensitivities of the radiation intensity to these parameters, this level of error is acceptable.

TUV allows the definition of the absorbing and scattering characteristics of the atmosphere due to the following sources: gases (e.g., NO₂, SO₂, O₂, O₃), aerosols and clouds. The user can also define other parameters such as atmospheric pressure and vertical temperature profiles and ground albedo. In case this information is missing, realistic default values are provided.

Although there are other more sophisticated models including higher-order approximations for the discrete ordinate method (DISORT), the finite difference method (PHOTOGT) or the discrete order and adding method (STAR), they are computationally too demanding for the present application. (See Lenoble, 1985 for an overview of methods available to model radiation transfer).

2.7 Implementation Issues for Air Quality Models

The treatment of photolysis reaction rate coefficients developed in this study is designed to be implemented in the Urban Airshed Model (UAM-IV), the Flexible Chemical Mechanism version of UAM-IV (UAM-FCM), and the SARMAP Air Quality Model (SAQM). This section discusses how photolysis rates are calculated in the existing codes for these three models.

2.7.1 Calculation of photolysis rates in UAM-IV

The UAM-IV model accepts a schedule of NO₂ photolysis rate coefficients (k_1) for each day being modeled and calculates all other rates by multiplying internally stored factors by k_1 . The diurnal schedule of k_1 values is calculated in the UAM SUNFUNC preprocessor using k_1

estimates for various zenith angles at an elevation of 640 m above sea level, assuming relatively high aerosol loading and surface albedo. Because the photolysis rates for different species are driven by different portions of the solar wavelength spectrum, the model incorporates proportionality factors that vary with the solar zenith angle. These factors were calculated outside the UAM software system using a standard set of solar actinic flux estimates in conjunction with absorption cross-section and quantum yield data.

In UAM-IV, photolysis rates are calculated in subroutine PHOTOL, which is called from subroutines SSIC (calculates initial concentrations of steady state species), SSBC (calculates boundary concentrations of steady state species), and STEP34 (controls the sequence of vertical transport and chemistry calculations during the numerical integration process). Subroutine PHFACT is called when aerosols are simulated to provide an estimate of their influence on the vertical spatial variation of the photolysis rate constants.

2.7.2 Calculation of photolysis rates in UAM-FCM

UAM-FCM was developed to facilitate the input of all aspects of a chemical mechanism into the Airshed Model. As part of implementing the FCM interface, modifications were made to the numerical integration procedure employed in UAM-IV. The routine to calculate the photolysis rates was taken from the integration module of the SAPRC Chemical Mechanism Preparation software and was modified to use the solar zenith angle. A new routine was added that calculates photolysis rates for different zenith angles and stores these resulting values in a table that can then be used to calculate photolysis rates during the course of a model run for any zenith angle by interpolation.

For the calculation of photolysis rates, the user must provide as inputs the product of the absorption cross-section and quantum yield for various user-specified photolytic wavelengths for each photolysis reaction. In addition, the user must supply a file containing actinic flux data for use in the calculation of photolysis rates from the action spectra data. If such a file is not provided, then a default set of actinic flux data are used derived from the work of Peterson (1976). These default data represent light spectra (expressed in terms of photons $\text{cm}^{-2} \text{min}^{-1}$ in specified wavelength intervals) for the solar zenith angles of 0, 10, 20, 30, 40, 50, 60, 78, 86, and 89°.

In UAM-FCM, the original treatment of photolysis rates (subroutine PHOTOL) has been replaced with a new subroutine, NEWPHK. However, the basic sequencing of the photolysis rate constant calculation is similar to that in UAM-IV.

2.7.3 Calculation of photolysis rates in SAQM

The photolysis rate constants in SAQM are calculated based on the integration of the molecular absorption cross-section, the quantum yield, and the actinic flux. A radiative transfer model is employed to characterize the effects of atmospheric scattering and absorption processes based on the work of Demerjian *et al.* (1980). Madronich's radiation transfer model (TUV) has been adopted to calculate photolytic rate constants for the CB-IV and SAPRC chemical mechanisms, using mechanism-specific absorption cross-section and quantum yield data provided with the mechanisms. The radiative transfer model employs the delta-Eddington approximation for the light scattering and absorption calculations by molecules and aerosols. The input data for the model calculation include the extraterrestrial solar irradiance, O₂ and O₃ absorption cross-sections, Rayleigh scattering cross-sections, seasonal and latitudinal varying vertical profiles of air density and temperature, aerosol attenuation coefficients, ozone profiles scaled to total ozone column, and wavelength dependent surface albedo.

In the SAQM code, photolysis rates are calculated in subroutine PHOT, which is called from subroutine CHEM (controls the chemistry integration steps), which in turn is called from subroutine DRIVERN (controls the overall sequencing of the numerical integration process).

Based on the review of UAM-IV, UAM-FCM, and SAQM, the following guidelines were followed during the development of the photolysis reaction rate module in this study.

- 1) The photolysis rate module should be designed to calculate rate constants in a column of grid cells at specified heights. Means should be provided for using "local" values of the pollutant concentration field and meteorological variables, as appropriate, in determining photolysis rates.
- 2) The photolysis module should be implemented in UAM-IV, UAM-FCM, and SAQM in a manner that allows the user to choose whether to employ the original photolysis treatment or that developed in this study.
- 3) If there is a significant computational burden associated with the usage of the photolysis module, sensitivity studies or other analyses should be carried out to provide a means for determining how frequently (or under what conditions) the module should be called in the normal course of the numerical integration procedure.

2.7.4 Photolysis reactions in the SAPRC and CB-IV mechanism

Different photochemical mechanisms are implemented in the Air Quality Models of interest. While similar, the photolysis reactions included in these mechanisms are not identical. The photolysis reactions used in the SAPRC97 and CB-IV mechanisms are summarized in Table 2.1

Reactant name	Reactant	Products	SAPRC	CB-IV
NO ₂	NO ₂ + hv	→ NO + O	X	X
NO ₃	NO ₃ + hv	→ NO + O ₂	X	
NO ₃	NO ₃ + hv	→ NO ₂ + O	X	
NO ₃	NO ₃ + hv	→ 0.89 NO ₂ + 0.89 O + 0.11 NO		X
Ozone	O ₃ + hv	→ O + O ₂	X	X
Ozone	O ₃ + hv	→ O(¹ D) + O ₂	X	X
HONO	HONO + hv	→ OH + NO	X	X
H ₂ O ₂	H ₂ O ₂ + hv	→ 2 OH	X	X
HCHO	HCHO + hv	→ 2 HO ₂ + CO	X	X
HCHO	HCHO + hv	→ H ₂ + CO	X	
HCHO	HCHO + hv	→ CO		X
CO ₂ H	-OOH + hv	→ HO ₂ + OH	X	
High molecular weight aldehyde	ALD2 + hv	→ CO + 2 HO ₂ + HCHO + XO ₂		X
CCHO	CCHO + hv	→ CO + HO ₂ + HCHO + RO ₂ -R + RO ₂	X	
RCHO	RCHO + hv	→ CCHO + RO ₂ -R + RO ₂ + CO + HO ₂	X	
Acetone (C ₃ H ₆ O)	ACET + hv	→ CCO-O ₂ + HCHO + RO ₂ -R + RCO ₃ + RO ₂	X	
High molecular weight aromatic oxidation ring fragment	OPEN + hv	→ C ₂ O ₃ + HO ₂ + CO		X
Methyl-glyoxal (C ₃ H ₄ O ₂)	MGLY + hv	→ C ₂ O ₃ + HO ₂ + CO		X
Methyl-ethyl-ketone (C ₄ H ₈ O)	MEK + hv	→ CCO-O ₂ + CCHO + RO ₂ -R + RCO ₃ + RO ₂	X	

Table 2.1: Photolysis reactions in SAPRC97 (Carter, 1997) and CB-IV (Gery *et al.*, 1992)

Reactant name	Reactant	Products	SAPRC	CB-IV
Glyoxal (OHC-CHO)	GLY + hv	$\rightarrow 0.8 \text{ HO}_2 + 0.45 \text{ HCHO} + 1.55 \text{ CO}$	X	
Glyoxal	GLY + hv	$\rightarrow 0.13 \text{ HCHO} + 1.87 \text{ CO}$	X	
Methyl-Glyoxal	MGLY + hv	$\rightarrow \text{HO}_2 + \text{CO} + \text{CCO-O}_2 + \text{RCO}_3$	X	
Methyl-Glyoxal	MGLY + hv	$\rightarrow \text{HO}_2 + \text{CO} + \text{CCO-O}_2 + \text{RCO}_3$	X	
Benzaldehyde (BZCHO)	BALD + hv	$\rightarrow 7 \text{ -C (Lost carbon)}$	X	
Aromatic product 2	AFG2 + hv	$\rightarrow \text{HO}_2 + \text{CO} + \text{CCO-O}_2 + \text{RCO}_3$	X	
Aromatic product 1	AFG1 + hv	$\rightarrow \text{HO}_2 + \text{HCOCO-O}_2 + \text{RCO}_3$	X	

Table 2.1 (continued): Photolysis reactions in SAPRC97 and CB-IV

2.7.5 Elevation grid treatment in Air Quality Models

The radiation transfer model selected for the computation of photolysis rate coefficients (see section 2.6) uses an elevation grid that is specified in kilometers. The elevation grid used for air quality modeling is often different, as discussed below. When the elevation grid used by the AQM is not defined in the same way than the elevation grid in the radiation transfer model, an appropriate mapping needs to be accomplished. We have reviewed the treatment of the elevation grid in UAM-IV, UAM-FCM, and SAQM.

The vertical grid structure in UAM and UAM-FCM is comprised of two sets of cells: one set resides between the ground and the so-called diffusion break (typically the base of an elevated inversion layer) and the other set resides from the diffusion break to the user-specified top of the modeling domain (typically spatially invariant, set at 2-3 km above the ground). The user specifies the number of cells both below and above the diffusion break (e.g., three cells below and two cells above). In addition, the user also specifies a minimum cell thickness for cells in each of these two layers (typically 25-50 m). The cells in each layer are equally spaced and subject to the minimum cell thickness. The user provides an input file with spatially and temporally varying mixing heights (*i.e.*, the height from the ground to the diffusion break). The

height from the ground to the top of the modeling domain can also vary spatially, but is typically set to a fixed value.

The SAQM vertical grid structure employs a σ -coordinate system, where

$$\sigma = \frac{p - p_{\text{top}}}{p_s - p_{\text{top}}} \quad (2.25)$$

and p is the pressure where σ is evaluated, and p_s and p_{top} are the pressure at the surface and the top of the modeling domain, respectively. The model also uses a surface layer submodel, which overlaps the bottom grid layer with three cells. Table 2.2 summarizes the pressure and height of each level assuming a 1000 hPa surface and standard atmosphere.

Level Index	σ -Index	Standard Pressure (hPa)	Standard Height (m)
15	0.000	100	16170
14	0.156	240	10540
13	0.326	393	7210
12	0.464	518	5210
11	0.600	640	3610
10	0.740	766	2190
9	0.814	833	1510
8	0.866	879	1070
7	0.902	912	770
6	0.918	926	640
5	0.934	941	510
4	0.950	955	390
3	0.966	969	260
2	0.980	982	150
1	0.992	993	60
a	0.996	996	30
b	0.9985	999	10
0	1.000	1000	0

Table 2.2: Discretization of the grid using σ -coordinates in SAQM

3 Photolysis Sensitivity to Radiative Transfer Parameters

Many factors influence the radiation transfer in the atmosphere, and these factors are parameters that are inputs to the radiation transfer model TUV that was chosen for this study (see section 2.6). The following input parameters must be defined in TUV:

- 1) General parameters such as date, time, time zone, longitude, latitude, and solar zenith angle.
- 2) Elevation grid, *i.e.*, the vertical column structure the program uses for the computations.
- 3) Wavelength grid, *i.e.*, the wavelength bins the program uses for the computations.
- 4) Air pressure.
- 5) Absorption and scattering by aerosols.
- 6) Absorption and scattering by clouds.
- 7) Ground albedo.
- 8) Air temperature.
- 9) Absorption by ozone.
- 10) Absorption by SO₂.
- 11) Absorption by NO₂.

Sensitivity analysis was performed to help determine which of these parameters are most influential when using TUV in the framework of an AQM. The parameters that can vary spatially and temporally in an unpredictable manner are items 4–11 in the list above. Sensitivity analysis was performed on parameters 5 and 7–11. Situations when clouds are present can be very complex because of the horizontal non-homogeneity of clouds. Because of this non-homogeneity, clouds can produce large and rapid radiation flux variations. Since TUV considers only one spatial dimension (elevation), partial cloud cover and the effects of cloud edges cannot be represented in this model. However, it is possible to include some homogeneous cloud layers that are treated similarly to the aerosols. Because of the difficulty of treating clouds appropriately, the sparsity of data, and since photochemical air pollution is often linked to stagnant high-pressure systems, the scope of this study was limited to clear-sky situations. Air pressure (item 4) can vary depending on the meteorological conditions. However, for stagnant high-pressure systems, temporal and spatial variations in air pressure are limited, and the important air pressure variations that must be considered are those due to changes in ground elevation.

Many photolysis reactions are considered in AQMs (see section 2.7.4). We selected a set of photolysis reactions that are influential in tropospheric photochemical ozone production. A

number of sensitivity studies (for example, Falls *et al.*, 1979, Milford *et al.*, 1992, Gao *et al.*, 1995, 1996, Yang *et al.*, 1995, 1996, Vuilleumier *et al.*, 1997, Bergin *et al.* 1998) have examined the sensitivity of ozone production to various chemical reactions, and have identified the photolysis of nitrogen dioxide (NO₂), formaldehyde (HCHO) and nitrous acid (HONO) as being the most important photochemical reactions. We also included the photolysis of ozone (O₃) that forms monoatomic oxygen in the singlet-D state [O(¹D)], because it both destroys, and reacts with H₂O to form OH radicals needed for tropospheric ozone formation. Table 3.1 summarizes the reactions considered in the sensitivity analysis.

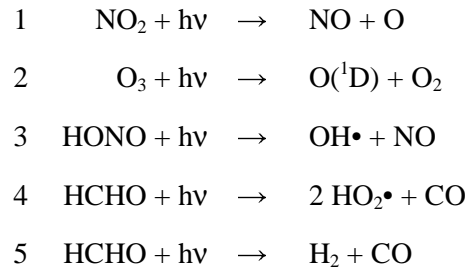


Table 3.1: Reactions considered in sensitivity analysis

Sensitivity analysis was performed by varying parameter values in a systematic manner, and executing a radiation transfer simulation for each set of parameter values. The parameters that were considered for sensitivity analysis were

- 1) The total aerosol optical depth: the optical depth is a measure of the opacity of the atmosphere to light (see Section 2.2). Light extinction can be caused by different materials such as the main gases in the air, trace gases (ozone, SO₂, NO₂...), aerosols, clouds, etc. The optical depth is additive, i.e., the combined effect of extinction by all materials can be represented as the sum of the optical depths due to each material. The total aerosol optical depth represents the extinction caused by the aerosol over the full height of the atmosphere (vertically). For the wavelength of interest (the near UV), the aerosol optical depth decreases with increasing wavelength. At 340 nm, typical total aerosol optical depths are on the order of 0.3.
- 2) The aerosol single scattering albedo: the aerosol single scattering albedo indicates what fraction of light is scattered (the rest is absorbed) when light is extinguished by aerosol.
- 3) The aerosol asymmetry factor: the asymmetry factor indicates whether the light is scattered in the forward or backward direction. It is the intensity-weighted average of the cosine of the scattering angle: $g = \frac{1}{2} \int_0^\pi \cos \theta p(\theta) \sin \theta d\theta$. Where θ is the scattering

angle and $p(\theta)$ is the phase function indicating the fraction of light scattered at the angle θ . The asymmetry factor is 1 for total forward scattering, and -1 for total backward scattering.

- 4) The ground albedo: the ground albedo indicates the fraction of light reflected by the ground surface.
- 5) The air temperature.
- 6) The total ozone column: the total ozone column indicates the height of a column of pure ozone at standard pressure and temperature that would include the same amount of ozone than encountered going through the full height of the atmosphere. This quantity is combined by TUV with a typical ozone elevation profile and wavelength-dependent ozone cross section to yield the ozone optical depth.
- 7) The total SO₂ column. Similar to the ozone column, this quantity yields the SO₂ optical depth.
- 8) The total NO₂ column. Similar to the ozone column, this quantity yields the NO₂ optical depth.

For each of these parameters, a reasonable nominal value, and a range of variation were chosen (see Table 3.2). The range of variation chosen was not always the full possible range, but represented a range representative of the conditions encountered in the 1997 Southern California Ozone Study (see section 4). For each parameter that was varied, five different values were used (the nominal value, the two extrema of the variation range, and the two midpoints between the extrema and the nominal value). Five simulations were performed with the five values, while the other parameters were kept at their nominal values. The photolysis rate coefficients for the reactions listed in Table 3.1, in the surface air layer and for a solar zenith angle of 10° were recorded, and a 2nd-order polynomial was fit to express the relationship between the rate coefficient and the sensitivity parameter. The 2nd-order polynomial was used to determine the sensitivity of the reaction rate coefficient to the sensitivity parameter with respect to the parameter nominal value. Figure 3.1 shows the NO₂ photolysis rate coefficient sensitivity to the aerosol total optical depth (a), and the O₃ photolysis rate coefficient sensitivity to the total ozone column (b).

Parameter	TUV default	Nominal value	Variation range	
Aerosol total optical depth	0.38	0.38	0.19	0.57
Aerosol single scattering albedo	0.99	0.85	0.75	0.95
Aerosol asymmetry factor	0.61	0.60	0.50	0.70
Ground (surface) albedo	0.10	0.10	0.00	0.20
Air temperature (surface ^{a)} (K)	288.15	288.15	263.15	313.15
O ₃ total column (Dobson Units)	349.82	300.00	280.00	320.00
NO ₂ total column (molec cm ⁻²)	$2.69 \cdot 10^{10}$	$2.69 \cdot 10^{10}$	0.00	$5.38 \cdot 10^{10}$
SO ₂ total column (molec cm ⁻²)	$2.69 \cdot 10^{10}$	$2.69 \cdot 10^{10}$	0.00	$5.38 \cdot 10^{10}$

Table 3.2: Nominal parameter values and ranges of variation used in sensitivity analysis

^{a)} Only surface air temperature is given in the table, but air temperature was varied at all elevations simultaneously (see section 3.2).

For facilitating comparison of the sensitivities, all sensitivity coefficients were normalized, *i.e.*, the sensitivity coefficients express the relative variation of the photolysis reaction rate coefficient in percent, with respect to percent parameter variation. All sensitivity coefficients evaluated with respect to the parameter nominal value are given in Table 3.3, except for the NO₂ and SO₂ total column values. The normalized sensitivities of all the photolysis rate coefficients considered to the latter two parameters were smaller than $5 \cdot 10^{-3}$ (in absolute value).

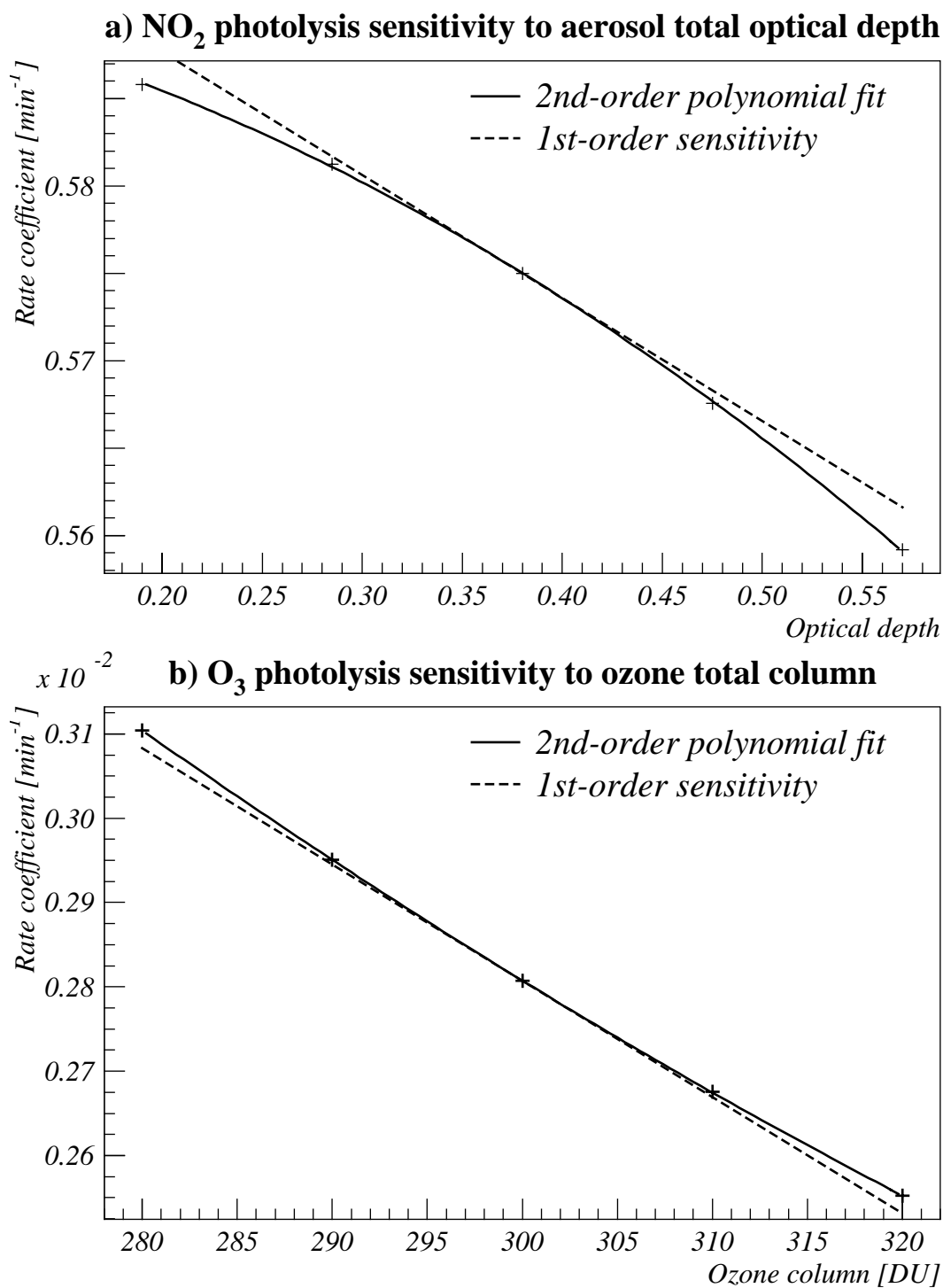


Figure 3.1: Photolysis rate coefficients normalized sensitivity to radiative transfer model parameters.

Reactions	Aerosol			Temperature	Ground albedo	O ₃ total column
	tot. optical depth	single scat. albedo	asymmetry factor			
NO ₂ + hv → NO + O	-0.047	0.470	0.063	-0.001	0.163	-0.017
O ₃ + hv → O(¹ D) + O ₂	-0.106	0.578	0.087	-0.055	0.154	-1.475
HONO + hv → OH• + NO	-0.054	0.494	0.066	-0.001	0.163	-0.007
HCHO + hv → 2 HO ₂ • + CO	-0.091	0.579	0.078	-0.022	0.159	-0.397
HCHO + hv → H ₂ + CO	-0.078	0.555	0.073	-0.011	0.161	-0.163

Table 3.3: Normalized sensitivity coefficients

3.1 Sensitivity to the aerosol parameters

The largest normalized sensitivities are the sensitivities to the single scattering albedo (refers to the fraction of light scattered vs. absorbed following interaction of light with a particle). These sensitivities are around 0.5 indicating that a 10% change in single scattering albedo will induce a 5% change in photolysis rate coefficients. Whereas black carbon is thought to be the only strongly absorbing aerosol component in the visible portion of the spectrum, there are unresolved questions about absorption of UV radiation by organic aerosols. According to expert judgement (Madronich, 2000), this parameter is likely to be in the range 0.75–0.95 in urban areas.

Sensitivity to the aerosol total optical depth (refers to the total amount of aerosols present in a vertical column) is between -0.05 and -0.1 depending on the reaction. All the sensitivities are negative implying that an increase in aerosol total optical depth would lead to a decrease in photolysis rate coefficients (in the surface layer). Dickerson *et al.* (1997) showed that the sign of this effect can change if the aerosol is purely scattering; in the present analysis the aerosol is assumed to have a single scattering albedo of 0.85. The sensitivity coefficients are not large, but the aerosol total optical depth is a parameter that can show large variations (see section 4.1.3). The aerosol asymmetry factor (fraction of light forward vs. back-scattered by aerosols) does not appear to be very influential, indicated by the low magnitude of the sensitivity coefficients, and because its range of likely values is thought to be limited (Madronich, 2000).

3.2 Sensitivity to the air temperature

To understand the dependence of photolysis rate coefficients on temperature, it is useful to consider Eq. (2.2) used to compute the J values:

$$J_x = \int_0^\infty \sigma_x(\lambda) \varphi_x(\lambda) F(\lambda) d\lambda$$

The factors in the integral in Eq. (2.2) [$\sigma_x(\lambda)$, $\varphi_x(\lambda)$ and $F(\lambda)$] may each exhibit temperature dependence. We use the term direct dependence, for the temperature dependence of $\sigma_x(\lambda)$ and $\varphi_x(\lambda)$, because it is specific to each reaction, and use the term indirect dependence for the temperature dependence of $F(\lambda)$, because it is common to all reactions. The temperature dependence of the ozone photolysis depends principally on the first two factors, and the first factor [$\sigma_{O_3}(\lambda)$] influences the third, $F(\lambda)$.

Since the ozone photolysis cross-section depends on temperature, the amount of light absorbed by ozone during the radiation transfer is temperature dependent as is the actinic flux. While the direct temperature dependence resulting from the ozone cross-section affects only ozone photolysis, the indirect dependence affects other photolysis reactions that also depend on $F(\lambda)$ in the relevant wavelength range.

TUV uses two data sets for the ozone cross-section that are treated independently in the program. The first data set [$\sigma_{O_3}^a(\lambda)$] is used to evaluate light absorption by ozone for the purpose of calculating radiation transfer. The second data set [$\sigma_{O_3}^p(\lambda)$] is used to evaluate the photolysis rate coefficient via Eq. (2.2). The reason for having two separate data sets is that TUV was designed to allow flexibility in the choice of supporting data. Consequently, one can choose to use a set of photolysis reactions that does not include the photolysis of the principal light-absorbing gases. Whether the user chooses to include ozone photolysis in the reactions of interest or not, the simulation program needs the light absorption cross-section of ozone to be defined for determining the actinic flux. The data set for ozone light absorption cross-section [$\sigma_{O_3}^a(\lambda)$] is dependent on the temperature regardless of how $\sigma_{O_3}^p(\lambda)$ is defined. Specifically, the current ozone cross-section data set for the ozone photolysis rate determination [$\sigma_{O_3}^p(\lambda)$] (data from the SAPRC-97 mechanism, see Carter, 1997) is independent of temperature. Consequently, ozone photolysis temperature sensitivity will not respond to the effect of the direct dependence, but only to that of indirect dependence.

To investigate the effect of temperature on the photolytic rate coefficients, the temperature of the lower atmospheric layers was varied in the following way:

- The temperature at elevations 0, 1 and 2 km was varied between ± 25 K of the nominal layer temperature,

- between ± 20 K of the nominal layer temperature at elevations 3, 4 and 5 km,
- between ± 10 K of the nominal layer temperature at elevations 6, 7 and 8 km, and
- between ± 5 K of the nominal layer temperature at elevations 9, 10 and 11 km.

The influence of the air temperature on photolysis is small as shown by the sensitivities. As expected, the ozone photolysis sensitivity is the largest. This is because the absorption spectra from the two data sources for the cross-section are similar, each with a sharp drop for wavelengths longer than 330 nm. The light-absorbing cross-section of ozone and the ozone photolysis rate cross-section are defined independently with the former temperature-dependent and the latter not dependent. Ignoring the direct temperature dependence of the ozone cross-section results in an overestimation of the sensitivity. In cases where the direct temperature dependence is considered, a cancellation would occur. On one hand, a temperature change that would increase the ozone absorption cross-section would result in an increased ozone photolysis rate *given a fixed actinic flux*. On the other hand it would decrease the actinic flux as a result of increased light absorption by ozone. Only the second effect is present in this study resulting in the observed negative sensitivity.

3.3 Sensitivity to the ground albedo

The sensitivities to ground albedo are all similar and of medium size in magnitude. The sensitivities are all positive because an increase of the ground albedo results in an increase of the light reflected by the surface. The default ground albedo in TUV is treated as independent of wavelength; consequently all reactions are affected similarly. Since the nominal value of the surface albedo is low (0.1) the amount of light reflected by the surface is small, and the effect of surface albedo variations is limited. Larger surface albedo would result in larger sensitivities. However, only a limited range of ground albedo values from 0.07 to 0.20 is relevant for southern California (see section 5.3). The ocean has low albedo except when the sun is near the horizon. The most reflective surfaces are urbanized areas and desert. The forested areas in the San Gabriel, San Bernardino, Santa Ana, and San Jacinto Mountains have low albedo. Large values of the ground albedo may only occur when the modeling domain includes snow-covered areas, which is not the case in this study.

3.4 Sensitivity to the total ozone column

The sensitivities to the ozone total column vary strongly depending on the reaction. This is a result of the strong wavelength dependence of the ozone absorption spectrum. Ozone is an influential light-absorbing gas at wavelengths shorter than 330 nm, and its absorption cross-

section exhibits a sharp drop above 300 nm (Seinfeld and Pandis, 1997, pp. 143–146). The ozone photolysis sensitivity to the total ozone column is large as expected because of the similar absorption spectra. The influence of the total ozone column on formaldehyde photolysis is also significant, but of limited importance for calculating nitrous acid or nitrogen dioxide photolysis rates. Large changes of total ozone column are believed to be restricted to relatively high latitudes, and are more pronounced in the Southern Hemisphere (e.g., Antarctic ozone hole). In California, variations of the total ozone column should be limited relative to the nominal value.

In many cases, the influence of a parameter is difficult to evaluate based solely on the sensitivity analysis. Information is often scarce about the range of variation associated with a parameter. In such cases, the relative importance of the parameters can only be evaluated by analyzing measured data. Many radiation measurements were made during the 1997 Southern California Ozone Study, and this information can be used to help resolve such questions.

4 Variability in Optical Depth during SCOS97

A large-scale field study of ozone formation in Southern California (SCOS97-NARSTO) was conducted during summer 1997, to improve understanding of the emissions, atmospheric chemistry, and meteorological conditions leading to the severe photochemical air pollution problems in the Los Angeles area. Our focus in this chapter is the analysis of solar UV irradiance measurements made at two Southern California sites experiencing different levels of air pollution. Photochemical reactions depend on the solar actinic flux while solar irradiance is the quantity measured in this study. Actinic flux and solar irradiance are related by a geometric factor, *i.e.*, the irradiance is weighted by the cosine of the incident zenith angle, while the actinic flux is not (see Section 2.1). Because it depends on the angular distribution of the radiance, the relationship between actinic flux and irradiance can be complex, and is an active area of research. For more details the reader is referred to Madronich (1987) who describes the relationship between these two quantities in detail.

We have analyzed ground-based UV irradiance data from the SCOS97 field campaign at Riverside and Mt Wilson, California. We have computed total optical depths (*i.e.*, the solar direct beam differential extinction rate, see section 2.2 and 4.1.1) and determined their distribution for the period extending from July to the end of October 1997. We also computed the correlation coefficients between pairs of optical depths measured at different wavelengths, and used principal component analysis (PCA) to identify the underlying factors responsible for the variability observed in the optical depths. If this variability is accounted for in the calculation of actinic flux, the uncertainty in photolysis rates in air quality models can be reduced and our calculation of ozone formation improved. Principal component analysis allows us to attribute the optical depth variability mainly to concentration changes in aerosols and marginally to changes in the ozone column.

In section 4.1, we describe how the irradiance data were acquired, and explain the algorithm used to obtain total optical depths from the irradiance. We also specify the selection criteria that were applied to the data set, and discuss the optical depth distributions. In section 4.2, we present the statistical methods that were used to analyze optical depth variability. We show how correlation coefficients were obtained from the optical depth distributions, and how PCA was applied to identify underlying factors responsible for the optical depth variability. The results of the statistical analysis are discussed at the end of section 4.2.

4.1 SCOS97 Data

4.1.1 Experimental Measurement

The irradiance data used in this study were acquired during the 1997 Southern California Ozone Study (SCOS97) at two sites selected for intensive monitoring. The first site is at Riverside, CA (260 m a.s.l., latitude 33.94°N, longitude 117.40°W) in the Los Angeles metropolitan area, and is characterized by frequent occurrences of severe air pollution episodes. The second site is Mt Wilson, CA (1725 m a.s.l., latitude 34.23°N, longitude 118.07°W) approximately 70 km northwest of Riverside, a mountainous site located above much of the urban haze layer. The measurement period extended from 1 July to 1 November 1997.

Solar UV irradiance reaching the ground was measured at seven wavelengths by two prototype Yankee Environmental Systems (Turners Falls, MA) UV multi-filter rotating shadow-band radiometers (MFRSR) (Bigelow and Slusser, 2000) SN 231 at Riverside and 232 at Mt Wilson. These radiometers have 2 nm nominal full-width half-maximum filters whose center wavelengths are 300.4, 305.7, 312.0, 318.1, 325.9, 332.9 and 367.8 nm. Bigelow *et al.* (1998) have shown that integrated out-of-band light contamination is less than 0.5%. A shadow-band blocks the direct solar beam to yield diffuse horizontal irradiance, which is subtracted from the total horizontal irradiance to give direct horizontal irradiance. In order to obtain absolute measurements of the solar irradiance, calibration factors should be used. However, optical depth can be computed using uncalibrated relative irradiances (see below). From this point, we will use the term “irradiance” to refer to the uncalibrated quantity. The direct normal solar irradiance used for computing total optical depths (see below) is obtained by dividing the direct horizontal irradiance by the cosine of the solar zenith angle and then applying angular corrections previously measured in the laboratory (Harrison and Michalsky, 1994). Measurements at the seven wavelengths were made simultaneously every 20 seconds and nine such measurements were averaged to form a 3-minute average. The averaged data were stored in a data logger until transferred by modem to the Colorado State University data facility each night.

Total optical depths were deduced from the irradiance data. The optical depth, a measure of the opacity of the atmosphere to light (see Section 2.2), is part of the exponent of the Beer-Lambert-Bouguer law.

$$\begin{aligned} I(t) &= R^2 I_0 \cdot \exp\left(-\sum_i m_i(t) \cdot \tau_i(t)\right) \\ \Rightarrow \ln(R^2 I_0) - \ln(I(t)) &= \sum_i m_i(t) \cdot \tau_i(t) \end{aligned} \quad (4.1)$$

where $I(t)$ is the direct normal solar irradiance at time t (I_0 is the extra-terrestrial irradiance), R is the Earth-to-Sun distance in astronomical units, and m_i and τ_i are the optical mass factors and optical depths for the different light-absorbing and scattering materials in the atmosphere. The sum over the different materials reflects that fact that light extinction can be caused by different materials such as the main gases in the air, trace gases (ozone, SO₂, NO₂...), aerosols, clouds, etc. The optical depth is additive, *i.e.*, the combined effect of extinction by all materials can be represented as the sum of the optical depths due to each material. The optical mass factor represents the ratio between the path length of the solar direct beam and the path length of a vertical beam. It is used because the optical depth is defined vertically (see Section 2.2). Optical mass factors can be different for different materials, because the direct solar beam is not straight but curved by refraction. The different elevation profiles of the light-absorbing and scattering materials in the atmosphere can result in slightly different optical mass factors. The expression in Eq. (4.1) is often approximated with (see Schotland and Lea, 1986):

$$\ln(R^2 I_0) - \ln(I(t)) = m_e(t) \cdot \tau(t) \quad \text{with } m_e(t) = \frac{\sum_i m_i(t) \cdot \tau_i(t)}{\sum_i \tau_i(t)} \quad (4.2)$$

where $m_e(t)$ is the effective air mass factor (a weighted average of the optical mass factors), and $\tau(t)$ is the total optical depth. When the value of $\ln(R^2 I_0)$ is known, an instantaneous total optical depth can be computed for each individual direct irradiance measurement. Values need not be known with an absolute calibration, but need to be known only relatively. If $V(t)$ is the radiometer reading (in mV) corresponding to the measurement $I(t)$, one needs only to know the value V_0 corresponding to $R^2 I_0$ to calculate the instantaneous total optical depth:

$$\tau(t) = \frac{\ln V_0 - \ln V(t)}{m_e(t)} \quad (4.3)$$

Absolute calibrations were not available for the prototype UV multifilter radiometers used in SCOS97. Thus, the Langley plot method (see Slusser *et al.*, 2000) was used to determine the $\ln V_0$ intercept. The direct normal solar irradiance data measured during a 2-4 hour period was expressed as a function of the air mass factor traversed by the direct solar beam. The time period were chosen such that the air mass factor ranged from 1.2 to 2.2 at the shorter wavelengths (300, 306, and 312 nm), and from 1.5 to 3 at the longer wavelengths. The $\ln V_0$ intercept was obtained by extrapolating a linear regression of the logarithm of irradiance as a function of air mass factor to the zero air mass axis. The Harrison and Michalsky algorithm (1994) was used to select periods for which the Langley method was applicable. Two modifications were made to the Harrison and Michalsky algorithm: 1) the air mass factor ranges are different (see above);

2) Harrison and Michalsky requested that the standard deviation of $\ln I$ around the regression line be less than 0.006, while we used 0.009. This method has been evaluated in numerous publications via intercomparisons to other optical depth measuring devices beginning with Harrison and Michalsky's original objective algorithm paper and most recently in an intercomparison of four solar radiometers at the ARM site in Oklahoma (Schmid *et al.*, 1999). It has been extended to UV wavelengths by numerous researchers including Bigelow and Slusser (2000) and Slusser *et al.* (2000).

Computation of the optical depths and $\ln V_0$ intercepts requires the effective air mass factor $m_e(t)$ to be known. For computing $m_e(t)$, one needs to know at every desired time, the optical mass factors and optical depths for all materials responsible for light extinction in the atmosphere. Missing this information, we replaced $m_e(t)$ by the air mass factor due to Rayleigh scattering $m_R(t)$. These terms (m_e and m_R) are different because of the difference in elevation profiles of the light-absorbing and scattering materials in the atmosphere, and replacing one by the other introduces a bias. These differences have been discussed extensively in the literature (e.g., Thomason *et al.*, 1983 or Tomasi *et al.*, 1998). The elevation profile of ozone is one of the profiles that differs most from the profile of the uniformly mixed atmospheric gases that is used for evaluating Rayleigh scattering. To estimate an upper limit on the bias that was introduced when replacing $m_e(t)$ by $m_R(t)$, we computed it assuming only ozone and uniformly mixed atmospheric gases, a 300 DU total ozone column, and a standard atmosphere with a sea-level pressure of 1013 hPa. At Mt Wilson and Riverside, the bias on the optical depth is less than 2% at $\lambda = 300$ nm, and for $m_R = 2$, considering the effect of replacing $m_e(t)$ by $m_R(t)$ in Eq. 2 and in the determination of $\ln V_0$. At all other wavelengths the bias is smaller, since ozone has a weaker influence at higher wavelengths.

For each wavelength and site, the average $\ln V_0$ values were applied to all days assuming that the variations in extraterrestrial irradiance (I_0) were negligible⁴, and that the instruments were stable. In order to test these assumptions, the distributions and time series for $\ln V_0$ were analyzed. A downward trend with time was visible in the time series for some wavelengths and sites (for example, see Figure 4.1a). Linear regressions were computed for each time series. When the linear correlation coefficient (r) was greater than 1/3 (in absolute value) the downward trend was characterized as significant and the linear regression was used to compensate for it. In cases where the trend is significant ($|r| > 1/3$), the value of the regression line for the desired time is used instead of the average $\ln V_0$. Bigelow and Slusser (2000) and Slusser *et al.* (2000) also observed a similar drift with the same type of radiometer. Bigelow and Slusser are unsure of the

⁴ The spectral irradiance of the sun between 300 and 400 nm is constant within 0.5% over an eleven-year solar cycle (Lean *et al.*, 1997).

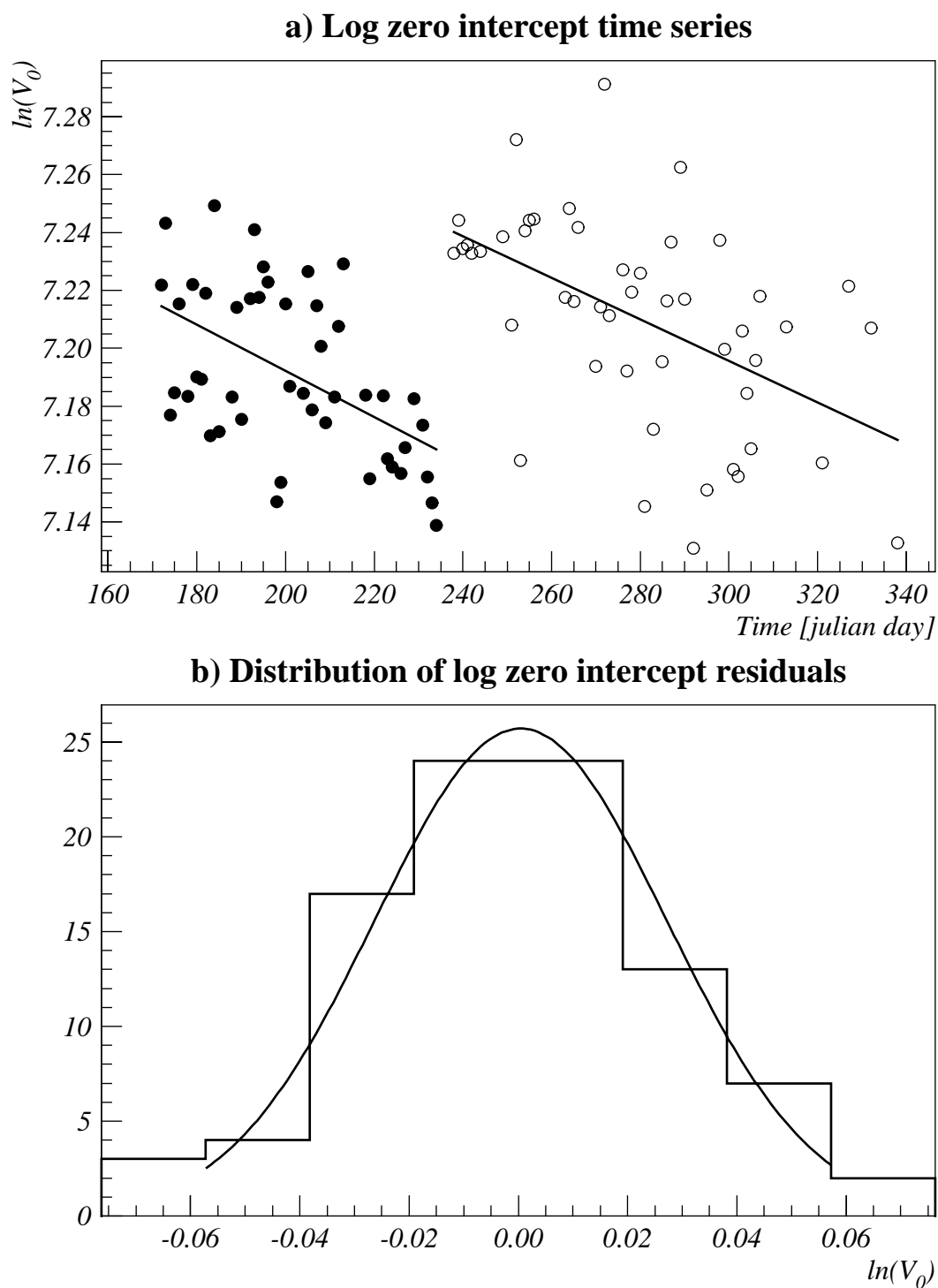


Figure 4.1: Logarithm of zero intercept ($\ln V_0$) time series and residual distribution for Mt Wilson at $\lambda = 333$ nm. V_0 is the value in mV that would be obtained by measuring the extraterrestrial irradiance with the radiometer used in this study.

cause of this minor drift. A noticeable feature occurs for the $\ln V_0$ time series for data taken at Mt Wilson. When a trend is significant at Mt Wilson, the time series are split in two distinct groups with a recovery around Julian day 234. On this day, the Mt Wilson radiometer was moved because of concerns about the original location.

The distributions of the residuals between the individual values of $\ln V_0$ and the regression line (significant trend) or the average (insignificant trend) were used to check the quality of the determination of $\ln V_0$. When the number of residuals is sufficient (larger than 60), a Gaussian can be fitted to describe the residual distribution (see Figure 4.1b). For each case with more than 60 residuals, the data look consistent with a normal distribution. The uncertainty on $\ln V_0$ can be computed using the residual distributions providing the following assumptions are true:

- 1) The uncertainty in the determination of $\ln V_0$ comes from the variability in the atmospheric conditions and not from the instability of the detector.
- 2) The uncertainty is statistically distributed with a normal distribution around the true value of $\ln V_0$.

The first assumption is warranted because the multifilter shadowband radiometers are stable, and random variations due to the instruments are negligible compared to variation in atmospheric optical properties (Bigelow and Slusser, 2000). The second assumption is warranted since all residual distributions with more than 60 events are compatible with a normal distribution. Thus, a 95% confidence level interval u can be computed for $\ln V_0$:

$$\overline{\ln V_0} - u \leq \ln V_0 \leq \overline{\ln V_0} + u, \quad u = t_{025} \frac{s'}{\sqrt{n}} \quad \text{at 95\% confidence level,} \quad (4.4)$$

where $\overline{\ln V_0}$ is the average $\ln V_0$ or the value obtained with linear regression, t_{025} is the critical value at a 95% confidence level for the Student-Fisher T distribution, s' is the estimator of the variance of the residual distribution and n is the number of residuals.

Having established the precision for $\ln V_0$, it is interesting to evaluate the relative uncertainty in τ_i :

$$\frac{\sigma(\tau_i)}{\tau_i} = \frac{\sqrt{\sigma^2(\ln V_0) + \sigma^2(\ln V_i)}}{(\ln V_0 - \ln V_i)} \quad (4.5)$$

The uncertainty of $\ln V_0$ depends on the wavelength. At wavelengths where the optical depth is usually small (longer wavelengths), it is also less variable. Consequently, the Langley plot method for determining $\ln V_0$ is more precise and the uncertainty is reduced. At short wavelengths, especially at 300 nm, the Langley plot method is more difficult to apply and the uncertainty in $\ln V_0$ is large. However, at the shorter wavelengths, the large optical depth results

in a large difference ($\ln V_0 - \ln V_i$) that compensates for the large uncertainty in $\ln V_0$. Hence, the relative uncertainty of τ_i is of the same order at all wavelengths.

For each wavelength and each site, an upper limit was estimated for the relative τ_i uncertainty considering only the contribution from $\ln V_0$ uncertainty. For this purpose, the 95% confidence interval and the smallest measured difference ($\ln V_0 - \ln V_i$), *i.e.*, the worst case, was used. At Riverside, this estimation was on the order of 5% at 300 and 368 nm, and lower at all other wavelengths. At Mt Wilson, it was on the order of 2% at 300 and 368 nm, and lower at all other wavelengths.

Some uncertainty in τ_i is also due to uncertainty in the direct irradiance measurement. The dominant uncertainty in $\ln V_i$ is due to electronic noise that is on the order of 1 mV. In order to achieve a low relative uncertainty only direct irradiance measurements greater than 50 mV were used in this analysis. Sources of systematical uncertainties other than the bias due to differences in elevation profile of the atmospheric absorbing and scattering material are believed to be negligible (Schmid *et al.*, 1998).

4.1.2 Cloud influence

When studying optical depth variability, it is important to determine whether clouds are present or not. While in clear sky situations the total optical depth can vary due to absorbing gases and aerosols in the atmosphere, clouds produce such large and rapid optical depth variations that other effects frequently become negligible in comparison. Figure 4.2 shows the optical depth time series for July 16 and 17, 1997 at Riverside at wavelength 300, 318 and 368 nm. July 16 is a day when clouds were present, whereas skies were clear on July 17. On July 16, the optical depth increased by more than 2 at all wavelengths, in less than an hour, just after midday (Julian day time equal to 197.5). This reflects the localized nature of clouds. In some cases, when clouds are present but not in the direct beam path, the total irradiance may be higher than clear-sky irradiance because of increased diffuse light, while minutes later, the presence of a cloud in the beam path greatly reduces the total irradiance. On July 17, optical depth variations were much smaller and slower.

In many instances, photochemical air pollution is linked to stagnant high-pressure systems. Because our long-term goal is to improve the treatment of actinic flux for simulating photochemistry in air quality models, we chose to study the optical depth variability for clear-sky situations. During SCOS97, broadband solar irradiance was measured at Riverside and Mt Wilson with Eppley Precision Spectral Pyranometers (PSP). Data were recorded almost continuously during the 4-month measurement period with a frequency between 3 and 15 minutes. For clear sky conditions, broadband total solar irradiance depends linearly on the cosine

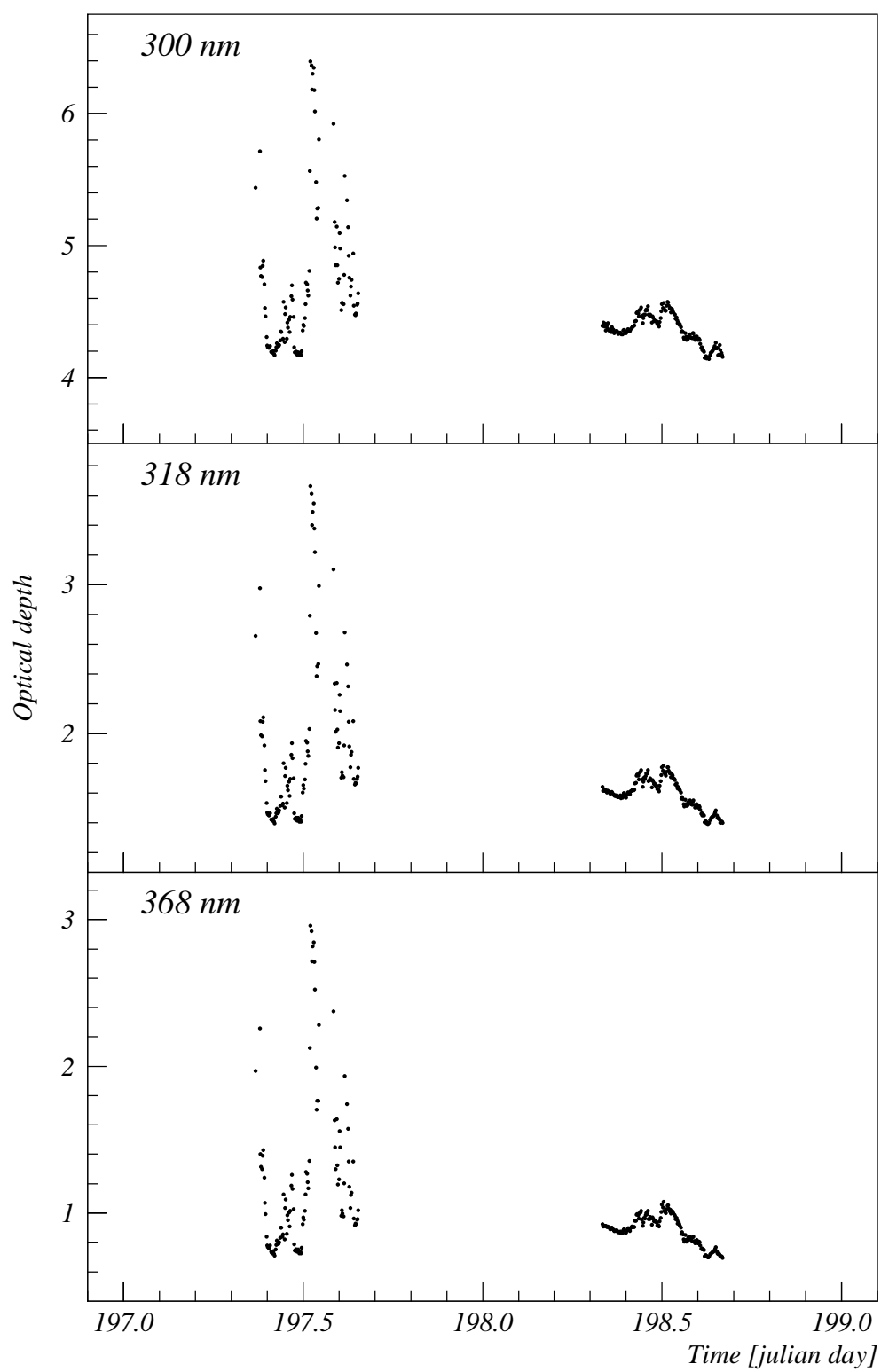


Figure 4.2: Optical depth time series for July 16 and 17, 1997 at Riverside at $\lambda = 300$, 318 and 368 nm.

of the solar zenith angle when the latter is below 70° . The broadband irradiance (PSP) data were used to establish the appropriate linear relationship, and the data points for which the irradiance differed by more than 100 W/m^2 from the established relationship were classified as cloudy periods. The Mt Wilson broadband irradiance data for zenith angle less than 70° are shown in Figure 4.3 with the $\pm 100 \text{ W/m}^2$ limits.

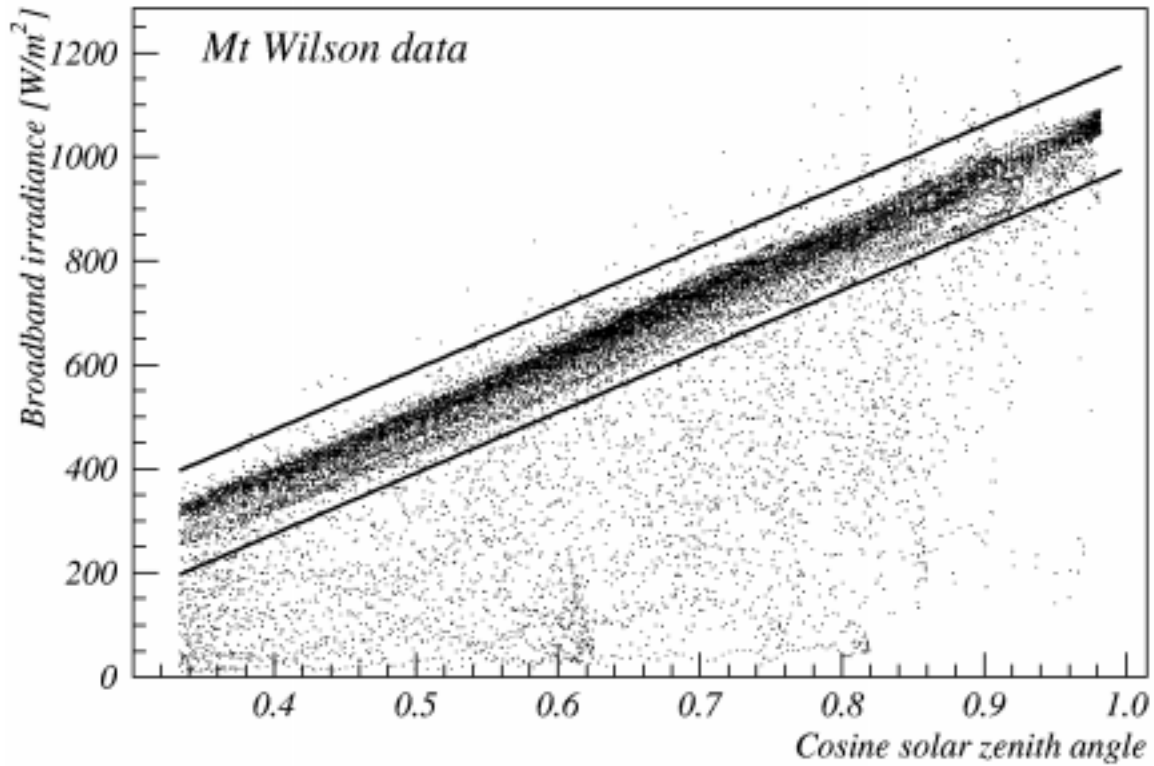


Figure 4.3: Broadband visible total solar irradiance vs. cosine solar zenith angle.

Clear-sky total optical depths were calculated after rejecting all measurements taken within 30 minutes (before or after) of cloudy periods. This criterion excludes data similar to those from Riverside on July 16, and retains data such as those recorded on July 17 (see Figure 4.2).

4.1.3 Distributions of optical depths

The original UV spectral irradiance data set includes 19,568 3-minute average measurements of the direct irradiance at each of the seven wavelengths at Riverside and 21,972 measurements at Mt Wilson. After selecting only time periods where the direct irradiance measurement was greater than 50 mV at all wavelengths and rejecting measurements taken at times when clouds were present, it was possible to compute 8,232 total optical depths for Riverside and 11,261 for

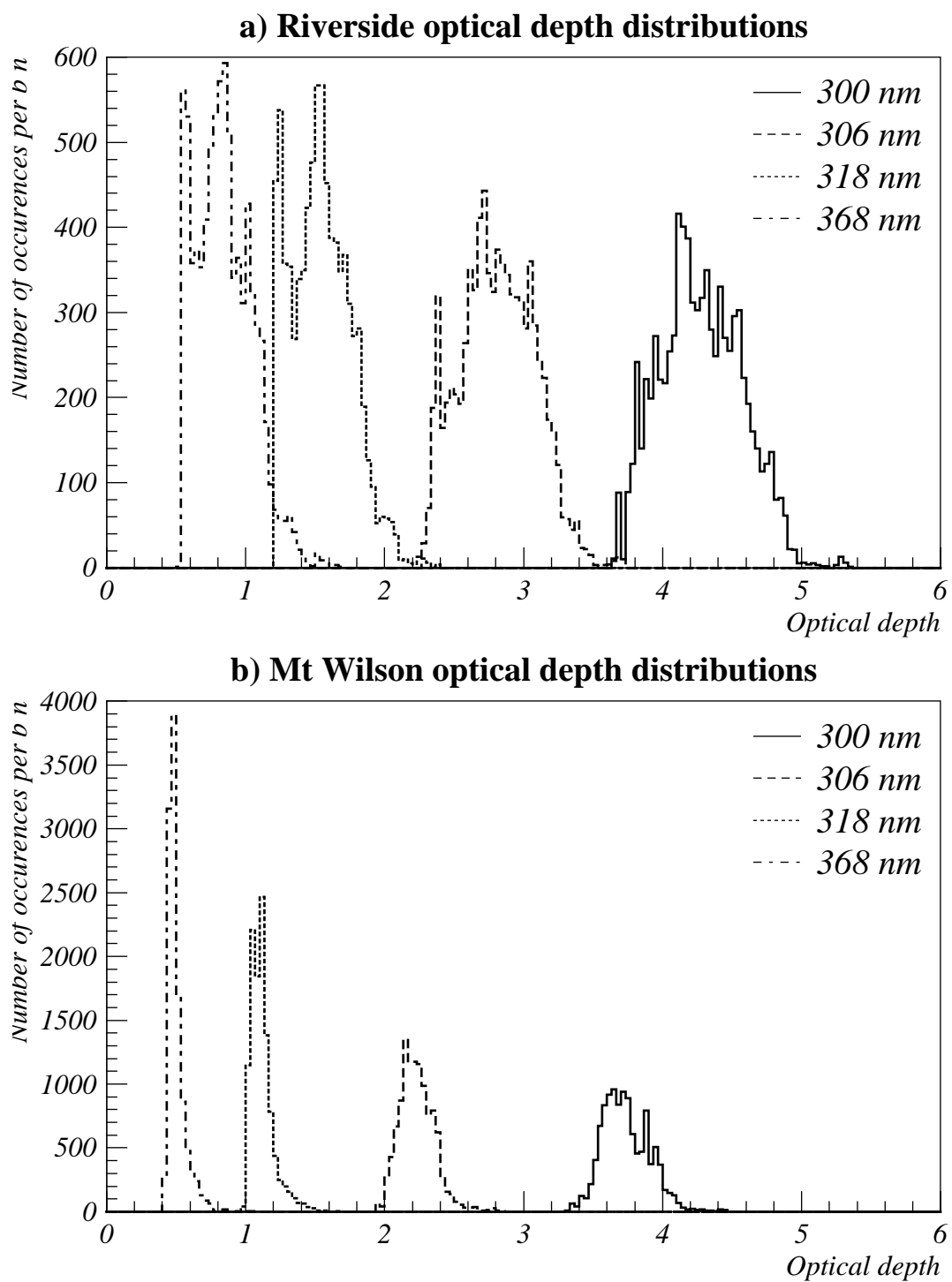


Figure 4.4: Optical depth distributions at $\lambda = 300, 306, 317$ and 368 nm.

Mt Wilson. As a consequence of the selection criteria, all measurements used in the analysis were made at times when the solar zenith angle was less than 60° , for both sites.

Distributions of optical depths were compiled for both Riverside and Mt Wilson for all wavelengths. Histograms of the distributions at both locations at four wavelengths are shown in Figure 4.4. A summary of the optical depth distribution characteristics is shown in Figure 4.5 where average values of the optical depth are plotted as a function of wavelength at both sites, and a bar is included to represent the standard deviation.

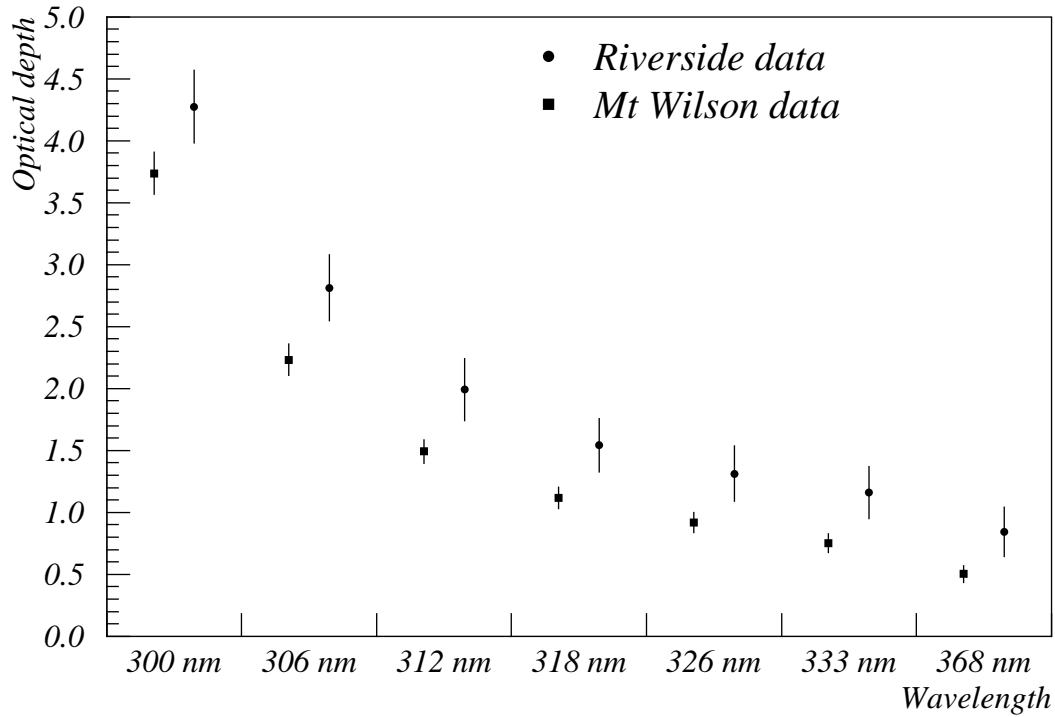


Figure 4.5: Averages and standard deviations of the optical depth distributions vs. wavelength.

The optical depths range from about 0.5 (Mt Wilson at $\lambda = 368$ nm) to about 4.3 (Riverside at $\lambda = 300$ nm). At Riverside, for each wavelength, the difference between the maximum and minimum optical depth is on the order of 1 or larger. This range illustrates the temporal variability in optical depths observed at a single site and wavelength. For a given time, direct beam irradiances for total optical depths τ_1 and τ_2 will differ by a factor $\exp((\tau_1 - \tau_2)m_e)$. This is more than a factor of 2 for an optical depth difference of 1 with overhead sun ($m_e = 1$ when the solar zenith angle is zero) and a factor larger than 7 for $m_e = 2$ (solar zenith angle of 60°). The diffuse irradiance will also be different but the factor must be calculated using a radiative transfer

model. The optical depths and the width of their distributions are smaller at Mt Wilson. In a pristine environment these differences would be expected to be the result of spatial and elevational differences. However, the increment in optical depth added by a purely Rayleigh scattering atmosphere accounting for the difference in elevation between Riverside (radiometer 260 m a.s.l.) and Mt Wilson (radiometer 1725 m a.s.l.) is smaller than the observed difference at all 7 wavelengths. A calculation following the formula given by Stephens (1994) yields an optical depth difference of 0.19 at 300 nm and 0.08 at 368 nm, while the observed average differences are 0.54 and 0.34, respectively. The remainder of the difference between the averages in Riverside and Mt Wilson is due to the more polluted air in Riverside that results in greater light absorption and scattering by pollutants. Similarly, the larger variability in Riverside is due to the larger pollution concentration changes observed at Riverside compared to Mt Wilson.

The optical depth decreases as wavelength increases, for the range of wavelengths considered here. The same trend is observed at both Riverside and Mt Wilson. A large decrease in optical depth is observed between 300 nm and 306 nm, and between 306 nm and 312 nm. At longer wavelengths, the rate at which optical depth decreases with increasing wavelength is lower. At the wavelengths of our measurements, the optical depths are largely due to absorption and/or scattering by ozone and aerosols because:

- 1) Ozone is an influential light-absorbing gas at wavelengths shorter than 330 nm, and its absorption cross-section exhibits a sharp drop above 300 nm (Seinfeld and Pandis, 1997, pp. 143–146).
- 2) Aerosols in the atmosphere are known to have broad absorption and scattering cross-sections at UV wavelengths, due to the particle size distribution and variability in chemical composition (Seinfeld and Pandis, 1997, pp. 1126–1146).

Analysis of atmospheric composition and visibility in Los Angeles on relatively clean and smoggy days (Larson *et al.*, 1984) has shown that large values of the extinction coefficient (b_{ext}) are mainly due to large amounts of aerosol with diameter ranging from 200 to 500 nm. For UV wavelengths in the same range, the optical depth is expected to vary approximately as $\lambda^{-\nu+2}$ with ν between 2 and 4 (Shaw, Reagan and Herman, 1973).

4.2 Statistical Analysis

4.2.1 Methodology

Our analysis of the optical depth distributions is based on the hypothesis that absorption and scattering by ozone and aerosols are responsible for most of the observed variability. Principal component analysis is a tool of choice to examine this hypothesis and *quantify* the apportionment

of the variability among the different factors. PCA is a statistical tool that has been used extensively in environmental sciences. Examples of its use are the apportionment of pollutants to possible sources (e.g., Henry, 1979, 1982; Baldasano, 1998), and solving inverse problems such as determining the characteristics of light-absorbing and scattering pollutants given the absorption spectrum (Steele and Turco, 1997). PCA is a technique for analyzing the variability of a group of simultaneously measured variables using their correlations (Everitt and Dunn, 1992). The goal of PCA is to uncover the underlying independent factors responsible for the variability observed in the group of variables, and to determine the most influential factors. To achieve this goal, the covariance matrix is diagonalized and expressed as:

$$\mathbf{C} = \mathbf{Z} \cdot \mathbf{D} \cdot \mathbf{Z}^{-1}, \quad (4.6)$$

where \mathbf{C} is the covariance matrix, \mathbf{D} is the diagonalized form, and \mathbf{Z} is the matrix of a rotation operator that transforms the n -dimensional space defined by the variables of interest (n is the number of variables) into a space where the covariance matrix is diagonal. The elements of the diagonal matrix \mathbf{D} are the eigenvalues of \mathbf{C} , and the matrix \mathbf{Z} is formed from the eigenvectors of \mathbf{C} (the i -th column of \mathbf{Z} is the eigenvector associated with the i -th eigenvalue in \mathbf{D}).

When applying PCA to our data, every simultaneous measurement of the optical depths at the seven wavelengths is considered as a point in the 7-dimensional space. The coordinates of such points are the optical depths measured at each of the wavelengths. The unitary matrix \mathbf{Z} transforms the reference frame of the 7-dimensional space. The components, *i.e.* the coordinate of each measurement point expressed in the new reference frame, are independent of each other (because the correlation matrix is diagonal in the new reference frame). The first component is chosen so that the largest possible part of the variability occurs along it, the second component so that the largest possible part of the remaining variability occurs along it, etc. It is useful to use a geometrical analogy to understand this approach. Let us assume optical depths are given at only 3 wavelengths, and the points representing the measurements are distributed in an ellipsoid-shaped cluster as shown in Figure 4.6. The PCA approach is equivalent to finding a rotation that will align the first component with the longest axis of the ellipsoid (a), the second component with the second longest axis (b), etc. The elements of the diagonal matrix \mathbf{D} , the eigenvalues of the correlation matrix, are used to determine the relative amount of variability associated with each component. The components define a new reference frame where the covariance matrix is diagonal. Hence, the components are uncorrelated. Determining the alignment of the components in the original reference frame helps identify the components. For this study, when a component makes a very small angle with one axis of the original frame, the underlying factor associated with the component absorbs and/or scatters at the wavelength associated with the axis,

but not at the other wavelengths considered. When the angles between one component and all axes are similar, the underlying factor affects all wavelengths similarly.

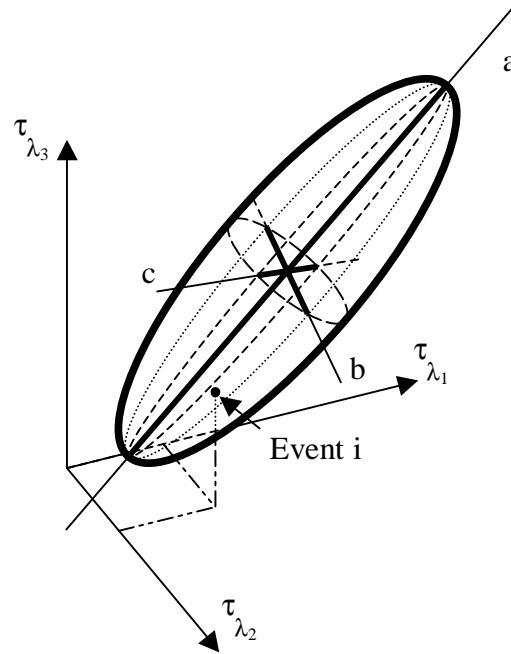


Figure 4.6: Geometrical analogy for Principal Component Analysis.

4.2.2 Results

Figures 4.7 and 4.8 show the optical depths for Riverside and Mt Wilson, respectively. The measurements at $\lambda = 300, 306$ and 312 nm are plotted against the measurements at $\lambda = 318$ and 326 nm. The correlation coefficients are included in the figures. Correlations are given instead of covariance because they are normalized, whereas covariance can have arbitrarily high values, depending on the variances of the two variables of interest. Similar correlation coefficients were computed for optical depths at all pairs of wavelengths and are given in Table 4.1.

At Riverside, the main characteristic is the strength of the correlation between measurements at all wavelengths. The weakest correlation coefficient is 0.92. Not surprisingly, correlation tends to be stronger for neighboring wavelengths (close to the diagonal) than for wavelengths that are further apart (away from the diagonal). Exceptions are the correlations between measurements at $\lambda = 318$ nm and smaller wavelengths (3rd column of the correlation matrix in Table 4.1) that are weaker than correlations between measurements at 326 nm and smaller wavelengths (4th column). A possible explanation is that the channel at 318 nm may have had greater measurement noise than the other channels.

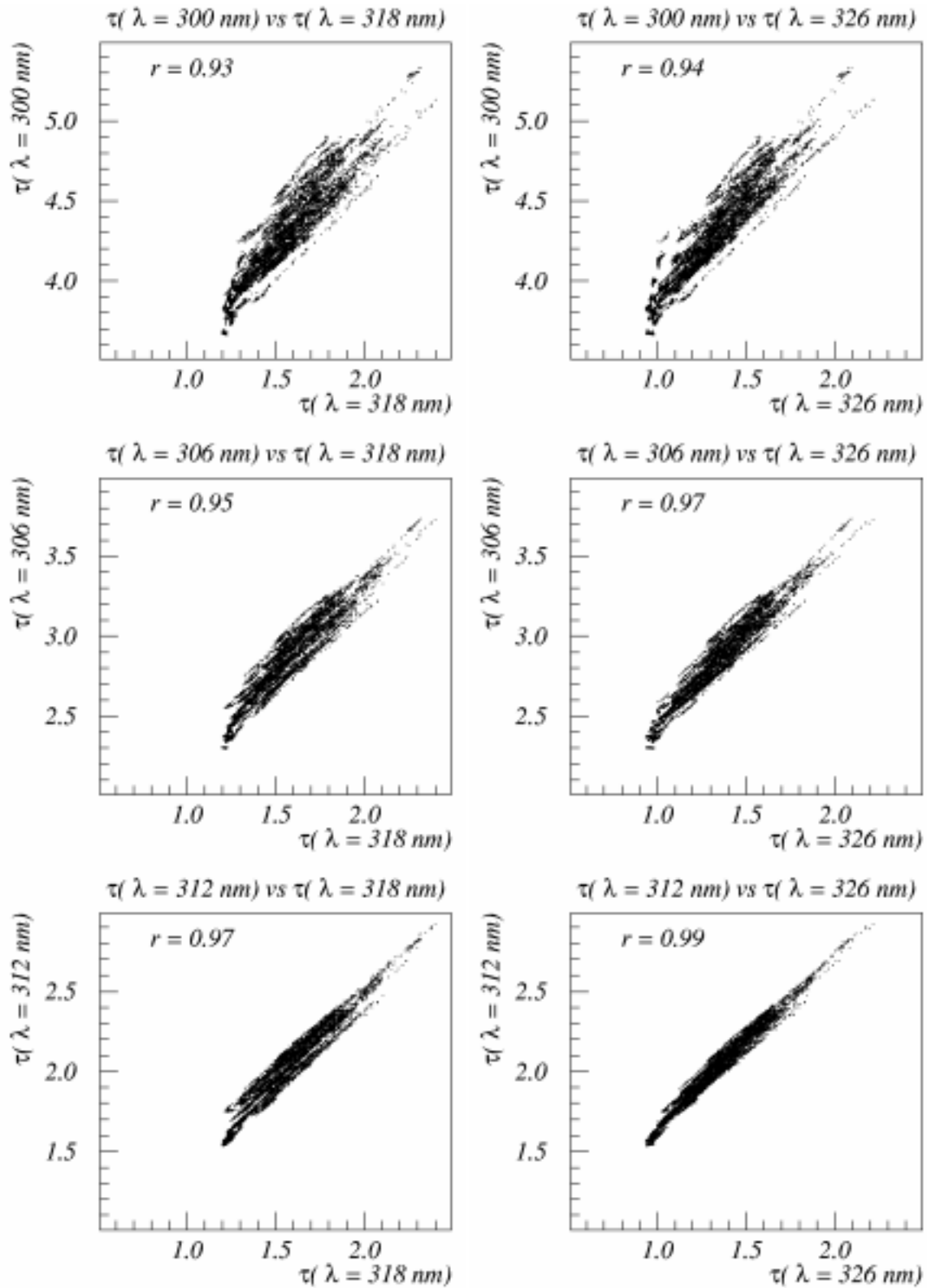


Figure 4.7: Optical depth correlations at Riverside (optical depths at 300, 306 and 312 nm vs. optical depths at 318 and 326 nm).

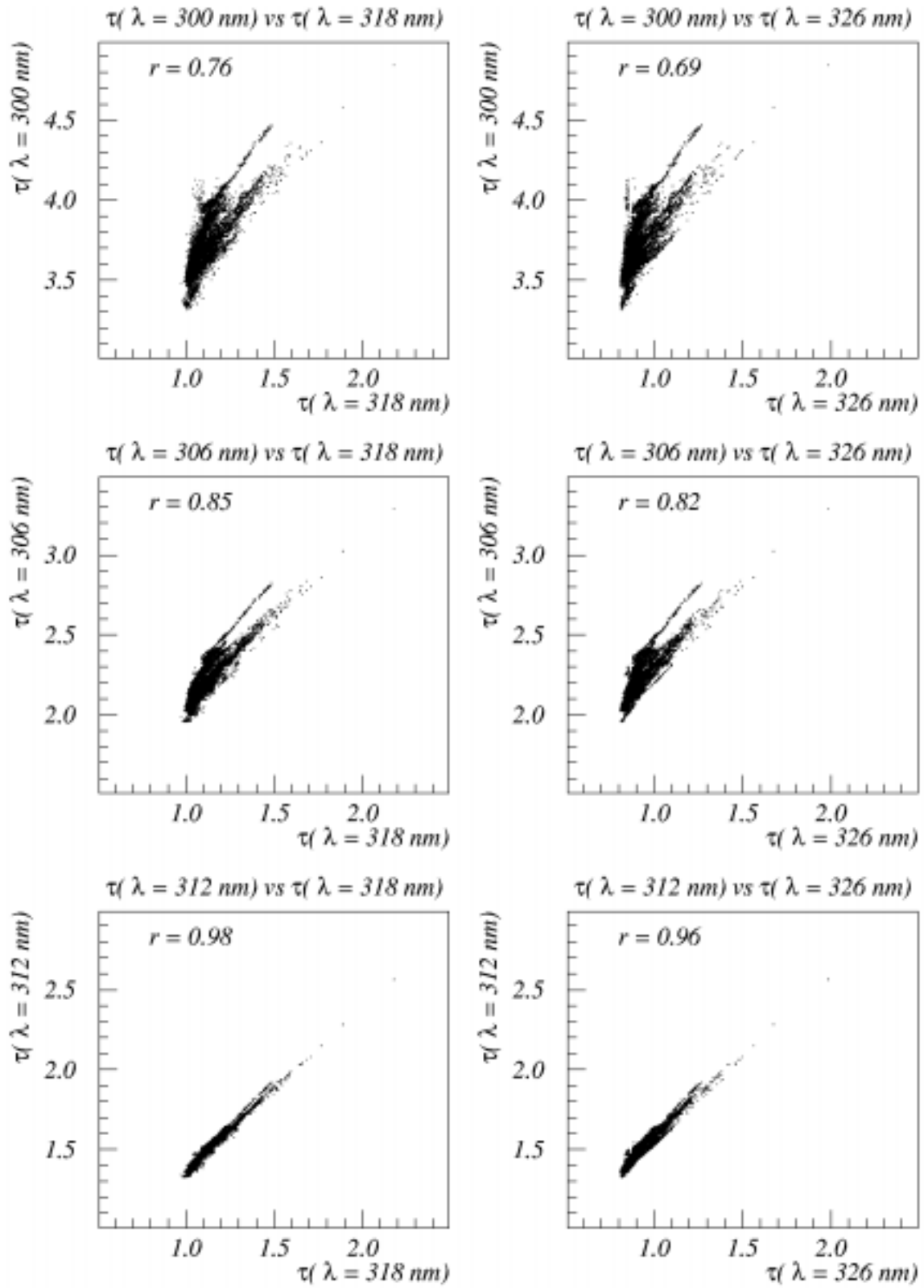


Figure 4.8: Optical depth correlations at Mt Wilson (optical depths at 300, 306 and 312 nm vs. optical depths at 318 and 326 nm).

Riverside	306 nm	312 nm	318 nm	326 nm	333 nm	368 nm
300 nm	0.99	0.97	0.93	0.94	0.92	0.92
306 nm		0.99	0.95	0.97	0.95	0.95
312 nm			0.97	0.99	0.97	0.97
318 nm				0.99	1.00	0.99
326 nm					1.00	0.99
333 nm						1.00
Mt Wilson	306 nm	312 nm	318 nm	326 nm	333 nm	368 nm
300 nm	0.94	0.85	0.76	0.69	0.62	0.59
306 nm		0.92	0.85	0.82	0.77	0.74
312 nm			0.98	0.96	0.93	0.91
318 nm				0.98	0.96	0.95
326 nm					0.99	0.98
333 nm						1.00

Table 4.1: Correlations between optical depth measurements at various wavelengths

At Mt Wilson, the same overall characteristics of strong correlation with weaker correlation away from the diagonal are observed. However, correlation coefficients are smaller than for Riverside and an additional feature can be distinguished. The correlation between measurements at 300 and 306 nm is strong (0.94), as well as the correlation between measurements at wavelengths longer than 310 nm (four bottom rows of the correlation matrix in Table 4.1). However, the correlation between measurements at 300 or 306 nm, and measurements at longer wavelengths is weaker. For instance, the correlation between measurements at 300 and 312 nm (0.85) is weaker than the correlation between 312 and 368 nm. This is due to the influence of both aerosols and ozone at 300 and 306 nm, while only aerosols have an influence at longer wavelengths. Similarly, the stronger correlations observed at Riverside than at Mt Wilson is due to a larger influence of aerosols on the optical depths at Riverside (frequent pollution episodes occur at this site).

The eigenvalues of the correlation matrices for Riverside and Mt Wilson are shown in Figure 4.9. At Riverside, 97% of the variability is associated with the first component and 2% with the second. At Mt Wilson, the variability associated with the first and second components is 89% and 10%, respectively. While all the components are necessary to explain all the observed

variability, a smaller number is sufficient to provide an adequate summary. Rules of thumb to choose the number of components to retain are (Everitt and Dunn, 1992):

- 1) Include just enough components to explain a relatively large percentage of the total variation (e.g., 90%).
- 2) Exclude components that have eigenvalues less than a given cut-off value (0.7 has been suggested by Jolliffe (1972)).
- 3) On a plot of eigenvalues (Figure 4.9), locate the point where an “elbow” is present and discard the components after this point.

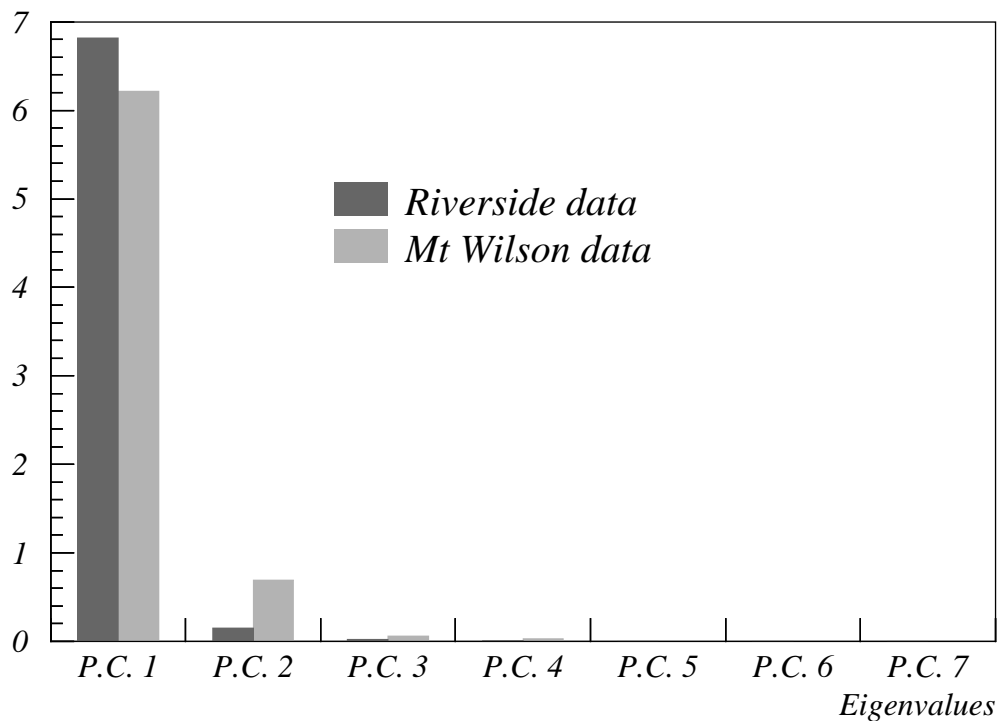


Figure 4.9: Eigenvalues of the correlation matrices for Riverside and Mt Wilson.

These rules of thumb suggest selecting only the first component in Riverside, and the two first components at Mt Wilson. For consistency, the two first components are analyzed both for Riverside and Mt Wilson. The matrix \mathbf{Z} can be used to determine the contributions of the optical depths at various wavelengths to the components or, in other words, the angles between the components and the axis of the original reference frame. Figures 4.10 a) and b) indicate the contributions of the various wavelengths to the first and second principal components. Since correlations are used, values are normalized, and the maximum possible contribution is 1. The contributions of all wavelengths to the first component are almost equal, especially for Riverside.

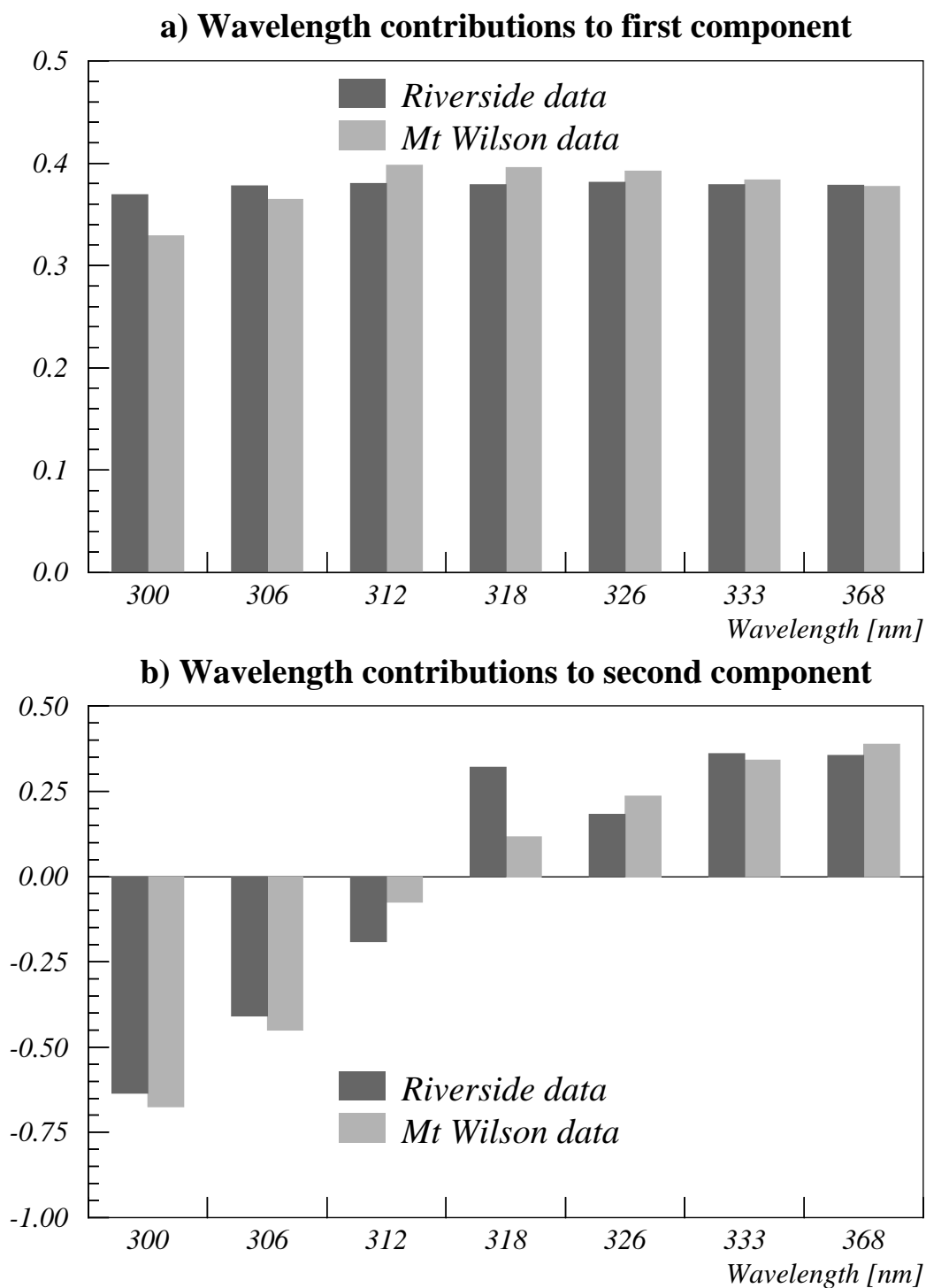


Figure 4.10: Wavelength-dependent optical depth contributions to first and second principal components.

Therefore, if the value of the factor responsible for the first component varies, all optical depths will vary in a similar way. The structure of the second principal component reflects the fact that correlation tends to be stronger for neighboring wavelengths than for wavelengths that are further apart. More attention should be devoted to the second component contributions at Mt Wilson than Riverside, since the second component accounts for only 2% of the variability at Riverside. At Mt Wilson, the largest contribution in absolute value is at $\lambda = 300$ nm, and the contribution at $\lambda = 306$ nm is also strong. At 312, 318 and 326 nm the contributions are weak while they are on the order of 0.35 at 333 and 368 nm. If contributions would all be strictly equal, they would be equal to $\sqrt{1/7}$ or 0.38. When a contribution is below this limit in absolute value, the corresponding component has little influence at the corresponding wavelength. When it is above, the component has a strong influence at this wavelength. Since the contribution is significantly stronger at 300 nm, the second component has its strongest influence at this wavelength. At Riverside a similar behavior is observed, although the anomaly pointed out for the correlations at 318 nm shows up in the second component.

Given *a priori* knowledge about the absorbing properties of ozone and aerosols in the atmosphere, the interpretation of the principal component analysis is relatively straightforward. The first component, explaining most of the data variability, and corresponding to simultaneous increases or decreases of the optical depth at all observed wavelengths, is linked to the presence of aerosols that absorb and scatter light over the full range of wavelengths measured. The second component that distinguishes between the shorter and longer wavelengths and has a stronger association with the absorption at $\lambda = 300$ nm is linked to ozone whose absorption spectrum declines sharply at wavelengths longer than 300 nm. “Contamination” of the components might occur, giving rise to measurement error contributions to the first or second component, or ozone contributions to the first component and aerosol contributions to the second. However, the remarkable similarity between the component signatures (the contribution to the components) at Riverside and Mt Wilson is an indication of the quality of the PCA discrimination. The only question mark is the 318-nm contribution to the second component at Riverside, but this component at Riverside is almost negligible.

At the observed wavelengths, principal component analysis suggests that almost all the optical depth variability is due to changes in aerosol concentration at both sites. At Riverside, the influence of aerosol variability is strong enough that the variability due to changes in ozone column is negligible even at the shorter wavelengths. At Mt Wilson where the environment is more pristine, the optical depth variability is lower and the influence of changes in the ozone column is more influential, proportionally. When the aerosol and ozone variability are taken into account, the remaining unexplained variability is negligible (on the order of 1% or below).

Despite differences in component size at Riverside and Mt Wilson, the similarity of the principal component structure is remarkable. Similar physics are expected to be the cause of the variability in optical depths at Riverside and Mt Wilson; otherwise, there would be no reason for the wavelength-dependent optical depth contributions to the principal components to be similar at the two sites. This study shows that the most influential factors for the optical depth variability are the same (light absorption and scattering by aerosols as the major factor, and absorption by ozone as the minor factor), and are ordered in a similar fashion at the two sites. The study also quantifies the influence of each factor and indicates the differences in relative influence of aerosols and ozone on the variability associated with optical depth at Riverside and Mt Wilson.

It should be emphasized that this chapter focused on the variability associated with optical depth. Even though aerosol optical depth was found to be the most influential factor in the optical depth variability at all the wavelengths considered in this study, this does not imply that it is the most important contribution to the total optical depth. For example, it is possible that the variability in ozone optical depth occurs around a larger stable average value than for the aerosol. PCA would not extract the signal due to the stable average.

5 Radiative Transfer Model Input Parameters

5.1 Aerosol optical properties and ozone column

The sensitivity analysis discussed previously in Chapter 3 highlighted the importance of aerosol optical properties and the total ozone column in radiative transfer calculations. Values for these parameters are needed by the radiative transfer model to compute actinic fluxes and photodissociation rates (*i.e.*, J values). As discussed earlier (section 2.3 and section 3), three main aerosol parameters are needed: the aerosol optical depth (τ_{aer}), the single scattering albedo (ω_0), and the aerosol asymmetry factor (g). Additionally, the radiative transfer model defines the dependence of aerosol optical depth on wavelength (it is assumed that $\tau_{\text{aer}} \propto 1/\lambda$), and a vertical distribution of aerosols that places most of the aerosol near the earth's surface.

Total optical depths (τ) were computed from UV multifilter radiometer data at Riverside and Mt. Wilson, as described elsewhere in this report (see section 4.1). By subtracting the contribution due to Rayleigh scattering (τ_{R}) from the total optical depth, estimates of aerosol optical depth at $\lambda=333$ nm were obtained (note that ozone does not absorb at this wavelength). The cumulative frequency distributions of $\tau - \tau_{\text{R}}$ are shown in Figure 5.1 for both sites. Median summer 1997 values for τ_{aer} were 0.09 at Mt. Wilson and 0.39 at Riverside. The value at Riverside is nearly identical to the default value of 0.38 specified in the radiative transfer model at $\lambda=340$ nm. It should be noted in Figure 5.1, however, that considerable variability in this parameter can occur; 80% of the aerosol optical depths determined for Riverside in summer 1997 fell within a range extending from 0.12 to 0.68. Improved procedures for objectively screening optical depth measurements for the presence of clouds are needed; some of the haziest periods may have been removed from our clear-sky data set even though no clouds were present. Therefore the 90th percentile of aerosol optical depth at Riverside may in fact be larger than suggested above. Also note that τ_{aer} may have been higher in earlier years when particulate matter concentrations were higher.

Expert judgement at present is that the value of single scattering albedo at ultraviolet wavelengths is highly uncertain, with appropriate values likely to fall somewhere in the range 0.75–0.95 for urban areas (Madronich, 2000). In the present model applications to California we set $\omega_0 = 0.85$, in the middle of this range. Further research, for example using paired optical depth measurements from Riverside and Mt. Wilson from SCOS97, is needed to reduce the uncertainty in this parameter. Mie theory calculations that use measured aerosol size distributions and chemical composition are not able at present to provide appropriate values of ω_0 , because of concerns about unquantified light absorption by particulate organic carbon (e.g., aromatic rings

are known to absorb in the UV). The default value of the aerosol asymmetry factor ($g = 0.61$) specified in the radiative transfer model was used in this study.

Total ozone column has been monitored worldwide on a daily basis since 1971, using the Total Ozone Mapping Spectrometer (TOMS), a satellite-borne instrument. Global maps of total ozone column (NASA, 2000) for August 27–29, 1987 and August 4–6, 1990 indicate that a value of 300 Dobson Units (DU) is appropriate for these two summertime air pollution episodes in California, with an uncertainty of ± 25 DU.

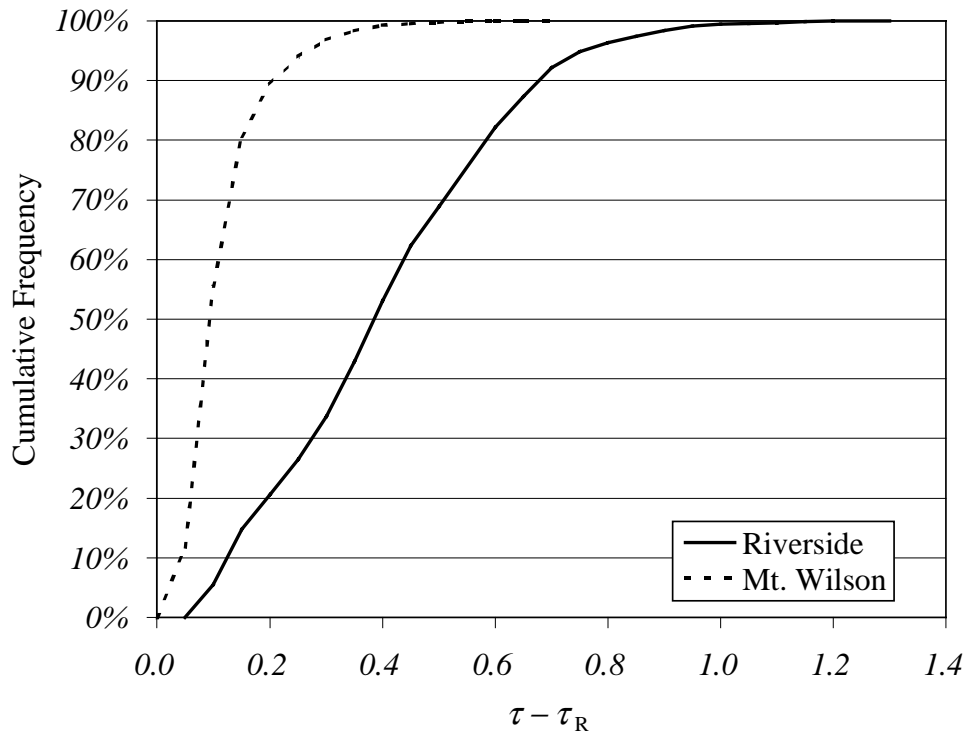


Figure 5.1: Cumulative frequency distributions of optical depths⁵ ($\tau - \tau_R$) at $\lambda=333$ nm for two southern California monitoring sites⁶ from summer 1997.

5.2 Review of Routine Radiation Data

Direct measurement of aerosol optical properties as described in the previous section is the most desirable way to specify parameters needed in radiative transfer modeling. However, this type of data is rarely available with good spatial and temporal resolution. We reviewed routinely available monitoring data in California and found that ground-based measurements of total solar,

⁵ $\tau - \tau_R$ excludes contribution due to Rayleigh scattering.

⁶ Mt. Wilson (elev. 1725 m) is above much of the urban haze layer, so optical depths there are lower.

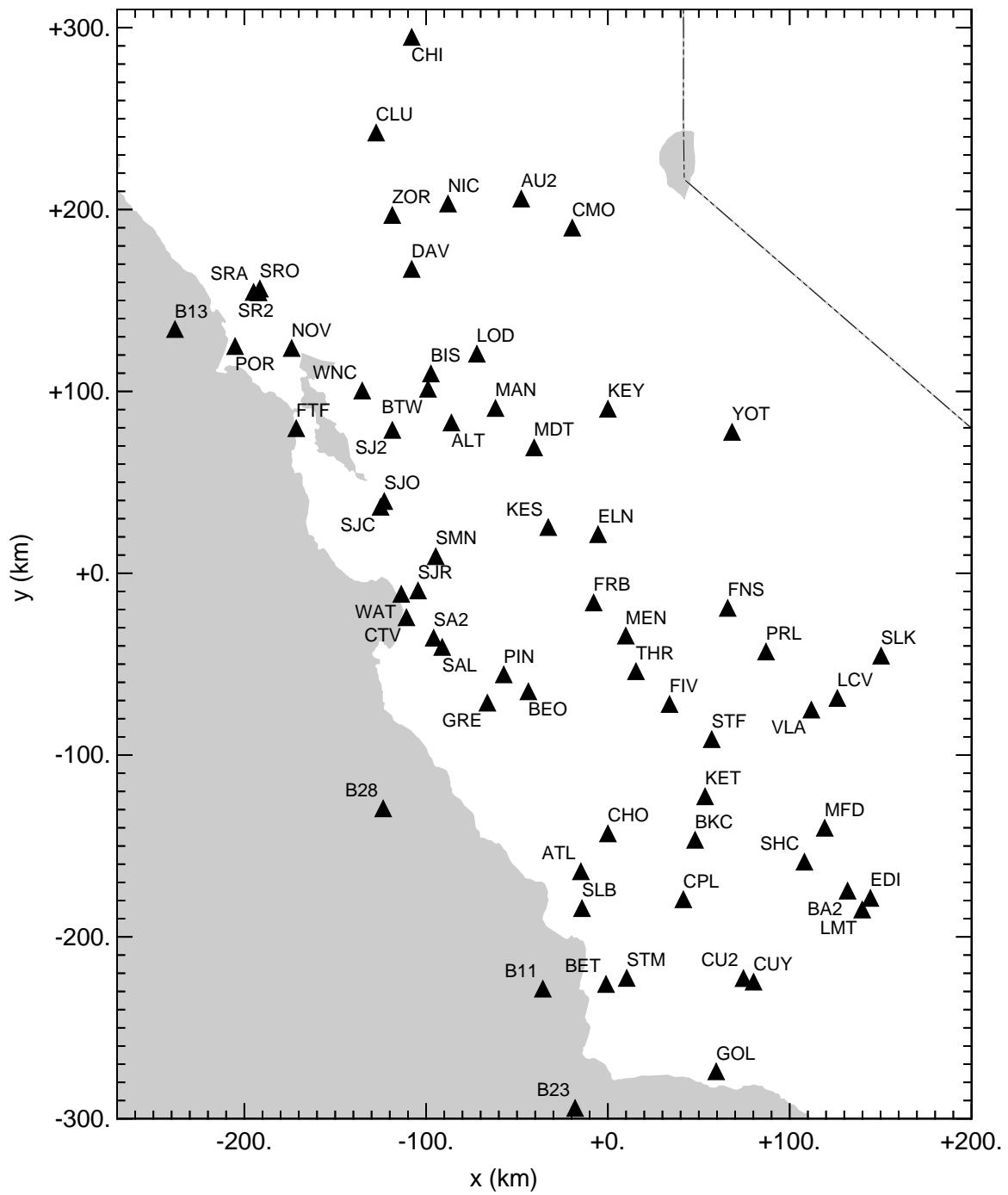


Figure 5.2: Radiation monitoring sites in the San Joaquin Valley.

but not broadband UV, radiation are widely available, as shown in Figure 5.2 for the 1990 San Joaquin Valley Air Quality Study. Sixty-seven monitoring sites stretching from Santa Rosa to Santa Barbara are included. Twenty-two of these sites measured only incoming total solar radiation; 37 measured both total and net (incoming-outgoing) solar insolation; 2 measured total and UV radiation; and at 1 site UV radiation intensity only was measured.

Although UV irradiance measurements are more directly relevant to calculating photolysis rates, total solar irradiance measurements are much more available. The correlation between UV and total solar irradiance was therefore examined, as shown in Figure 5.3 for the Three Rocks site (THR in Figure 5.2, near Fresno) and in Figure 5.4 for Riverside from SCOS97 data. Both Figures shown a non-linear relationship between total and UV irradiance, with the UV irradiance attenuated more strongly than total solar irradiance as the sun drops lower in the sky. The equations of fit relating UV and total irradiance are similar at both sites.

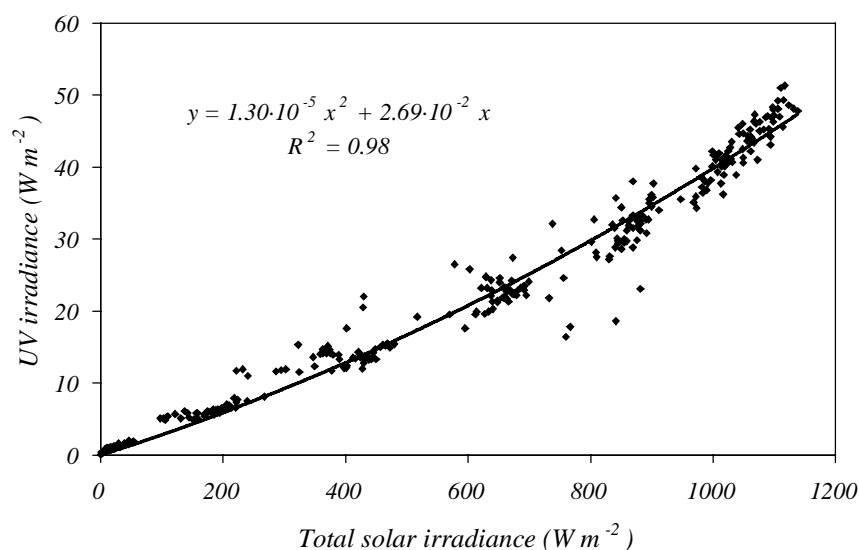


Figure 5.3: Correlation between total solar and UV irradiance at Three Rocks.

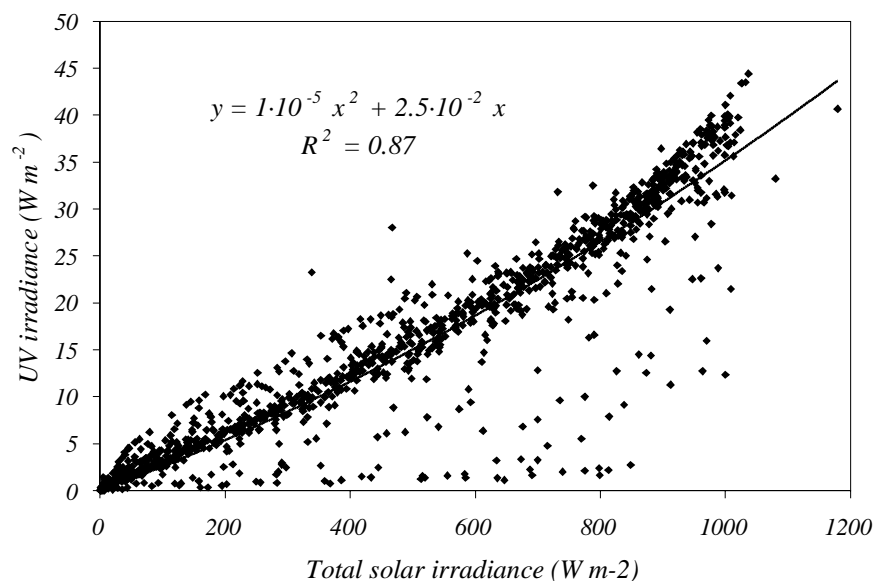


Figure 5.4: Correlation between total solar and UV irradiance at Riverside.

5.3 Ground albedo

Ground surface albedo data were obtained for the Los Angeles Area (Taha, 1998). While the full range of possible ground albedo is 0 to 1 (0=no reflection at the earth's surface, 1=100% reflection), in fact only a limited range of values from 0.07 to 0.20 is relevant for southern California (see Figures 5.5 and 5.6). Figure 5.5 shows the distribution (number of 5 km by 5 km

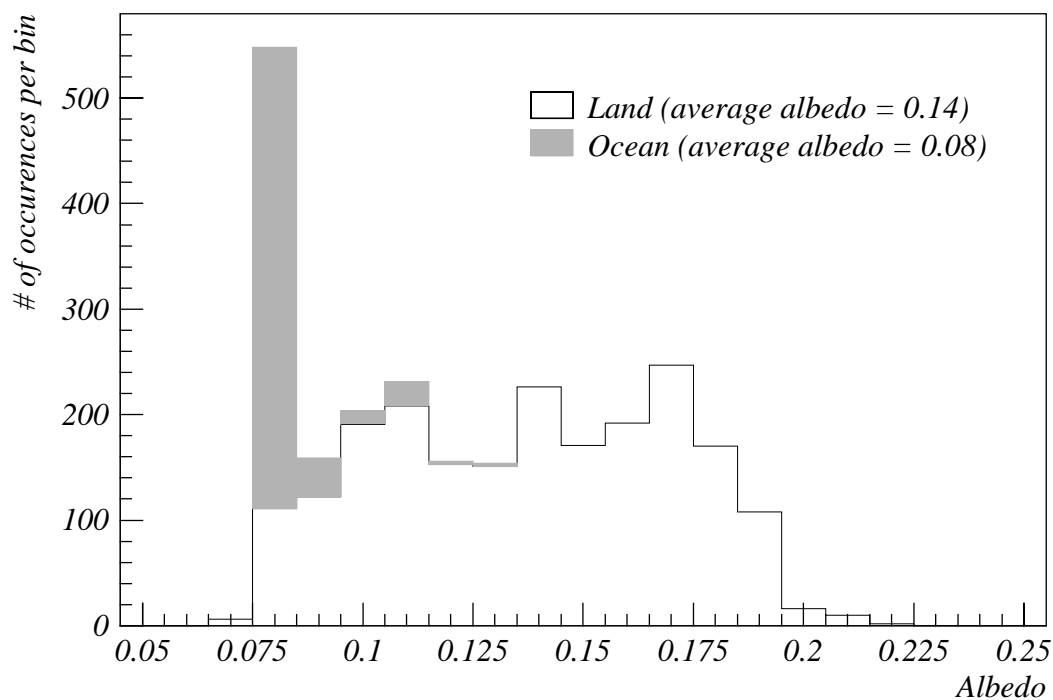


Figure 5.5: Los Angeles Area ground albedo distribution.

grid cells) of ground albedo in southern California and Figure 5.6 is a map of the surface albedo. The ocean has low albedo except when the sun is near the horizon. The most reflective surfaces are urbanized areas and desert. The forested areas in the San Gabriel, San Bernardino, Santa Ana, and San Jacinto mountains have low albedo (see Figure 5.6).

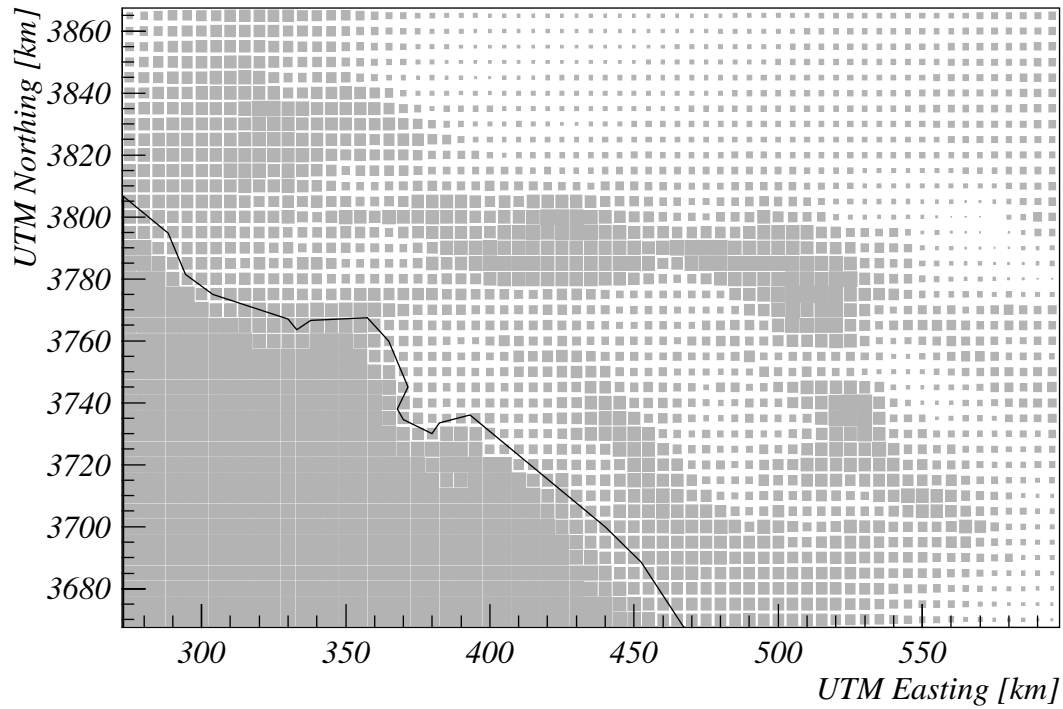


Figure 5.6: Los Angeles Area ground albedo map (5×5 km grid). The size of the squares is inversely proportional to the albedo (smallest squares correspond to 0.22, and largest to 0.07) so that the lower albedo regions appear darker, and the higher albedo regions appear lighter.

6 Radiative Transfer and Photolysis Module Implementation

The Tropospheric Ultraviolet-Visible radiation transfer model (TUV) has been selected for our treatment of radiative transfer in Air Quality Models (AQM) (see section 2.6). In the original version (version 3.9, February 97), TUV is a standalone radiation transfer model. Consequently, the execution follows a linear flow: First, the input parameters are initialized for fixed conditions suitable for a given location and date. Second, the radiation transfer equation is solved for given times of the day at all the pre-defined altitudes. Changing the input parameter values requires changes both in the input data files and in the code itself. While this approach is well suited for using TUV as a standalone radiation transfer model, it results in unacceptable limitations if TUV is to be used within an AQM. Within an AQM, a range of conditions can occur depending on the modeling domain cell (location) and modeling time. Some parameters may remain constant throughout the whole domain and modeling episode, and others may vary from cell-to-cell and time-to-time. For using TUV within an AQM, we made the following modifications:

- 1) We transformed TUV into a package (TUVAQM, see Volume II) including library routines, test programs, UNIX installing scripts, and supporting data. This enhanced the modularity of TUV, and allowed breaking the original linear flow into a set of separate steps.
- 2) We grouped all parameter initializations in a separate step that can be called independently from the radiative transfer calculations. It is possible to give all parameter initial values in a limited number of data files with a simple and flexible syntax.
- 3) We created a main routine, which is the only routine that needs to be called from the AQM. Depending on the value of the code variables when the main routine is called, it can initialize the input parameter values, update the parameter values, or perform a radiation transfer calculation and return the photolysis rate coefficients.
- 4) We changed the independent variable from time to zenith angle. (Most AQMs provide their own computation of the solar zenith angle.)

Ideally, all parameters that vary spatially or temporally should have their values updated for each AQM modeling cell (location) and time. Unfortunately, data that can be used to specify these parameters are usually scarce, and the spatial and temporal resolution is often poor. The strategy chosen in the current implementation is to select a reduced number of important parameters that can vary within the AQM simulation domain and episode. These parameters are:

- 1) zenith angle,
- 2) elevation grid,

- 3) ground albedo,
- 4) total ozone column,
- 5) total aerosol optical depth,
- 6) aerosol single scattering albedo, and
- 7) aerosol asymmetry factor.

The user *must* specify the temporal and spatial dependence for these parameters. First, the user must divide the modeling domain into regions and the modeling episode into time intervals such that the atmospheric properties can be considered as constant within a given region and time interval. Then the user needs to specify the parameter values for each region and time interval using an input file read at initialization.

For each region and time interval, a set of complete radiation transfer calculations is performed for conditions representative of the region and time interval. For all AQM cells within a region, and time steps within an interval, the photolysis reaction rate coefficients are computed by interpolation from the full radiation transfer calculations.

Every time a new region and/or time interval is encountered during the AQM simulation, a series of radiative transfer simulations is performed. Each of these simulations computes the photolysis reactions rate coefficients (J values) using the parameters listed above predefined for the region and time interval of interest in a multi-cell vertical column. The simulations differ in the ground elevation used (the base of the vertical column). For each region a set of representative ground elevations determines the elevation grids used in the simulations. Subsequent computations of the actinic flux in the same region and during the same time interval are evaluated by interpolation using values from the series of radiative transfer simulations performed when the region and time interval was encountered for the first time.

Three types of interpolation are used successively. First, an interpolation is used to obtain J values for the particular ground elevation under consideration from the J value calculations performed for different ground elevations relevant to the region of interest. Second, J values for the solar zenith angle under consideration are determined by interpolation from J value calculations using the solar zenith angles pre-determined for the region and the time interval of interest. Third, the J values in the vertical elevation cells considered in the radiation transfer model are projected onto the current AQM elevation grid structure. The interpolation scheme uses a three-point second-order polynomial algorithm in order to avoid derivative discontinuities.

7 Implementation of TUVAQM in Three Air Quality Models

TUVAQM has been implemented in three AQMs: the Urban Airshed Model version 6.21 (UAM621), the Flexible Chemical Mechanism version of UAM621 (UAM-FCM), and the SARMAP Air Quality Model (SAQM-SLS). The objective of this effort is to demonstrate the use of the treatment of photolysis rates developed in this study in actual simulations of ozone episode events. UAM621 and UAM-FCM are applied to the simulation of the August 26-28, 1987 ozone episode in the South Coast Air Basin (SoCAB). This episode occurred during the conduct of the Southern California Air Quality Study (SCAQS). SAQM-SLS is applied to a large portion of central California to simulate an ozone episode that occurred during August 3-6, 1990, as part of the San Joaquin Valley Air Quality Study/Atmospheric Utilities Signatures: Predictions and Experiments (SJV/AUSPEX) field monitoring program.

The source codes for UAM621, UAM-FCM, and SAQM-SLS were obtained from the California Air Resources Board (CARB). Each model uses the Carbon-Bond IV chemical mechanism. CARB also provided a complete set of input files as well as the associated output files for each model. We installed the codes and replicated the simulation results for each model. Then we modified the source code for each model to incorporate TUVAQM. A second simulation was carried out for each model, this time using J values derived from TUVAQM. The two sets of results from each model were examined to determine what influence the revised treatment of photolysis rates had on calculated ozone levels.

7.1 AQM code and input modifications

Incorporation of TUVAQM in each AQM involved the development of an interface subroutine to pass required data to TUVAQM during the course of a simulation. This interface also provides the mechanism for transferring the J values calculated in TUVAQM to the appropriate array in the AQM. Calls to the interface routine are made at appropriate points in the model set up and numerical integration processes. Additional parameters are included in the AQM input structure, as needed, to assure that all control and input data needed by TUVAQM are available. For example, an input parameter is included in each AQM to allow the user to select whether to employ the original photolysis treatment or that provided by TUVAQM. Provisions are included in each model to input gridded terrain heights, if needed, and subregion identifiers (used by TUVAQM to determine local values of spatially varying inputs, including the total aerosol optical depth, ground surface albedo, and aerosol asymmetry factor). Suitable means for opening required files are included in each AQM at an appropriate point in the model set up

sequence. Additional information to supplement the existing users guide for each model is included in Appendix A of Volume II of this report.

The current implementation of TUVAQM provides estimates of J values for photolysis reactions included in the SAPRC '97 chemical mechanism. Table 2.1 summarizes the photolysis reactions included in both the SAPRC'97 and Carbon-Bond IV (CB-IV) mechanisms. Where there is a one-to-one correspondence in reactions, the J values are mapped directly to the appropriate CB-IV reactions. The J values for the two NO_3 reactions in SAPRC'97 are summed to estimate the J value for the single NO_3 reaction in the CB-IV mechanism. Similarly the J values for the two methyl-glyoxal (MGLY) reactions in SAPRC'97 are summed to estimate the J value for the single MGLY photolysis reaction in the CB-IV mechanism. The average of the J values for the photolysis reactions involving CCHO and RCHO in SAPRC'97 is used to provide the J value for ALD2 in the CB-IV mechanism. The J values for OPEN (high molecular weight aromatic ring fragments) in CB-IV are not directly available from TUVAQM; these J values are taken from those employed in the UAM-FCM model.

As a result of implementing TUVAQM in the three air quality models, the computational time required to carry out a simulation increased. For example, using UAM621 with TUVAQM in the SoCAB increased the simulation time by approximately 50 percent.

7.2 Model results

To assess the influence of using TUVAQM on calculated ozone concentrations, we created displays of the gridded hourly-averaged concentration fields for both the original base case simulation (using the original photolysis treatment) and the simulation using TUVAQM. We also prepared a set of difference plots by subtracting the results from the original base case run from those derived using TUVAQM.

Generally, higher calculated ozone concentrations result from employing TUVAQM in the UAM621 simulation for the SoCAB. During the early morning hours through 0900, ozone levels differ by no more than 20 ppb over most of the modeling domain. In a few grid locations in the eastern downwind portions of the domain, ozone levels may be as much as 60 to 80 ppb higher using TUVAQM. These relatively large differences result from the carry over of ozone produced during the previous day. During the late morning and afternoon hours when the J values are relatively high, calculated ozone levels over a large portion of the modeling domain continue to differ by no more than about 20 ppb. However, differences in calculated ozone levels ranging from 100 to 131 ppb occur in the northeastern portion of the San Fernando Valley, the San Gabriel Valley, and the Pomona-Chino-Ontario area. Increases in ozone levels ranging from

80 to 100 ppb are noted in the eastern portion of the Chino Hills and just west of Riverside. Figures 7.1 and 7.2 illustrate the gridded hourly-averaged ozone concentration fields at 1400 on August 28, 1987, produced by UAM621 and UAM621 with TUVAQM, respectively. Figure 7.3 shows the difference in calculated ozone concentrations at 1400 on August 28. The largest difference in calculated ozone results between the two UAM621 simulations occurs at 1400. As indicated in Figure 7.1, the highest calculated ozone concentration in the original UAM621 simulation is 268 ppb, with concentrations exceeding 240 ppb occurring in only two grid cells. As shown in Figure 7.2 illustrating the UAM621 with TUVAQM results, the highest ozone concentration is 314 ppb with concentrations exceeding 240 ppb occurring in many grid cells. Figure 7.3 is a difference plot (expressed as the UAM621 with TUVAQM results minus the original UAM621 results) at 1400. Figure 7.3 shows that the largest differences in simulation results occur in an area along the south-facing base of the San Gabriel Mountains and the area from just west of Riverside to Ontario. The greatest difference in calculated ozone levels is 131 ppb located just north of Glendora. The domain peak ozone level occurred at 1500 in both simulations and in the same grid location (west of Riverside). The domain peak values for the UAM621 and UAM621 with TUVAQM simulations were 269 and 340 ppb, respectively. A summary of the results for other species is provided in Table 7.1.

The UAM-FCM results are similar in many respects to the UAM621 results. Figures 7.4 and 7.5 show the gridded hourly-averaged ozone concentrations at 1400 on August 28. The highest calculated ozone level in the original UAM-FCM baseline simulation is 292 ppb at this time; the highest value from the UAM-FCM with TUVAQM is 315 ppb. There are only five grid cells with calculated ozone exceeding 240 ppb at this time in the original UAM-FCM simulation, whereas ozone levels exceed 240 ppb in many more cells in the UAM-FCM with TUVAQM simulation. Figure 7.6 illustrates the difference in the gridded ozone fields (expressed as UAM-FCM with TUVAQM minus UAM-FCM) at 1400 from the two simulations. Again, the differences in calculated ozone values differ by no more than 20 ppb over most of the modeling domain and the TUVAQM treatment of photolysis rates yields higher calculated ozone concentrations along the base of the San Gabriel Mountains and in the area just west of Riverside to Ontario. Note that the domain peak ozone levels differ by only 1 ppb (314 versus 315 ppb) for the UAM621 and UAM-FCM simulations using TUVAQM. Implementing TUVAQM in UAM621 has a larger impact on calculated ozone levels than in UAM-FCM. The treatment of photolysis rates in the original version of UAM-FCM represents an upgrade to the treatment in UAM621 yielding *J* values that are more consistent with those generated using TUVAQM. The UAM621 and UAM-FCM simulations that both employ TUVAQM yield ozone results at 1400 on August 28 that differ by no more than 34 ppb. In examining the two model runs using

TUVAQM, UAM-FCM with TUVAQM yields higher ozone concentrations in most of the modeling domain and lower concentrations in the area encompassing the central basin, the eastern portion of the San Fernando Valley, the San Gabriel Valley, and areas to the south of Ontario. A summary of the results for other species is provided in Table 7.1.

Figures 7.7 and 7.8 illustrate the gridded hourly-averaged ozone concentrations at 1500 on August 5, 1990 for the original version of SAQM and the version that uses TUVAQM, respectively. The highest calculated ozone concentration in the domain from the original simulation on this day is 155 ppb, while the corresponding result from the version using TUVAQM is 163 ppb. During the early morning hours until 0800, the two versions of SAQM yield ozone results that differ by no more than 5 ppb. Throughout the remainder of the day, calculated ozone levels from the two models in most areas outside the San Francisco Bay area continue to differ by no more than 5 ppb. However, in the late morning and afternoon hours in the immediate downwind locations of the San Francisco Bay area, the version of SAQM using TUVAQM yields ozone concentrations that are as much as 34 ppb higher than those from the original version of SAQM. In the early afternoon, the TUVAQM version also yields ozone values that are as much as 41 ppb higher in a very limited area of Monterey Bay. In a small area of the San Joaquin Valley, calculated ozone concentrations from the TUVAQM version are just over 10 ppb higher than the original SAQM simulation results.

In general, the SAQM results for central California are similar to those of the UAM621 and UAM-FCM simulations for the SoCAB. That is, the TUVAQM versions of these models tend yield higher calculated ozone levels, especially in locations immediately downwind of the major metropolitan source areas. The influence of using TUVAQM in SAQM yielded smaller differences in calculated ozone levels. This may result from the fact that for the episodes studied, ambient ozone levels in the central California are lower than those in the SoCAB. In addition, implementing TUVAQM in SAQM has a less profound influence on calculated J values than its incorporation in the other two models.

	UAM621 (ppb)	UAM-FCM (ppb)	Comments
O3	-17 to 130	-7 to 81	Largest increases occur from 1000-1600 along the base of the San Gabriel Mountains and in the Riverside/Ontario areas
CO	-16 to 7	-11 to 1	Areas and times of largest decreases coincide with those for the largest O3 increases (see above)
NO	-46 to 4	-40 to 5	Largest decreases occur during early morning hours in areas where high O3 occurs
NO2	-48 to 24	-23 to 36	In UAM621, TUVAQM generally yields lower concentrations, with isolated areas where increased levels occur; in UAM-FCM, TUVAQM yields higher concentrations during the early morning hours as well as at midday in coastal areas with lower concentrations inland
NOX	-54 to 3	-26 to 20	In UAM621, TUVAQM yields lower levels, especially during midday in areas where high O3 occurs; in UAM-FCM, TUVAQM yields significant concentration differences in isolated areas
HNO3	-17 to 36	-25 to 9	In UAM621, TUVAQM yielded the greatest increases and decreases at night in areas surrounding Ontario; in UAM-FCM, TUVAQM yielded lower values at night throughout the most populated areas of the SoCAB
HONO	-0.1 to 0.8	-0.6 to 0.7	In UAM621, the greatest increases occurred in the central Basin from 0600-0800; in UAM-FCM, TUVAQM gave lower values at night in the central Basin, with increases in isolated coastal areas from 0600-0800.
PAN	-1 to 11	-1 to 6	Largest increases occur during midday in areas where significant O3 increases are noted (see O3 above)
H2O2	0 to 10	0 to 5	Largest increases occur during late morning and afternoon in areas in the vicinity and south of Ontario and in the San Gabriel Mountains
ISOP	-0.3 to 0.1	-0.2 to 0.1	Largest decreases occur during midday in San Gabriel Mountains; isolated significant increases
FORM	-0.4 to 6	-0.2 to 5	Largest increases occur in central Basin and San Fernando and San Gabriel Valleys during the day
ALD2	-3 to 1	-2 to 1	Largest decreases occur during midday in areas where largest O3 increases occur (see O3 above)

Table 7.1: Influence of using TUVAQM for selected species in the SoCAB. Results for August 28, 1987, expressed as the range of the differences in concentrations (UAM621 with TUVAQM minus UAM621 and similarly for UAM-FCM).

Layer 1 O3 -- UAM621

August 26-28, 1987-Baseline Simulation (UAM6.21)

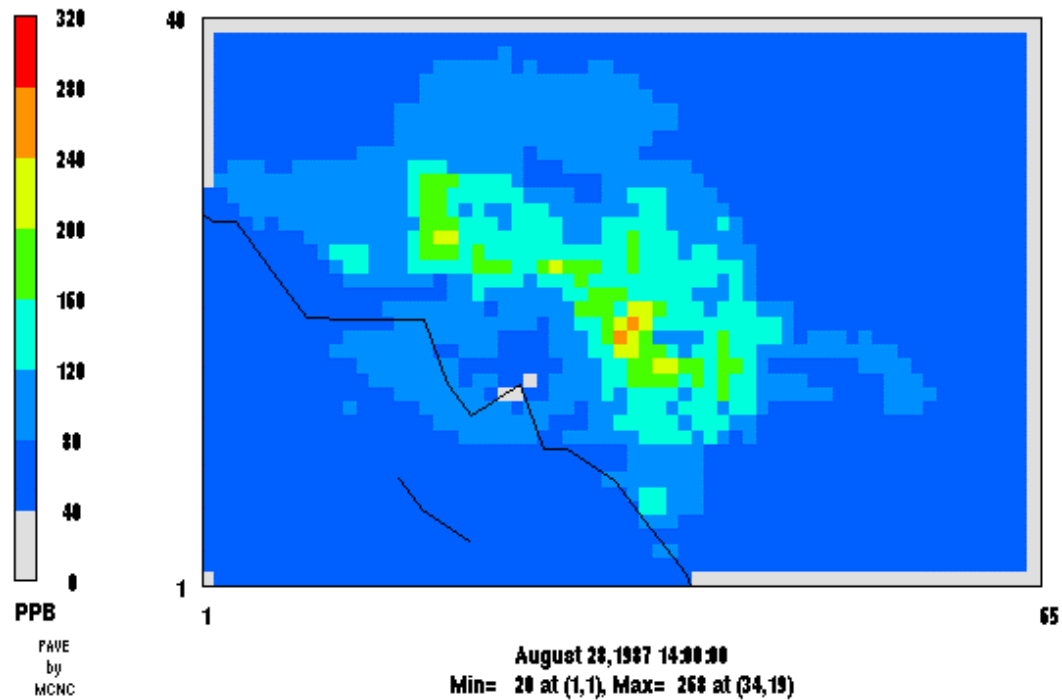


Figure 7.1. Calculated hourly-averaged ground level ozone concentrations (ppb) at 1400 on August 28, 1987 using the original version of UAM621.

Layer 1 O3 -- UAM621TUV

August 26-28, 1987--Baseline Simulation (UAM6.21TUV)

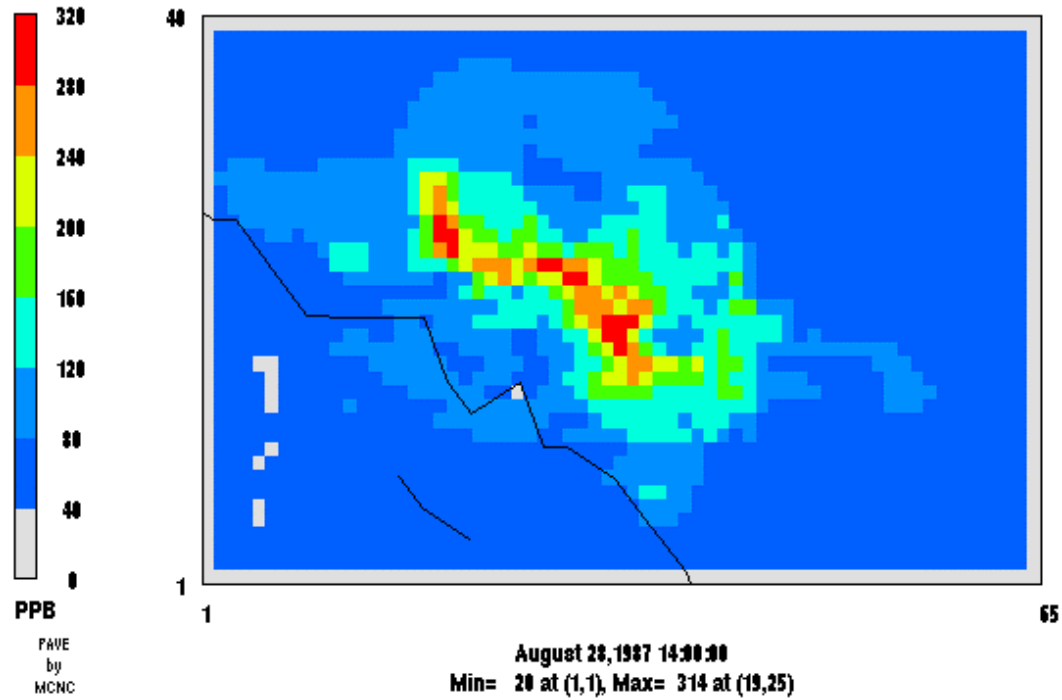


Figure 7.2. Calculated hourly-averaged ground level ozone concentrations (ppb) at 1400 on August 28, 1987 using UAM621 with TUVAQM.

Layer 1 O3 -- (UAM621TUV - UAM621)

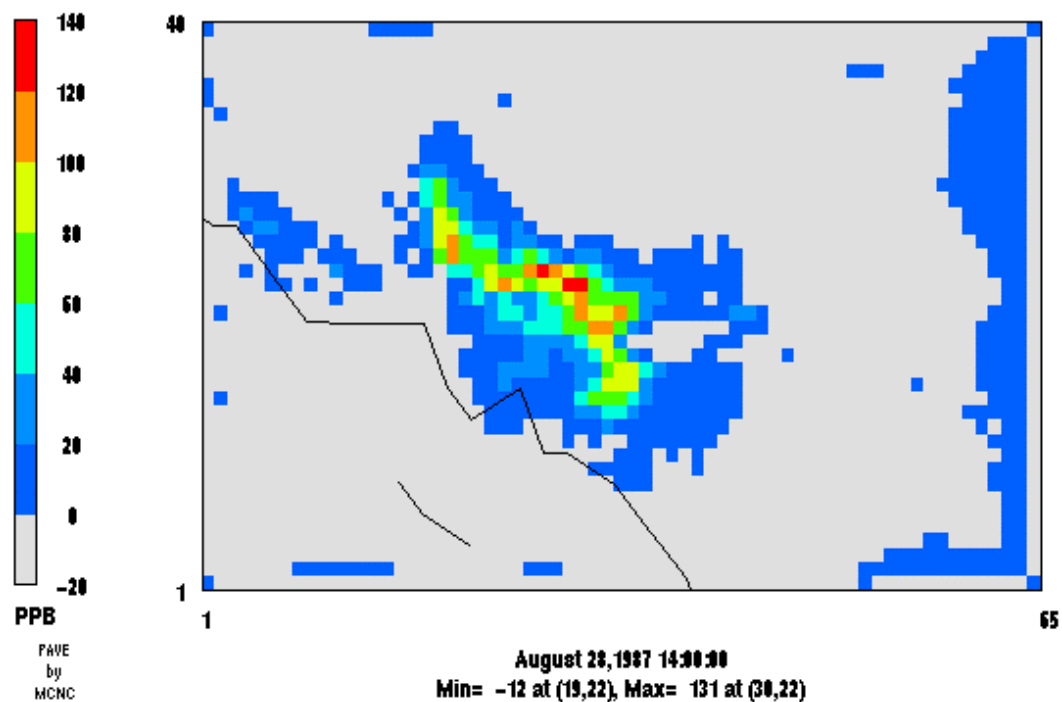


Figure 7.3. Difference in calculated hourly-averaged ground level ozone concentrations (ppb) at 1400 on August 28, 1987 – UAM621 with TUVAQM minus UAM621.

Layer 1 O3 -- UAMFCM

August 27, 1987- Basecase

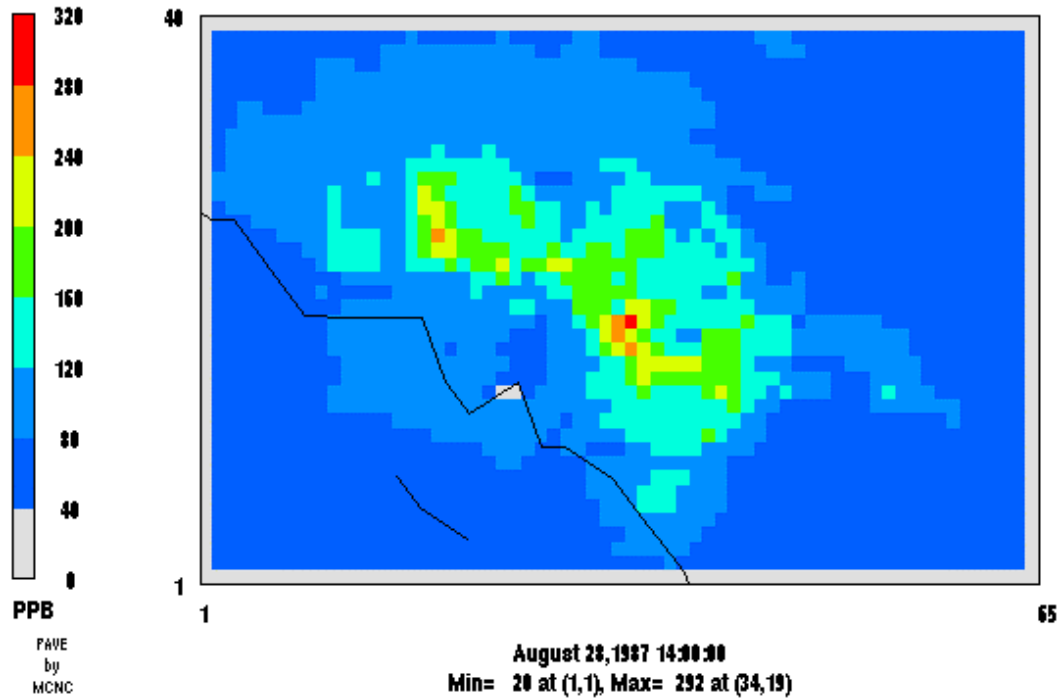


Figure 7.4. Calculated hourly-averaged ground level ozone concentrations (ppb) at 1400 on August 28, 1987 using the original version of UAM-FCM.

Layer 1 O3 -- UAMFCMTUV

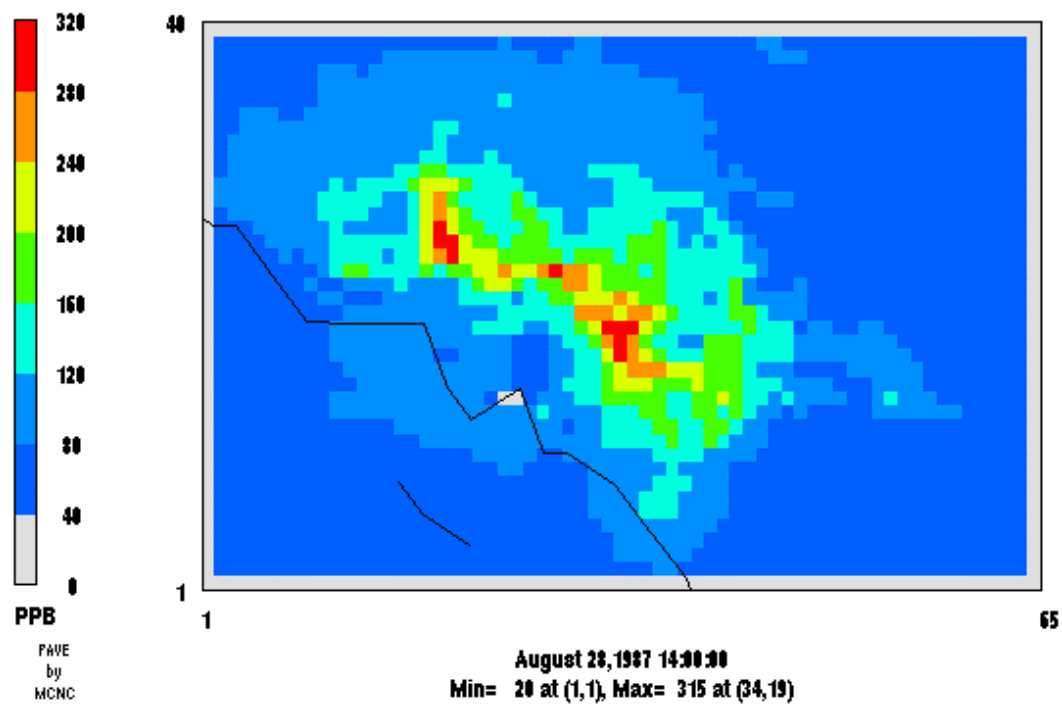


Figure 7.5. Calculated hourly-averaged ground level ozone concentrations (ppb) at 1400 on August 28, 1987 using UAM-FCM with TUVAQM.

Layer 1 O3 -- (UAMFCMTUV - UAMFCM)

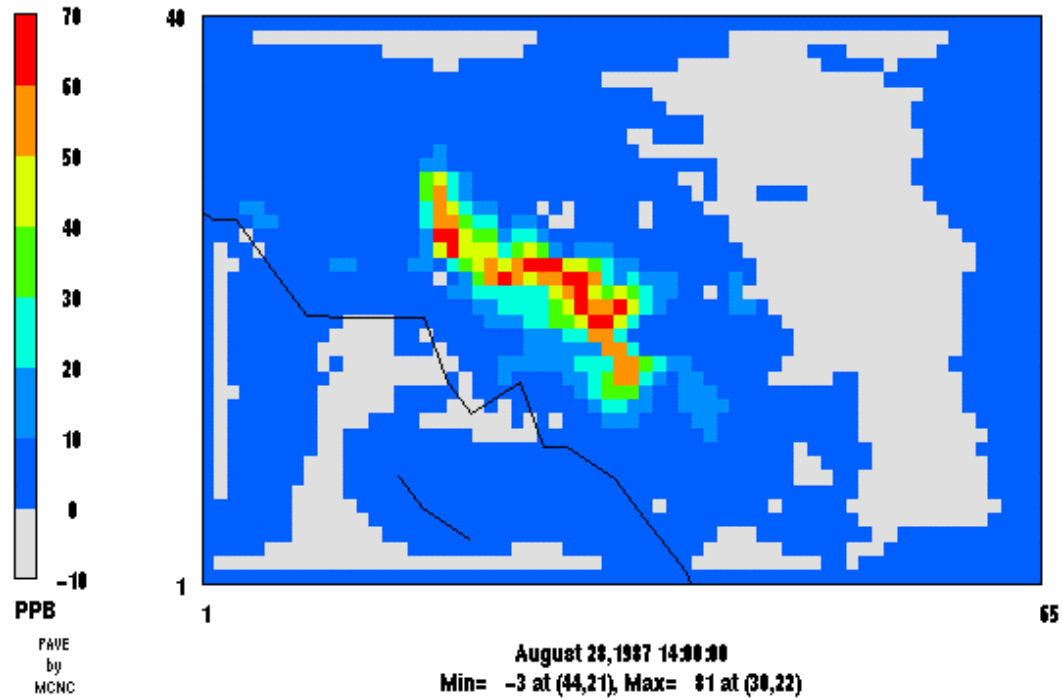


Figure 7.6. Difference in calculated hourly-averaged ground level ozone concentrations (ppb) at 1400 on August 28, 1987 – UAM-FCM with TUVAQM minus UAM-FCM.

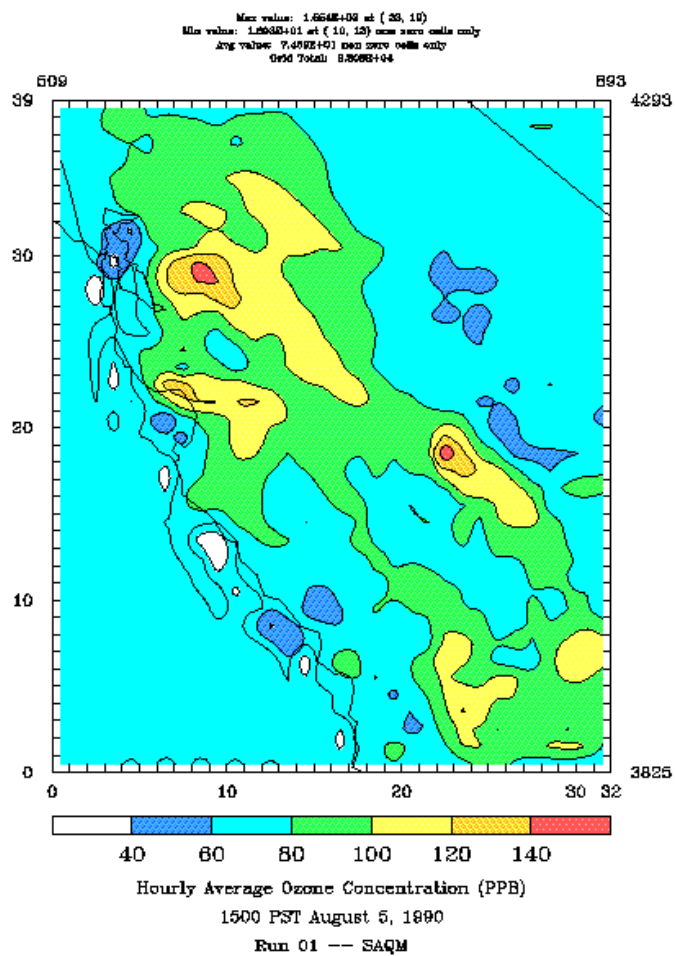


Figure 7.7. Calculated hourly-averaged ground level ozone concentrations (ppb) at 1500 on August 5, 1990 using the original version of SAQM.

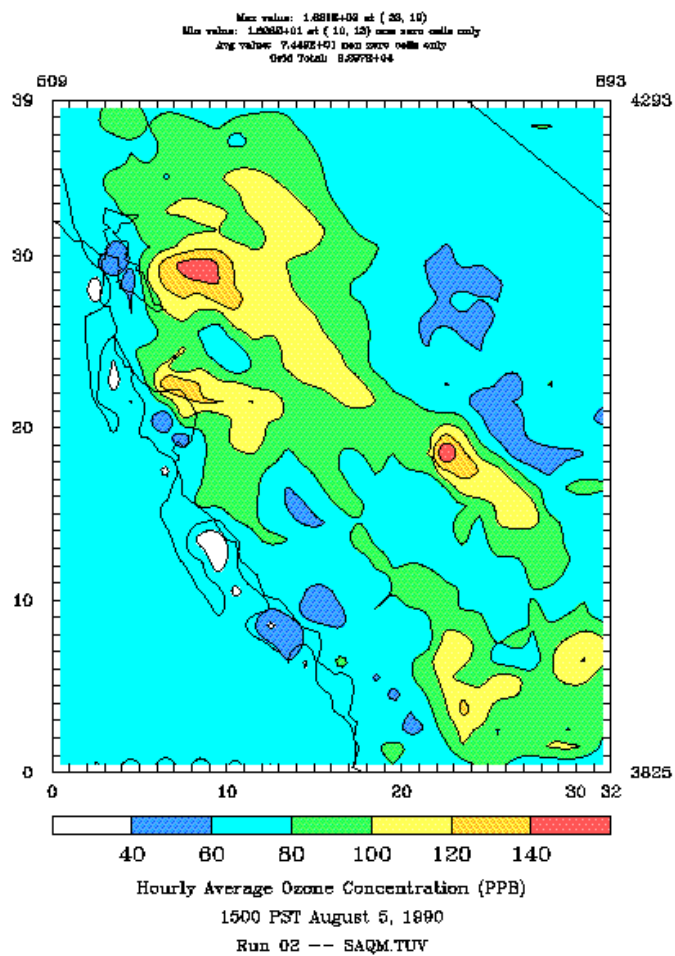


Figure 7.8. Calculated hourly-averaged ground level ozone concentrations (ppb) at 1500 on August 5, 1990 using SAQM with TUV AQM.

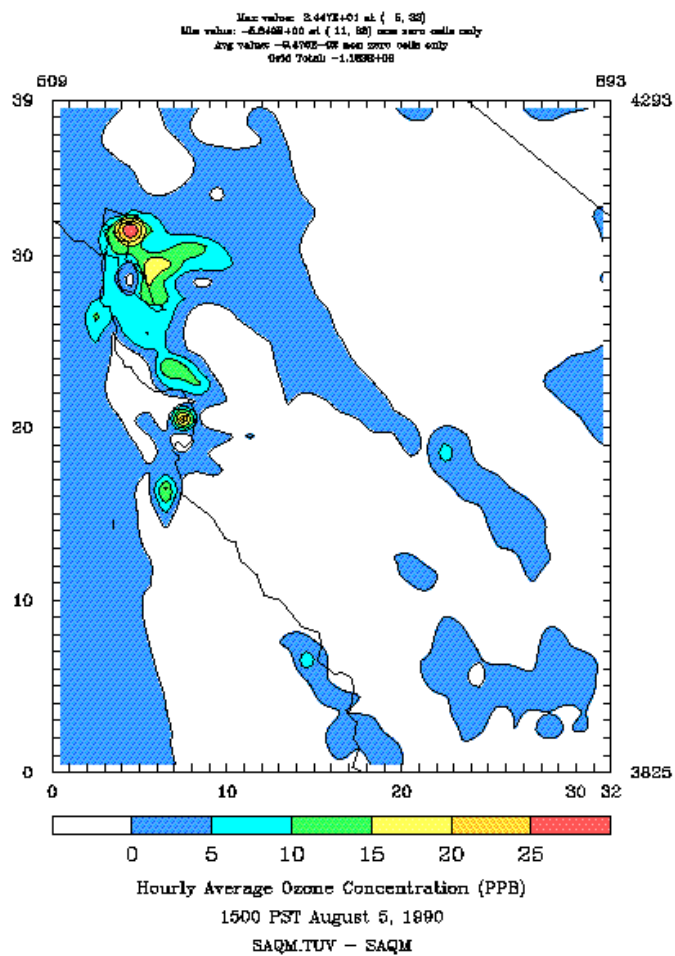


Figure 7.9. Difference in calculated hourly-averaged ground level ozone concentrations (ppb) at 1500 on August 5, 1990 – SAQM with TUV AQM minus SAQM.

8 Conclusions

Photolysis rates strongly influence the formation of photochemical air pollutants such as ozone. Photolysis rates of NO_2 and, depending on the VOC to NO_x ratio, formaldehyde are found to be among the most influential chemical reactions. The rates of photolysis depend on the integral of the product of absorption cross section, quantum yield and actinic flux over wavelength. While laboratory measurements have improved our understanding of cross sections and quantum yields for various photolyzing species, the representation of actinic flux in many air quality models is simplistic.

8.1 Radiative Transfer Models

Radiative transfer models exist that are fundamentally based in theory. Models that compute the spherically integrated light intensity (actinic flux) are appropriate for use in calculating photodissociation rate coefficients. Models differ mainly in the degree of approximation of their description of the angular dependence of the light intensity. In this research, the Tropospheric Ultraviolet-Visible radiation transfer model (TUV) was implemented to run online within urban and regional-scale photochemical models.

Data on atmospheric optical properties are sparse at the wavelengths influencing photolysis of atmospheric pollutants (i.e., the near UV from 290 to 420 nm). Important factors affecting the actinic flux include solar zenith angle, clouds, aerosol amount and optical properties, total ozone column, terrain elevation and ground albedo. Although higher-order approximations are available, we used a two-stream model in the present implementation of TUV. This was done to minimize computational burden and because larger uncertainties are related to the lack of appropriate data for the TUV model inputs described above.

8.2 TUV Sensitivity to Input Data

The sensitivity of photodissociation rate coefficients to selected TUV input parameters was examined, and the likely range of variation for these parameters was assessed. Two aerosol properties were found to be similarly influential. The aerosol optical depth (aerosol amount) has a potential wide range of variation, and a normalized sensitivity between -5% and -10% depending on the reaction. The aerosol single scattering albedo is uncertain, especially at the ultraviolet wavelengths; likely values range from 0.75 to 0.95. The normalized sensitivity to this parameter is about +50%. We expect variation in photolysis rate coefficients due to these parameters to be on the order of 10%. During summer, ground albedo in the Los Angeles area ranges from about 0.05 to 0.20. Normalized sensitivity is on the order of 15%. The challenge

here is to obtain high quality spatially-resolved values for ground albedo. The influence of total ozone column varies greatly depending on the reaction of interest. Not surprisingly, ozone photolysis rates are the most strongly affected. Formaldehyde photolysis rates are also influenced significantly by ozone column, whereas NO₂ and nitrous acid are barely affected. Variation of 10% (i.e., 30 Dobson Units) in ozone column lead to changes of 15% in ozone photolysis (for the O(¹D) channel), and 4% in formaldehyde photolysis (for the channel that forms radicals).

8.3 Variability in Optical Depth

Aerosols have the potential to affect photolysis reaction rates significantly (see above), and their optical properties have significant uncertainties. Therefore, we studied variability in total optical depths (including contributions due to Rayleigh scattering and absorption by ozone) in southern California to assess the importance of the aerosol contribution.

Measurements of direct (i.e., total minus diffuse) solar irradiance were made during the 1997 Southern California Ozone Study continuously at seven wavelengths at 300, 306, 312, 318, 326, 333 and 368 nm. At 300 nm, optical depths (mean \pm 1 S.D.) measured over the entire study period were 4.3 ± 0.3 at Riverside and 3.7 ± 0.2 at Mt Wilson. Optical depth decreased with increasing wavelength, falling at 368 nm to values of 0.8 ± 0.2 at Riverside and 0.5 ± 0.1 at Mt Wilson. At all wavelengths, both the mean and the relative standard deviation of optical depths were larger at Riverside than at Mt Wilson. At 300 nm, the difference between the smallest and largest observed optical depths corresponds to over a factor 2 increase in the direct beam irradiance for overhead sun, and over a factor 7 increase for a solar zenith angle of 60°.

Principal Component Analysis was used to reveal underlying factors contributing to variability in optical depths. PCA showed that a single factor (component) was responsible for the major part of the variability. At Riverside, the first component was responsible for 97% of the variability and the second component for 2%. At Mt Wilson, 89% of the variability could be attributed to the first component and 10% to the second. Dependence of the component contributions on wavelength allowed identification of probable physical causes: the first component is linked to light scattering and absorption by atmospheric aerosols, and the second component is linked to light absorption by ozone. These factors are expected to contribute to temporal and spatial variability in solar actinic flux and photodissociation rates of species including ozone, nitrogen dioxide, and formaldehyde.

8.4 Implementation and Application of TUV

The TUV model as been implemented as a flexible module that can be used within photochemical air quality models. A new interface was developed to allow flexible specification

of TUV input parameters by the model user. (The version of the module modified for implementation in air quality models is designed as TUVAQM.) This will allow air quality models to take advantage of more and better input data as they become available. The implementation of TUVAQM is highly modular, so that state-of-the-art treatment of radiative transfer can be maintained (e.g., switch to 4- or 8-stream models).

The photolysis module was implemented in three photochemical models: the Urban Airshed Model (UAM621), the Urban Airshed Model with Flexible Chemical Mechanism (UAM-FCM), and the SARMAP Air Quality Model (SAQM). The UAM621 and UAM-FCM models were used to simulate the August 26-28, 1987, SCAQS ozone episode in the South Coast Air Basin (SoCAB). Generally, higher calculated ozone concentrations resulted from employing TUVAQM, especially in the late morning and afternoon hours when relatively high ozone levels occur. For example, in the early afternoon of the simulation of 28 August, calculated hourly-averaged ozone concentrations were as much as 131 and 81 ppb higher using TUVAQM in UAM621 and UAM-FCM, respectively. Significant increases in calculated ozone concentrations occurred in the downwind areas of the San Gabriel Valley and the Riverside-San Bernardino areas. Much smaller increases in calculated ozone concentrations were noted in offshore, coastal, and central basin areas as well as in the easternmost and northernmost portions of the modeling domain. Differences in predicted ozone using TUVAQM may result not only from improved treatment of radiative transfer, but also because of more up to date information on absorption cross-section and quantum yields of photolyzing species such as formaldehyde.

SAQM was applied to the simulation of a large portion of central California for the August 3-6, 1990, ozone episode. Since the existing photolysis treatment in SAQM and TUVAQM share a somewhat similar origin, calculated ozone levels resulting from the implementation of TUVAQM were not as different as those noted for the implementation in UAM621 and UAM-FCM.

9 Recommendations

Further research is needed to reduce influential uncertainties associated with photolysis rates in photochemical models.

9.1 Radiometric data

At present the radiation monitoring network in California is heavily oriented toward broadband visible measurements in support of water supply needs and meteorological assessments. These data are marginally useful for assessing photolysis rates. Long-term measurements and study of wavelength-resolved UV irradiance and actinic flux are needed. Improved spatial coverage, and siting of radiometers in urban areas with high ozone should be considered. Modern instrumentation that separates direct and diffuse contributions to total light intensity is better suited to the tasks at hand. New instruments that measure wavelength-resolved actinic flux continuously are likely to be superior to chemical actinometer in both temporal resolution and applicability to more than one photolyzing species.

9.2 Clouds

Rigorous treatment of the effects of clouds on radiative transfer remains a challenging and active area of research. Situations with partially covered sky (broken clouds) are especially complex. The state should consider routinely acquiring satellite observations of cloud cover (e.g., Geostationary GOES Satellite Products by the National Environmental Satellite, Data, and Information Service at the National Oceanic and Atmospheric Administration) to support improved representation of cloud effects in future studies.

9.3 Air Quality Modeling

Further analyses are needed to assess more fully the performance characteristics of the modified versions of UAM621, UAM-FCM, and SAQM. Considering the differences in calculated ozone levels that were noted in portions of the SoCAB, model sensitivity studies are needed to understand better whether use of TUVAQM has a significant influence on the effectiveness of VOC and NO_x emission controls in the SoCAB and the amount of control that may be needed for attainment of the one- and eight-hour ozone standards.

Literature cited

- Baldasano J. M., Delgado R. and Calbo J., 1998. Applying receptor models to analyze urban/suburban VOCs air quality in Martorell (Spain). *Environ. Sci. Technol.* 32, 405-412.
- Bergin M. S., Russell A. G. and Milford J. B., 1998. Effects of chemical mechanism uncertainties on the reactivity quantification of volatile organic compounds using a three-dimensional air quality model. *Environ. Sci. Technol.* 32, 694-703.
- Bigelow D. S. and Slusser J. R., 2000. Establishing the stability of multi-filter UV rotating shadowband radiometers. *J. Geophys. Res.* 105, 4833-4840.
- Bigelow, D. S., Slusser J. R., Beaubien A. F. and Gibson J. H., 1998. The USDA Ultraviolet Radiation Monitoring Program. *Bull. Amer. Meteorol. Soc.* 79, 601-615.
- Blindauer C., Rozanov V. and Burrows J. P., 1996. Actinic flux and photolysis frequency comparison computations using the model PHOTOGT. *J. Atmos. Chem.* 24, 1-21.
- Carter W. P. L. Updated SAPRC-97 Mechanism. Electronic source at <ftp://cert.ucr.edu/pub/carter/mech/saprc97/>, 1997.
- Chandrasekhar, S. Radiative transfer. Dover, New York, 1960 (2nd ed.) 393pp.
- Coakley J. A. Jr. and Chýlek P., 1975. The two-stream approximation in radiative transfer: Including the angle of the incident radiation. *J. Atmos. Sci.* 32, 409-418.
- Demerjian K.L., Schere K.L. and Peterson J.T., 1980. Theoretical estimates of actinic (spherically integrated) flux and photolytic rate constants of atmospheric species in the lower troposphere. In *Advances in Environmental Science and Technology*, 10, 369-441.
- Dickerson R. R., Kondragunta S., Stenchikov G., Civerto K. L., Doddridge B. G. and Holben B. N., 1997. The impact of aerosols on solar ultraviolet radiation and photochemical smog. *Science* 278, 827-830.
- Everitt B. S. and Dunn G. *Applied Multivariable Data Analysis*. Oxford University Press, New York, NY, 1992.
- Falls A. H., McRae G. J. and Seinfeld J. H., 1979. Sensitivity and uncertainty of reaction mechanisms for photochemical air pollution. *Int. J. Chem. Kinet.* 11, 1137-1162.
- Finlayson-Pitts B. J. and Pitts J. N. Jr. *Atmospheric Chemistry: Fundamentals and Experimental Techniques*. Wiley-Interscience, New York, NY, 1986.

- Gao D., Stockwell W. R. and Milford J. B., 1995. First-order sensitivity and uncertainty analysis for a regional-scale gas-phase chemical mechanism. *J. Geophys. Res.* 100, 23153-23166.
- Gao D., Stockwell W. R. and Milford J. B., 1996. Global uncertainty analysis of a regional-scale gas-phase chemical mechanism. *J. Geophys. Res.* 101, 9107-9119.
- Gery M. W., Whitten G. Z., Killus J. P. and Dodge M. C., 1992. A Photochemical Kinetics Mechanism for Urban and Regional Scale Computer Modeling. *J. Geophys. Res.* 94, 12,925–12,956.
- Harley R. A., Russell A. G., McRae G. J., Cass G. R. and Seinfeld J. H., 1993. Photochemical modeling of the Southern California Air Quality Study. *Environ. Sci. Technol.*, 27, 378-388.
- Harrison L. and Michalsky J., 1994. Objective algorithms for the retrieval of optical depths from ground-based measurements. *Appl. Opt.* 33, 5126-5132.
- Henry R. C. and Hidy G. M., 1979. Multivariate analysis of particulate sulfate and other air quality variables by principal components — Part I. Annual data from Los Angeles and New York. *Atmos. Environ.* 13, 1581-1596.
- Henry R. C. and Hidy G. M., 1982. Multivariate analysis of particulate sulfate and other air quality variables by principal components — Part II. Salt Lake City, Utah and St. Louis, Missouri. *Atmos. Environ.* 16, 929-943.
- Jolliffe I. T., 1972. Discarding variables in a principal component analysis 1: Artificial data. *Applied Statistics* 21 160-173.
- Joseph J. H., Wiscombe W. J. and Weinman J. A., 1976. The delta-Eddington approximation for radiative transfer. *J. Atmos. Sci.* 33, 2452-2459.
- Larson, S., Cass G., Hussey, K., and Luce F., 1984. Visibility model verification by image processing techniques. Final Report to State of California Air Resources Board under Agreement A2-077-32, Sacramento, CA.
- Lean, J. L., Rottman G. J., Kyle H. L., Woods T. N., Hickey J. R., and Puga L. C., 1997. Detection and parameterization of variations in solar middle and near-ultraviolet radiation (200-400 nm). *J. Geophys. Res.* 102, 29,939-29,956.
- Lenoble J. (ed.) Radiative Transfer in Scattering and Absorbing Atmospheres: Standard Computational Procedures. A. Deepak Publishing, Hampton, VA, 1985. 300 pp.
- Liou K.-N., 1973. A numerical experiment on Chandrasekhar's discrete-ordinate method for radiative transfer: Applications to cloudy and hazy atmospheres. *J. Atmos. Sci.* 30, 1303-1326.

- Liou K.-N., 1974. Analytic two-stream and four-stream solutions for radiative transfer. *J. Atmos. Sci.* 31, 1473-1475.
- Lurmann F. W., Carter W. P. L. and Coyner L. A. A Surrogate Species Chemical Reaction Mechanism for Urban-Scale Air Quality Simulation Models. ERT Inc., Newbury Park, CA and Statewide Air Pollution Research Center, University of California, Riverside, CA, 1987. Report to the US Environmental Protection Agency under contract 68-02-4104.
- Madronich S., 1987. Photodissociation in the atmosphere 1. Actinic flux and the effects of ground reflections and clouds. *J. Geophys. Res.* 92, 9740-9752.
- Madronich S., 2000. Atmospheric Chemistry Division, National Center for Atmospheric Research, Boulder, Colorado. Personal communication, April 2000.
- Meador W. E. and Weaver W. R., 1980. Two-stream approximations to radiative transfer in planetary atmospheres: A unified description of existing methods and a new improvement. *J. Atmos. Sci.* 37, 630-643.
- Meng Z., Dabdub D. and Seinfeld J. H., 1997. Chemical coupling between atmospheric ozone and particulate matter. *Science* 277, 116-119.
- Milford J. B., Gao D., Russell A. G. and McRae G. J., 1992. Use of sensitivity analysis to compare chemical mechanisms for air-quality modeling. *Environ. Sci. Technol.* 26, 1179-1189.
- Nakajima T. and Tanaka M., 1986. Matrix formulations for the transfer of solar radiation in a plane parallel scattering atmosphere. *J. Quant. Spectrosc. Radiat. Transfer.* 35, 13-21.
- NASA (2000). Total ozone mapping spectrometer (TOMS) ozone column retrievals. Goddard Space Flight Center, National Aeronautics and Space Administration. Downloaded from <http://toms.gsfc.nasa.gov/ozone/ozone01.html>.
- Odum J. R., Jungkamp T. P. W., Griffin R. J., Flagan R. C. and Seinfeld J. H., 1997. The atmospheric aerosol-forming potential of whole gasoline vapor. *Science* 276, 96-99.
- Plass G. N., Kattawar G. W., Catchings F. E., 1973. Matrix operator theory of radiative transfer. 1: Rayleigh Scattering. *Appl. Opt.* 12, 314-329.
- Peterson J. T. Calculated actinic fluxes (290-700 nm) for air pollution photochemistry applications. US Environmental Protection Agency, Research Triangle Park, NC, 1976. EPA-600/4-76-025.
- Ruggaber A., Dlugi R. and Nakajima T., 1994. Modelling radiation quantities and photolysis frequencies in the troposphere. *J. Atmos. Chem.* 18, 171-210.

- Schmid B., Spyak P. R., Biggar S. F., Wehrli C., Sekler J., Ingold T., Mätzler C. and Kämpfer N., 1998. Evaluation of the applicability of solar and lamp radiometric calibrations of a precision Sun photometer operating between 300 and 1025 nm. *Appl. Opt.* 37, 3923-3941.
- Schmid B., Michalsky J., Halthorne R., Beauharnois M., Harrison L., Livingston J. and Russell P., 1999. Comparison of aerosol optical depth from four solar radiometers during the fall 1997 ARM intensive observation period. *J. Geophys. Res.* 17, 2725-2728.
- Schotland R. M. and Lea T. K., 1986. Bias in a solar constant determination by the Langley method due to structured atmospheric aerosol. *Appl. Opt.* 25, 2486-2491.
- Seinfeld J. H. and Pandis S. N. *Atmospheric Chemistry and Physics*. Wiley-Interscience, New York, NY, 1997.
- Shaw, G. E., Reagan, B. M. and Herman B. M., 1973. Investigations of atmospheric extinction using direct solar radiation measurements made with a multiple wavelength radiometer. *J. Appl. Meteor.* 12, 374-380.
- Shettle E. P. and Weinman J. A., 1970. The transfer of solar irradiance through inhomogeneous turbid atmospheres evaluated by Eddington's approximation. *J. Atmos. Sci.* 27, 1048-1055.
- Slusser J. R., Gibson J. H., Bigelow D. S., Kolinski D., Disterhoft D. P., Lantz K. and Beaubien A., 2000. Langley method of calibrating UV filter radiometers. *J. Geophys. Res.* 105, 4841-4849.
- Stamnes K. and Swanson R. A., 1981. A new look at the discrete-ordinate method for radiative transfer calculations in anisotropically scattering atmosphere. *J. Atmos. Sci.* 38, 387.
- Stamnes K., Tsay S.-C., Wiscombe W. and K. Jayaweera., 1988. Numerically stable algorithm for discrete-ordinate-method radiative transfer in multiple scattering and emitting layered media. *Appl. Opt.* 27, 2502-2509.
- Steele H. M. and Turco R. P., 1997. Separation of aerosol and gas components in the Halogen Occultation Experiment and the Stratospheric Aerosol and Gas Experiment (SAGE) II extinction measurements: Implications for SAGE II ozone concentrations and trends. *J. Geophys. Res.* 102, 19,665-19,681.
- Stephens G. L. *Remote Sensing of the Lower Atmosphere*. Oxford University Press, New York, NY, 1994.

- Taha H., 1998. Environmental Energy Technologies Division, Lawrence Berkeley National Laboratory, Berkeley, California. Personal communication, 1998.
- Thomason L. W., Herman B. M. and Reagan J. A., 1983. The effect of Atmospheric Attenuators with Structured Vertical Distributions on Air Mass Determinations and Langley Plot Analysis. *J. Atmos. Sci.* 40, 1851-1854.
- Tomasi C., Vitale V. and De Santis L. V., 1998. Relative optical mass functions for air, water vapour, ozone, and nitrogen dioxide in atmospheric models presenting different latitudinal and seasonal conditions. *Meteorol Atmos. Phys.* 65, 11-30.
- Toon O. B., McKay C. P., Ackerman T. P. and Santhanam K., 1989. Rapid calculation of radiative heating rates and photodissociation rates in inhomogeneous multiple scattering atmospheres. *J. Geophys. Res.* 94, 16,287-16,301.
- Vuilleumier L., Harley R. A. and Brown N. J., 1997. First- and Second-Order Sensitivity Analysis of a Photochemically Reactive System (a Green's Function Approach). *Environ. Sci. Technol.* 31, 1206-1217.
- Yang Y. J., Stockwell W. R. and Milford J. B., 1995. Uncertainties in incremental reactivities of volatile organic compounds. *Environ. Sci. Technol.* 29, 1336-1345.
- Yang Y. J., Stockwell W. R. and Milford J. B., 1996. Effect of chemical product yield uncertainties on reactivities of VOCs and emissions from reformulated gasolines and methanol fuels. *Environ. Sci. Technol.* 30, 1392-1397.